

UMEÅ UNIVERSITY  
Faculty of Science and Technology  
Department of Physics

## **Modelling air flow in the larynx**

Master's thesis

Author:  
Ugis Lacis  
880907-7319  
[ugis.lacis@gmail.com](mailto:ugis.lacis@gmail.com)

Supervisors:  
Martin Berggren  
Eddie Wadbro

Umeå 2012



## Abstract

In some cases, a change of epiglottic fold geometry during exercising can be a reason for breathing problems. Such a condition is called exercise induced laryngeal obstruction. The condition is only beginning to be recognised and not many investigations have been done. The current work uses computational fluid dynamics to obtain qualitative and quantitative relations between various epiglottic fold geometries and the resulting flow rates through the larynx for a constant lung suction pressure. Incompressible, steady Navier–Stokes equations with standard  $k - \omega$  turbulence modelling are used to compute the air flow in the larynx. The numerical simulations show an expected flow rate drop for blocked larynx cases. Surprisingly, the results show an increase in flow rates for partially blocked larynx cases. Also, there is an increase in resulting flow for cases with larger distance between the epiglottic fold and vocal chords.

The current work uses a simple elastic description to acquire feasible shapes of the epiglottic fold for a given flow and given elasticity modulus. A fixed point iteration method is used to balance the fluid forces and the elasticity forces. The resulting shape has a notable similarity with a laryngoscopic view of the epiglottic fold.

## Acknowledgments

First of all I want to thank my supervisors Eddie Wadbro and Martin Berggren for interesting discussions and consultations through my work. Their guidance helped me to pursue goals of this work and their company helped me to stay motivated and focused. I thank Uppsala University researcher Leif Nordang and his colleagues for introducing us to the problem and providing valuable insights in the medicine. I also thank Staffan Grundberg from TFE for consulting me on elasticity issues.

I would also like to thank researchers Jarmo Malinen and Atle Kivelä at Helsinki University of Technology for kindly sharing larynx 3D geometries and for assistance with developed generation procedures.

I also thank my colleagues and the personnel at *UMIT* laboratory for keeping interesting and motivating company. Last but not least I want to thank my family and friends for the support during my study time abroad.

---

## List of abbreviations and symbols

EIA	Exercise Induced Asthma						
EILO	Exercise Induced Laryngeal Obstruction						
FD	Fluid Dynamics						
CFD	Computational Fluid Dynamics						
DNS	Direct Numerical Simulation						
RANS	Reynolds Averaged Navier–Stokes						
LES	Large Eddy Simulation						
MRI	Magnetic Resonance Imaging						
2D, 3D	Two (three) dimensional						
$\vec{u}$	Flow velocity in Eulerian coordinates [m/s]						
$P$	Fluid pressure in Eulerian coordinates [Pa]						
$k$	Averaged turbulent kinetic energy [ $m^2/s^2$ ]						
$\varepsilon$	Dissipation rate of turbulent kinetic energy [ $m^2/s^3$ ]						
$\omega$	Specific dissipation rate of turbulent kinetic energy [ $s^{-1}$ ]						
$Q$	Flow rate, in 2D case [ $m^2/s$ ] and 3D case [ $m^3/s$ ]						
$V_E$	Minute ventilation rate (including inflow and outflow) [l/min]						
$\Phi$	Scalar field in Eulerian coordinates[misc]						
$\vec{A}$	Vector field in Eulerian coordinates [misc]						
$\mathbf{B}$	Second-rank tensor field in Eulerian coordinates or matrix [misc]						
$A_i$	Vector field component $i$ [misc]						
$B_{ij}$	Tensor field or matrix component $ij$ [misc] <table style="margin-left: 20px;"> <tr> <td><math>i</math></td><td>Free index (component)</td></tr> <tr> <td><math>ii</math></td><td>Einstein's summation convention</td></tr> <tr> <td><math>j</math></td><td>Variable derivative in respect to coordinate <math>j</math></td></tr> </table>	$i$	Free index (component)	$ii$	Einstein's summation convention	$j$	Variable derivative in respect to coordinate $j$
$i$	Free index (component)						
$ii$	Einstein's summation convention						
$j$	Variable derivative in respect to coordinate $j$						
$\mu$	Dynamic viscosity of air [ $\mu = 1.8369 \cdot 10^{-5}$ Pa·s at $T = 20^\circ\text{C}$ ]						
$\rho$	Density of air [ $\rho = 1.204$ kg/m <sup>3</sup> at $T = 20^\circ\text{C}$ ]						
$\mu/\rho = \nu$	Kinematic viscosity of air [ $\nu = 1.5257 \cdot 10^{-5}$ m <sup>2</sup> /s at $T = 20^\circ\text{C}$ ]						

# Contents

<b>1</b>	<b>Introduction</b>	<b>1</b>
1.1	Short description of medical background . . . . .	1
1.1.1	Basics of the larynx structure . . . . .	1
1.1.2	Exercise induced laryngeal obstruction (EILO) . . . . .	2
1.2	Analysis of selected literature . . . . .	4
1.2.1	Characteristics of the larynx . . . . .	4
1.2.2	CFD simulations in the larynx . . . . .	4
1.3	Preliminary analysis . . . . .	6
1.3.1	Flow characteristics . . . . .	6
1.3.2	Deformation characteristics . . . . .	6
1.3.3	Time and velocity scales . . . . .	7
1.4	Goals of current work . . . . .	8
<b>2</b>	<b>CFD simulation</b>	<b>9</b>
2.1	Selection of suitable simulation software . . . . .	9
2.2	Description of COMSOL 4.2 simulation software . . . . .	10
2.2.1	Basics of the FEM application to the CFD . . . . .	10
2.2.2	Turbulence modelling in COMSOL 4.2 . . . . .	12
2.2.3	Mesning procedures in COMSOL 4.2 . . . . .	12
2.2.4	Solvers in COMSOL 4.2 . . . . .	14
2.3	Selection of suitable boundary conditions . . . . .	15
<b>3</b>	<b>Developed test models and conditions</b>	<b>19</b>
3.1	Development of model geometries . . . . .	19
3.1.1	Preliminary 2D geometry, Model 0 . . . . .	19
3.1.2	The improved 2D geometry, Model 1 . . . . .	20
3.2	Simulation methodology . . . . .	21
3.3	Description of the epiglottic fold elasticity . . . . .	22
3.3.1	Simple 1D continuous elastic description . . . . .	22
3.3.2	Methodology for the CFD simulation with an incorporated 1D elasticity . . . . .	24
<b>4</b>	<b>Results and analysis</b>	<b>27</b>
4.1	Turbulence time scale study . . . . .	28
4.2	Solution convergence study . . . . .	29
4.2.1	Domain size study . . . . .	29

4.2.2	Mesh type and size study . . . . .	31
4.3	Model 0 results . . . . .	34
4.3.1	Reference simulation . . . . .	34
4.3.2	Epiglottic fold distance study . . . . .	34
4.3.3	Epiglottic fold length study . . . . .	37
4.3.4	Epiglottic fold angle study . . . . .	39
4.4	Model 1 results . . . . .	42
4.4.1	Reference simulation . . . . .	42
4.4.2	Laryngeal ventricle existence study . . . . .	42
4.4.3	Pressure–flow characteristics study . . . . .	42
4.4.4	Epiglottic fold angle and length study . . . . .	46
4.4.5	Vocal cord opening study . . . . .	46
4.4.6	False vocal cord distance study . . . . .	50
4.5	Model 1 with elasticity results . . . . .	52
4.5.1	Simulation methodology . . . . .	52
4.5.2	Stiff epiglottic fold study . . . . .	53
4.5.3	Soft epiglottic fold study . . . . .	54
<b>5</b>	<b>Investigation for future 3D simulations</b>	<b>57</b>
5.1	Conceptual model . . . . .	57
5.2	Constructed geometries from MRI scans . . . . .	58
<b>6</b>	<b>Conclusions</b>	<b>61</b>
<b>A</b>	<b>Derivation of a beam stretching equation</b>	<b>63</b>
<b>B</b>	<b>Full analytical description of smooth flow guide</b>	<b>66</b>
<b>C</b>	<b>Tied transition section boundary shape and integration</b>	<b>73</b>
<b>References</b>		<b>75</b>

## List of Figures

1.1	Left: vertical cross-section of larynx (from Mancuso et al. [7]). Right: laryngoscopic view of larynx (from Gray [4]). The parts of interest enumerated.	1
1.2	A vertical cross-section representation of the larynx [14]. The added arrows schematically illustrate the glottic EILO (left) and the supra-glottic EILO (right).	3
1.3	The laryngoscopic view of the supra-glottic obstruction condition [12], the open state (left) and the closed state (right).	3
1.4	The example of schematics for some larynx measurements [2], height of the larynx (left) and the vocal cord dimensions (right).	4
1.5	A sagittal image (left) and the deduced 3D geometry with pressure probes (right), not to scale. Mylavarapu et al. [11] work.	5
2.1	Example of the $P1 + P1$ (left) and the $P2 + P1$ (right) FEM dicretizations for the Navier–Stokes equations.	11
2.2	The default CFD mesh, generated by the COMSOL 4.2 near the curved surface.	13
2.3	The pure triangular CFD mesh, generated by the COMSOL 4.2 near the curved surface.	13
2.4	COMSOL 4.2 solver sequence for stationary CFD solutions with the $k - \omega$ turbulence model.	14
2.5	A generic sketch of the computational domain.	15
2.6	An illustration of the wall function boundary condition for the turbulence modelling.	17
3.1	Model 0 geometry approximation over the larynx cross section image [14], a global geometry with the vocal chords (left) and an epiglottic fold design (right).	19
3.2	3D representation sketch of the larynx Model 0 geometry approximation with $L_z$ as the length in the $\hat{z}$ dimension.	20
3.3	The larynx Model 1 geometry approximation over the larynx cross section image [14], a global geometry with vocal chord (left) and the epiglottic fold design (right).	21
3.4	A block scheme representation of the Model 0 and the Model 1 simulation methodology.	22

3.5	Sketch of a simple beam bending, one end fixed, a force on the other end and a load on boundaries applied (left), a small bent beam element (middle) and the relation to the linear stretching (right). . . . .	23
3.6	A sketch of the epiglottic fold shape data representation (left) and the shape skeleton construction (right). . . . .	24
3.7	Epiglottic fold shapes generated with a rough resolution (left) and a fine resolution (right). . . . .	25
3.8	A selection of the epiglottic fold boundary (left) and the parametric pressure plot over the surface in respect to the $x$ coordinate (right). . . . .	25
3.9	A construction of the 1D load from the epiglottic fold boundary force densities (left) and the representation on 1D mesh (right). . . . .	25
3.10	The shape of the first epiglottic fold (left) and the mapped load from the pressure and the total stress (right). . . . .	26
3.11	The shape of second test epiglottic fold (left) and the mapped load from the pressure and the total stress (right). . . . .	26
4.1	A schematic representation of selected quantities to be measured, Model 0 (left) and Model 1 (right). . . . .	27
4.2	The velocity magnitude at times $t = 4$ ms (left), $t = 5$ ms (middle) and $t = 6$ ms (right). The unsteady simulation with laminar outflow boundary condition, compressible Navier-Stokes equations. . . . .	28
4.3	The pressure for the surface point just below the vocal cords, the selected time interval. . . . .	29
4.4	The pressure at the non-slip surface for various simulation domain lengths. .	30
4.5	The pressure at the non-slip surface for various simulation domain lengths with the zero pressure at the inlet. . . . .	30
4.6	The pressure at the non-slip surface for various mesh types and sizes, two different discretizations. . . . .	31
4.7	The boundary layer mesh around the vocal cords, different mesh sizes. . .	32
4.8	The velocity streamlines around the vocal cords for different mesh sizes and discretizations, when using the boundary layer mesh. . . . .	32
4.9	The triangular mesh around the vocal cords for different mesh sizes. . .	33
4.10	The velocity streamlines around the vocal cords for different mesh sizes and discretizations, when using the purely triangular mesh. . . . .	33
4.11	The velocity magnitudes for the epiglottic fold distances $f_{\text{dist}} = 3, 8, 13$ mm, Model 0. . . . .	35
4.12	The epiglottic fold distance case study, the flow results, Model 0. . . . .	35
4.13	The epiglottic fold distance case study, the torque on the epiglottic fold, Model 0. . . . .	36
4.14	The epiglottic fold distance case study, the horizontal force on the vocal cords, Model 0. . . . .	36

4.15 The velocity magnitudes for the epiglottic fold lengths $f_{\text{length}} = 3, 5, 7 \text{ mm}$ , Model 0 . . . . .	37
4.16 The epiglottic fold length case study, the flow results, Model 0 . . . . .	38
4.17 The epiglottic fold length case study, the torque on epiglottic fold, Model 0 . . . . .	38
4.18 The epiglottic fold length case study, the horizontal force on the vocal cords, Model 0 . . . . .	39
4.19 The velocity magnitudes for the epiglottic fold angles $f_{\text{angle}} = 20^\circ, 55^\circ, 90^\circ$ , Model 0 . . . . .	40
4.20 The epiglottic fold angle case study, the flow results, Model 0 . . . . .	40
4.21 The epiglottic fold angle case study, the torque on the epiglottic fold, Model 0 . . . . .	41
4.22 The epiglottic fold angle case study, the horizontal force on the vocal cords, Model 0 . . . . .	41
4.23 Model 1 with (left) and without (right) the laryngeal ventricle, the velocity magnitude. . . . .	43
4.24 The resulting flow as a function of the epiglottic fold angle with and without the laryngeal ventricle, Model 1. . . . .	43
4.25 An example of the velocity field for the flow $Q = 40 \text{ l/min}$ with the epiglottic fold in the opened (left) and the closed (right) state, Model 1. . . . .	44
4.26 The obtained pressure–flow curves with the epiglottic fold in the opened and the closed state, Model 1. . . . .	44
4.27 The obtained pressure–flow log-log curve with the epiglottic fold in the opened state, a linear fit in a selected interval, Model 1. . . . .	45
4.28 The obtained pressure–flow log-log curve with the epiglottic fold in the closed state, a linear fit in a selected interval, Model 1. . . . .	45
4.29 The velocity magnitudes for epiglottic fold angles $f_{\text{angle}} = -16^\circ, 37^\circ, 89^\circ$ and epiglottic fold length $f_{\text{length}} = 7.5 \text{ mm}$ , Model 1. . . . .	47
4.30 The velocity magnitudes for epiglottic fold angles $f_{\text{angle}} = -16^\circ, 37^\circ, 89^\circ$ and epiglottic fold length $f_{\text{length}} = 5.5$ , Model 1. . . . .	47
4.31 The velocity magnitudes for epiglottic fold angle values $f_{\text{angle}} = -16^\circ, 37^\circ, 89^\circ$ and epiglottic fold length $f_{\text{length}} = 3.5 \text{ mm}$ , Model 1. . . . .	48
4.32 The epiglottic fold angle and length case study. The resulting flow contour lines. The maximal flow marked by a blue star, Model 1. . . . .	48
4.33 The velocity magnitudes for the epiglottic fold angle values $f_{\text{angle}} = -16^\circ, 37^\circ, 89^\circ$ and vocal cord opening $v_{\text{open}} = 6.3 \text{ mm}$ , Model 1. . . . .	49
4.34 The velocity magnitudes for the epiglottic fold angle values $f_{\text{angle}} = -16^\circ, 37^\circ, 89^\circ$ and vocal cord opening $v_{\text{open}} = 2.3 \text{ mm}$ , Model 1. . . . .	49
4.35 The epiglottic fold angle case study with different vocal cord openings, the resulting flow, Model 1. . . . .	50
4.36 The velocity magnitudes for the epiglottic fold angle values $f_{\text{angle}} = -16^\circ, 37^\circ, 89^\circ$ and false vocal cord height $fv_{\text{dist}} = 5.0 \text{ mm}$ , Model 1. . . . .	51

4.37	The velocity magnitudes for the epiglottic fold angle values $f_{\text{angle}} = -16^\circ, 37^\circ, 89^\circ$ and false vocal cord height $fv_{\text{dist}} = 7.8 \text{ mm}$ , Model 1 . . . . .	51
4.38	The epiglottic fold angle case study with different false vocal cord heights, the resulting flow, Model 1 . . . . .	52
4.39	The geometry and the iteration statistics, the converged simulation, $E = 50 \text{ kPa}$ , damping coefficient $\alpha = 0.5$ , iteration 4, the Model 1 with elasticity. . . . .	53
4.40	The geometry and the iteration statistics, no convergence, $E = 16 \text{ kPa}$ , damping coefficient $\alpha = 0.5$ , iteration 60, the Model 1 with elasticity. . . . .	54
4.41	The geometry plot and the iteration statistics, converged simulation, $E = 16 \text{ kPa}$ , damping $\alpha = 0.1$ , iteration 98, Model 1 with elasticity. . . . .	55
4.42	The laryngoscopic view of the supra-glottic obstruction condition closed state, the cross section identified (black line $CS$ ). . . . .	55
5.1	The initial attempt to design a 3D larynx model, the base geometry with the vocal chords. . . . .	58
5.2	An example of the human MRI cross section scan in the upper airway region (left) and the reconstructed geometry (right) [6]. . . . .	59
5.3	An example of the reconstructed geometry of the human upper airways from the MRI scans [6], the region of interest zoomed. . . . .	59
5.4	A laryngoscopic view of a reconstructed geometry of the human upper airways based on MRI scans [6]. . . . .	59
A.1	The sketch of the simple beam stretching, the left side fixed, the force applied on the right side and the tension applied on boundaries (left), a infinitesimal beam element with the respective extension (right). . . . .	63
B.1	The schematic representation of the case to be investigated, 2D. . . . .	66
B.2	A schematic representation of the region $II$ boundary, the comparison between the linear case and the polynomial case. . . . .	69
B.3	The precise representation of the transition regions with the linear boundary and the 7th order inverse polynomial boundary. . . . .	70

## List of Tables

2.1	COMSOL 4.2 predefined mesh size sets and the degrees of freedom for the Model 1 geometry (see Section 3) and the $P1 + P1$ and the $P2 + P1$ discretization. . . . .	14
-----	--	----



# 1 Introduction

For a long time, numerical simulations have been a great tool for understanding and exploring complicated cases. Because of huge advancements in the computer technology in recent times, the usage of the computer solutions has had a rapid increase. Also the computational fluid dynamics (CFD) has become irreplaceable aid in the education, the industry and even the medicine.

Medical conditions called asthma and exercise induced asthma (EIA) has been known and studied for quite some time. However, it is known that some of the EIA patients do not respond to asthma treatment. After careful investigations, Leif Nordang and his colleagues at the Uppsala University hospital (later referred to as our collaborators in Uppsala) suspect that in some cases, obstructions in the larynx region are responsible for the condition. Since the condition has not been separated from EIA up till recent times, there is no detailed analysis of air flow in the region of obstructions.

In the current chapter, a basic description of the medical background is given, an analysis of selected literature is performed, and goals of current work are outlined.

## 1.1 Short description of medical background

### 1.1.1 Basics of the larynx structure

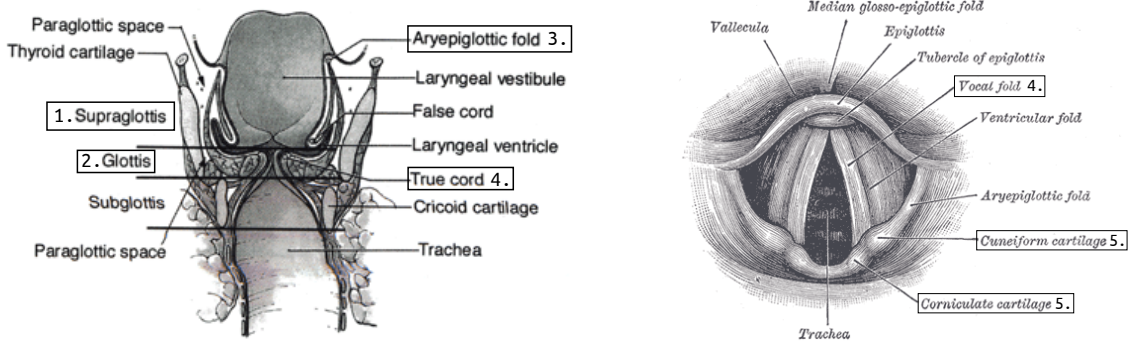


Figure 1.1: Left: vertical cross-section of larynx (from Mancuso et al. [7]). Right: laryngoscopic view of larynx (from Gray [4]). The parts of interest enumerated.

In general, the structure and the terminology of human airways is quite complex. In order to understand the problem considered in the current work, one must familiarize himself with

the very basic structure of the larynx and the terminology closely related to it. Two 2D representations, illustrating the larynx structure, are given in Fig. 1.1.

The left part of Fig. 1.1 illustrates the general division of the larynx in a glottic (around the vocal cords, denoted with number 1) and a supra-glottic (above the vocal cords, denoted with number 2) region. The aryepiglottic fold is denoted with number 3, and the vocal fold or the true cord (also known as the vocal chords) is denoted with number 4. The right part of Fig. 1.1 shows the larynx from a laryngoscopic view. The cartilages denoted with number 5 (can not be seen in left part of Fig. 1.1) will later on be called epiglottic fold.

The main function of aryepiglottic and epiglottic folds (denoted by 3 and 5) is suspected to be protection of the airways during swallowing phase. The function of the vocal cords is to create a voice sound during speech or other vocal activities. Sound is produced, when the vocal cord gap is reduced to a point, when the air outflow creates and sustains a vocal cord vibration (detailed process description falls outside the scope of this work). During physical activities, the vocal cord gap is usually very wide, to allow as big volumetric air flow as possible.

### 1.1.2 Exercise induced laryngeal obstruction (EILO)

Nordang et al. [13] (*in Swedish*) suggest that the EILO should be separated from EIA. Their findings are quite recent, hence the EILO has not been thoroughly investigated and not many medical doctors recognize it. As the name of the medical condition suggests, it is induced by intense physical activities (such as running, playing football and badminton), it is caused by laryngeal (airway near vocal cords) obstruction. Typical symptoms include choking and breathing problems.

Our collaborators in Uppsala suggest that the EILO should be divided in two classes:

1. Glottic EILO: the obstruction essentially is created by contraction of the vocal cords and the obstruction location is in the glottic region (Fig. 1.1, region 2);
2. Supra-glottic EILO: the obstruction is due to that the epiglottic fold (Fig. 1.1, structure 5) gets bent down, creating an obstruction, located in the supra-glottic region (Fig. 1.1, region 1).

In a real life situation, the EILO typically occurs as either as one of the described classes or as combination of both. An illustration for the glottic and the supra-glottic EILO classes separately is given in Fig. 1.2.

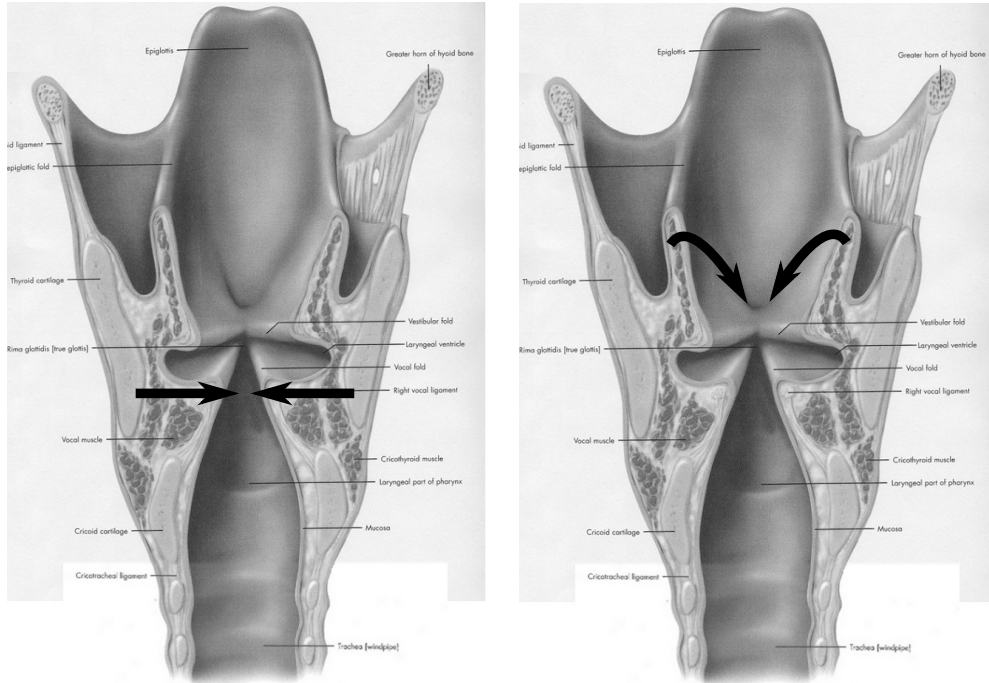


Figure 1.2: A vertical cross-section representation of the larynx [14]. The added arrows schematically illustrate the glottic EILO (left) and the supra-glottic EILO (right).

The nature of the glottic and supra-glottic EILO is quite different. However, both obstructions yield breathing problems and causes an inability to continue exercising. The present work will consider both conditions, with an increased focus at the supra-glottic EILO. Fig. 1.3 shows two images from a film of a patient, who is having the supra-glottic EILO [12]. The left and right image shows a closed and an opened state of the larynx, respectively. These images illustrate how the condition looks in real life from the laryngoscopic view.

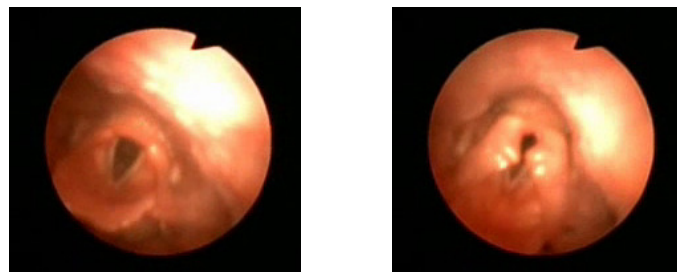


Figure 1.3: The laryngoscopic view of the supra-glottic obstruction condition [12], the open state (left) and the closed state (right).

## 1.2 Analysis of selected literature

### 1.2.1 Characteristics of the larynx

Eckel et al. [2] have performed extensive measurements and collected statistics for many human larynges. His work is very useful as a reference for medical purposes and also for computer simulation purposes. An example of schematics for some measurements of his work is given in Fig. 1.4.

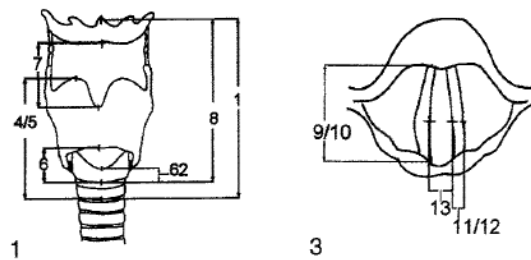


Figure 1.4: The example of schematics for some larynx measurements [2], height of the larynx (left) and the vocal cord dimensions (right).

Mermier et al. [8] have developed a method to determine a minute ventilation (breathing rate) from measuring heart rate. The method is later used by Zuurbier et al. [18] to determine the breathing rate of several pedestrians and cyclists. Their work suggests that the breathing rate of an exercising person can reach up to  $V_E = 100 \text{ l/min}$ .

### 1.2.2 CFD simulations in the larynx

Mylavaram et al. [11] evaluated the validity of the turbulence modeling for the air flow in the upper human airways by using multiple magnetic resonance imaging (MRI) axial scans of a real person. Their used geometry and the pressure probe locations are given in Fig. 1.5.

Mylavaram et al. [11] created a computer model and a physical model. They measured the pressure and the velocity at multiple points for physical model. For the numerical simulations, they used the software FLUENT 6.3 (Ansys, Lebanon, USA) and various turbulence models (unsteady large eddy simulations (LES), the steady  $k-\varepsilon$  model, the steady  $k-\omega$  standard model, the steady  $k - \omega$  shear stress transport model, and the steady Spalart–Allmaras model). In the simulations they used a peak flow rate  $Q$  of 200 l/min. Their conclusions are that the worst agreement between the simulations and the experiments is at the narrowest part of airways, and that the standard  $k - \omega$  model gives the smallest error approximately 20% on average.

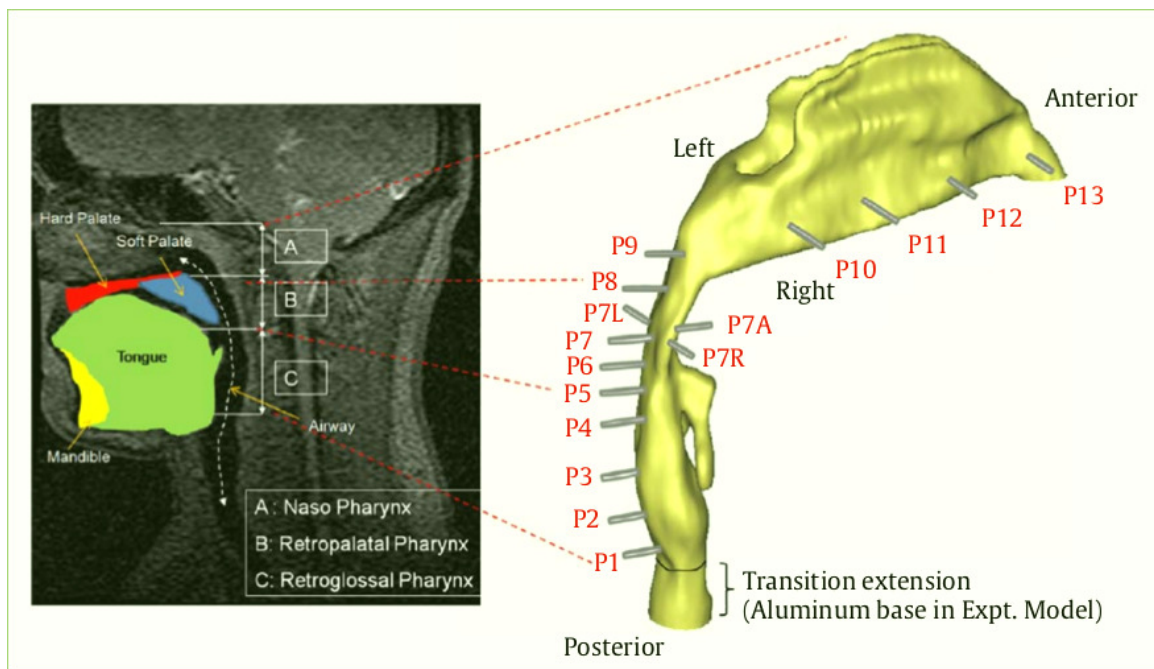


Figure 1.5: A sagittal image (left) and the deduced 3D geometry with pressure probes (right), not to scale. Mylavaram et al. [11] work.

Xi et al. [17] modelled air flow from the human upper airways down till the lungs. The main objective of their work was to check a flow through a simple larynx model. They studied the flow characteristics and aerosol deployment (particle transport). They did simulations for a relatively low flow rate  $Q = 15 - 30 \text{ l/min}$ . Xi et al. [17] predicted the turbulence using the low Reynolds number  $k - \omega$  model. Their conclusion was that an introduction of the vocal chords creates a laryngeal jet and can create an asymmetry in the particle transport. Such effect can be problematic for an asthma patient treatment with the aerosol.

A similar study by Lambert et al. [5] specifically targeted the aerosol delivery efficiency in the human airways using a particle tracking method together with the LES sub-grid scale (SGS) model. In the simulations, they constructed the geometry from a real person airway computed tomography (CT) scans. Lambert et al. [5] present results indicating asymmetric particle deposition, as predicted by Xi et al. [17].

Mihaescu et al. [9] performed unsteady flow simulations in the glottic region with the LES. In their work, a test 3D model of the vocal cords was designed to resemble the vocal cords in their closing phase. Mihaescu et al. [9] concluded that large intra-glottic vortices give an additional contribution to a contraction force and accelerate the closing phase of vocal cords.

## 1.3 Preliminary analysis

### 1.3.1 Flow characteristics

In the CFD simulation, general flow characteristics such as the flow velocity and the Reynolds number are important. The dimensions of the larynx are taken from Eckel et al. [2]. The average trachea diameter as  $d_{\text{main}} = 18.15 \text{ mm}$ , and the average vocal chord opening as  $v_{\text{open}} = 6.3 \text{ mm}$ . The flow rate is taken from Mermier et al. [8] as  $Q = 100 \text{ l/min}$ .

The maximal air velocity in the domain is located at the narrowest region in the larynx — near the vocal chords. Assuming a uniform velocity distribution and a rectangular vocal cord gap, one can estimate maximal air velocity,

$$u_{\text{flow}}^{(\max)} \approx \frac{Q}{v_{\text{open}} \cdot d_{\text{main}}} = \frac{100 \text{ l/min}}{6.3 \cdot 18.15 \text{ mm}^2} = \frac{1.667 \cdot 10^{-3} \text{ m}^3/\text{s}}{6.3 \cdot 18.15 \cdot 10^{-6} \text{ m}^2} \approx 14 \text{ m/s}, \quad (1.1)$$

$$u_{\text{flow}}^{(\max)} \approx 14 \text{ m/s} << 340 \text{ m/s} \approx c, \quad (1.2)$$

where  $c \approx 340 \text{ m/s}$  is the sound speed in air at  $T = 20^\circ\text{C}$ . It is concluded that the incompressible Navier–Stokes equations can be used.

For estimation of the Reynolds number, the flow parameters at the vocal cord gap are selected. For velocity scale, the obtained  $u_{\text{flow}}^{(\max)}$  is taken, and for the length scale, a shortest side  $v_{\text{open}}$  of the rectangular gap is taken. The chosen scales together with the kinematic viscosity of air yields following estimate of the Reynolds number:

$$\text{Re}_{\text{flow}} = \frac{u_{\text{flow}}^{(\max)} \cdot v_{\text{open}}}{\nu} = \frac{14 \cdot 6.3 \cdot 10^{-3}}{1.5257 \cdot 10^{-5}} \approx 5800 > 2000 \approx \text{Re}_c, \quad (1.3)$$

where  $\text{Re}_c \approx 2000$  is the critical Reynolds number for a transition from laminar to turbulent flow in a pipe. Although the  $\text{Re}_c$  is not known for the larynx, such relation can be seen as suggestion that the flow is turbulent.

### 1.3.2 Deformation characteristics

In order to determine the velocity of the epiglottic fold itself, the video with the EILO condition laryngoscopic view [12] was investigated. The average velocity of the epiglottic fold outer part is determined by counting frames between the opened and the closed state. The epiglottic fold closing time is observed to be approximately 8 frames, which yields the closing time scale

$$t_{\text{f,close}} \approx 8/25 \cdot 1 \text{ s} = 0.32 \text{ s}, \quad (1.4)$$

where 25 frames per second is the standard frame rate of PAL video. Assuming that the outermost line of the epiglottic fold has the largest velocity and travels on a quadrant with circular radius  $r \approx 7 \text{ mm}$  (estimated length of epiglottic fold), the maximal velocity of the

epiglottic fold will be

$$u_{\text{fold}}^{(\max)} \approx \frac{\pi}{2} \cdot \frac{r}{t_{\text{f,close}}} = 35 \text{ mm/s.} \quad (1.5)$$

The video with the EILO condition [12] shows that the epiglottic fold in closed state oscillates. However, it is difficult to distinguish an oscillatory movement, hence it is concluded that the oscillations are rather fast:

$$t_{\text{f,oscil}} \ll t_{\text{f,close}} = 0.32 \text{ s,} \quad (1.6)$$

where  $t_{\text{f,oscil}}$  is the closed state epiglottic fold oscillation time scale.

### 1.3.3 Time and velocity scales

The time scale of the turbulence is estimated from simple dimensional analysis (later tested in Section 4.1). The air flow, passing through the vocal chord gap, generates a jet with the velocity scale  $u_{\text{flow}}^{(\max)}$  and length scale  $v_{\text{open}}$ . It is assumed that the jet generates the largest oscillations with time scale

$$t_{\text{turb}} \approx \frac{v_{\text{open}}}{u_{\text{flow}}^{(\max)}} = \frac{6.3 \cdot 10^{-3}}{14} \approx 0.5 \text{ ms,} \quad (1.7)$$

where  $t_{\text{turb}}$  is the generated turbulence time scale, which can be compared to the epiglottic fold closing time scale (1.4). The summary of the obtained relations for the time scales:

$$t_{\text{f,oscil}} \ll t_{\text{f,close}} \quad (1.8)$$

$$t_{\text{turb}} \ll t_{\text{f,close}} \quad (1.9)$$

As later is explained, the current work is devoted to the epiglottic fold closing phase investigations. The closing phase has much larger time scale than the turbulence (1.9), therefore the turbulence effects can be averaged out using the RANS turbulence modelling. It is not clear, if the time scale for the epiglottic fold closed state oscillations is also larger than the turbulence time scale. However, these fast oscillations are not considered interesting.

One can also compare the flow velocity in the vocal cord region (1.1) with the estimated average epiglottic fold closing phase velocity (1.5):

$$u_{\text{flow}}^{(\max)} \approx 14 \text{ m/s} >> 35 \text{ mm/s} \approx u_{\text{fold}}^{(\max)}, \quad (1.10)$$

which suggest that a quasi-static approach for the fluid simulation can be used. The main assumption is that the fluid flow is so fast in comparison to the movement of the epiglottic fold, so that the flow adjusts to the epiglottic fold geometry change almost immediately. Hence one can use stationary Navier-Stokes equations.

It is assumed that the EILO occurs only during the inhalation phase, therefore the stationary solutions during only the inhalation phase are considered.

## 1.4 Goals of current work

As concluded from the literature study, no or very little attention has been paid to the flow in the near vicinity of the vocal chords. Existing studies are focused more on aerosol delivery efficiency, the vocal function and the dynamics of it, the turbulence effects and similar problems. No studies could be found that would consider geometry changes in the supra-glottic region, investigate the obstruction and its influence on the resulting flow. Our collaborators in Uppsala have expressed two conjectures based on experience:

- The supra-glottic EILO is more severe if the epiglottic fold distance from the vocal chords is smaller.
- The supra-glottic EILO can trigger the glottic obstruction in some cases.

The goals of the present work are:

1. Obtain quantitative relations between the flow rates and the different epiglottic fold blockage configurations.
2. Obtain quantitative relations between flow stresses and deformations of epiglottic fold.
3. Obtain qualitative conclusions about the numerical simulation predictions of the EILO process.
4. Test conjectures, outlined by our collaborators in Uppsala.
5. Improved understanding about the EILO condition and the air flow nearby.

## 2 CFD simulation

### 2.1 Selection of suitable simulation software

In order to carry out a numerical simulation, one need to select an appropriate software. There are various choices in the CFD field:

- A self written software.
- An open source software (for example, OpenFOAM).
- A commercial software (for example, FLUENT, COMSOL).

Using the self written software yields great understanding of the simulation procedures later to be used, however writing the software can be very time consuming. Open source software is free of charge, but usually requires long experience and knowledge base. The commercial software is usually the most user friendly, but it comes at a financial cost and sometimes at a cost of understanding.

There are various methods used in the numerical simulation software. The following methods are examples that can be found in CFD implementations:

- FDM – finite difference method.
- FVM – finite volume method (used in FLUENT, OpenFOAM).
- FEM – finite element method (used in COMSOL).

Due to its robustness, for a long time the FVM dominated the CFD field. However, recently FEM has become increasingly popular for CFD applications. The COMSOL software is built on FEM.

In the current work, the need for turbulence modelling has been identified (see Section 1.3.1). The self-written software has been dismissed due to insufficient time resources. The open source software has not been selected, mainly because a lack of knowledge base. The final choice is the commercial software COMSOL 4.2. A licence for COMSOL 4.2 is available, as well as experience in its use.

In this chapter, the main attention will be devoted to the COMSOL simulation software and the FEM that is utilized for the CFD simulations.

## 2.2 Description of COMSOL 4.2 simulation software

### 2.2.1 Basics of the FEM application to the CFD

The COMSOL 4.2 simulation software is entirely based on the FEM. The heart of the FEM is a variational formulation of the problem to be solved. Therefore the derivation of a variational form for the incompressible stationary Navier–Stokes equations is presented. The steady, laminar equations in the domain  $\Omega$  with non-slip and zero normal stress conditions on the boundaries  $\Gamma_0$  and  $\Gamma_n$  respectively in component form are

$$\begin{aligned} \rho u_j u_{i,j} &= -p_{,i} + \mu (u_{i,j} + u_{j,i})_{,j} && \text{in } \Omega, \\ u_{i,i} &= 0 && \text{in } \Omega, \\ u_i &= 0 && \text{on } \Gamma_0, \\ -pn_i + \mu (u_{i,j} + u_{j,i}) n_j &= 0 && \text{on } \Gamma_n. \end{aligned} \quad (2.1)$$

For the momentum equation a test function  $v_i$  is chosen such that  $v_i = 0$  on  $\Gamma_0$ . For the continuity equation a test function  $z$  is selected. The momentum and continuity equations are multiplied with test functions and integrated over the domain:

$$\begin{aligned} \rho \int_{\Omega} u_j u_{i,j} v_i \, dV &= - \int_{\Omega} p_{,i} v_i \, dV + \mu \int_{\Omega} (u_{i,j} + u_{j,i})_{,j} v_i \, dV, \\ \int_{\Omega} u_{i,i} z \, dV &= 0. \end{aligned} \quad (2.2)$$

Integration by parts applied to the pressure and viscous terms yields

$$- \int_{\Omega} p_{,i} v_i \, dV = - \int_{\Gamma_n} pn_i v_i \, dS + \int_{\Omega} p v_{i,i} \, dV, \quad (2.3)$$

$$\begin{aligned} \mu \int_{\Omega} (u_{i,j} + u_{j,i})_{,j} v_i \, dV &= \mu \oint_{\partial\Omega} (u_{i,j} + u_{j,i}) n_j v_i \, dS - \mu \int_{\Omega} (u_{i,j} + u_{j,i}) v_{i,j} \, dV = \\ &= \mu \int_{\Gamma_n} (u_{i,j} + u_{j,i}) n_j v_i \, dS - \frac{\mu}{2} \int_{\Omega} (u_{i,j} + u_{j,i}) (v_{i,j} + v_{j,i}) \, dV. \end{aligned} \quad (2.4)$$

The sum of the boundary terms from the equations (2.3)–(2.4) give zero stress boundary condition integral

$$- \int_{\Gamma_n} pn_i v_i \, dS + \mu \int_{\Gamma_n} (u_{i,j} + u_{j,i}) n_j v_i \, dS = \int_{\Gamma_n} [-pn_i + \mu (u_{i,j} + u_{j,i}) n_j] v_i \, dS = 0. \quad (2.5)$$

Putting expressions (2.3)–(2.5) back in the integral expression (2.2) gives the final variational form

$$\rho \int_{\Omega} u_i u_{i,j} v_i \, dV = \int_{\Omega} p v_{i,i} \, dV - \frac{\mu}{2} \int_{\Omega} (u_{i,j} + u_{j,i}) (v_{i,j} + v_{j,i}) \, dV, \quad (2.6)$$

$$\int_{\Omega} u_{i,i} z \, dV = 0. \quad (2.7)$$

The non-slip boundary condition (on  $\Gamma_0$ ) is enforced explicitly on the FEM functions with appropriate selection of the function space. The zero normal stress boundary condition (on  $\Gamma_n$ ) is implicitly enforced through the variational form.

In the incompressible flow case there are 4 independent unknowns — 3 velocity components and the pressure. Individual discretization for each independent variable can in principle be chosen. It is a general knowledge that different combinations have different properties.

It is common practice to use separate discretizations for the velocity and the pressure. The simplest case would be to use continuous, piecewise linear elements for both variables. Such a combination is called the  $P1 + P1$  discretization. However, it is well known that such numerical discretization without modifications yields high pressure oscillations (discretization is unstable). Another option is to choose continuous piecewise quadratic elements for the velocity, but linear elements for the pressure. Such a combination is called the  $P2 + P1$  discretization or the Taylor–Hood pair. It has been proven that the  $P2 + P1$  discretization is stable [3].

The representation of  $P1 + P1$  and  $P2 + P1$  discretizations on a single triangular element (evaluation points for the function values are marked with the black dots) is given in Fig. 2.1.

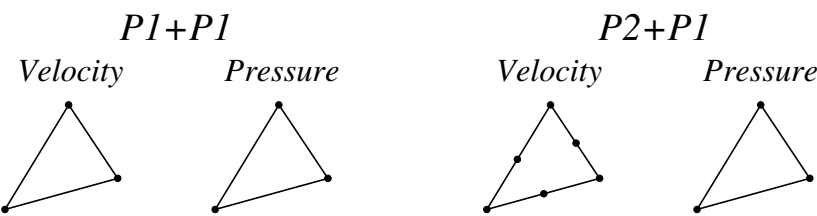


Figure 2.1: Example of the  $P1 + P1$  (left) and the  $P2 + P1$  (right) FEM dicretizations for the Navier–Stokes equations.

In the COMSOL 4.2 simulation software it is possible to change the discretization. The default COMSOL 4.2 setting is the  $P1 + P1$  discretization. The COMSOL software deals with the  $P1 + P1$  oscillations using stabilization techniques — a streamline and a cross-wind diffusion (enabled by default) and an isotropic diffusion (disabled by default). More information can be found in the COMSOL 4.2 CFD users guide pages 193 – 194.

### 2.2.2 Turbulence modelling in COMSOL 4.2

In order to obtain an access to any kind of turbulence models, a CFD module for the COMSOL software must be purchased separately. The basic COMSOL package admits only a laminar CFD solver. One option is to write a turbulence model from scratch using a *PDE* mode. Such an approach is dismissed due to the complexity of a reasonable turbulence model.

COMSOL 4.2 includes four industry-standard RANS turbulence models, a  $k - \varepsilon$ , a Low Reynolds number  $k - \varepsilon$ , a Spalart-Allmaras and a  $k - \omega$  model. As concluded from the literature study, the best match with the experiments for the boundary pressure (allowing 20% error on average) is given by the standard  $k - \omega$  model (see Section 1.2.2). The same model is selected for the current work and will be described in more details in this section.

Both in the FLUENT 6.3 and the COMSOL 4.2 software, the  $k - \omega$  turbulence model implementation is based on Wilcox [16] work. Therefore one can assume that the verification [11] done with FLUENT 6.3 applies also for the simulations with the COMSOL 4.2 software.

The  $k - \omega$  turbulence model describes the turbulent kinetic energy  $k$  and the specific dissipation rate  $\omega$  evolution in the simulation domain and relates variables back to the Reynolds stress tensor. The equations are given below in component notation:

$$\rho u_j u_{i,j} = -p_{,i} + [(\mu + \mu_T)(u_{i,j} + u_{j,i})]_{,j} - \frac{2}{3}\rho k_{,i}, \quad (2.8)$$

$$u_{i,i} = 0, \quad (2.9)$$

$$\rho u_i k_{,i} = [(\mu + \mu_T \sigma_k^*) k_{,i}]_{,i} + P_k - \rho \beta^* k \omega, \quad (2.10)$$

$$\rho u_i \omega_{,i} = [(\mu + \mu_T \sigma_\omega) \omega_{,i}]_{,i} + \alpha \frac{\omega}{k} P_k - \rho \beta \omega^2, \quad (2.11)$$

$$\mu_T = \rho \frac{k}{\omega}, \quad (2.12)$$

$$P_k = \mu_T u_{i,j} (u_{i,j} + u_{j,i}), \quad (2.13)$$

where  $\mu_T$  is the turbulent viscosity and  $\sigma_k^*$ ,  $\beta^*$ ,  $\sigma_\omega$ ,  $\alpha$ , and  $\beta$  are the closure coefficients (for more details see the COMSOL 4.2 CFD users guide pages 151 – 153). Equation (2.8) is the momentum conservation law, equation (2.9) the mass conservation law, equations (2.10) – (2.11) the diffusion expressions for  $k$  and  $\omega$ , equation (2.12) turbulent viscosity definition and equation (2.13) an auxiliary expression.

### 2.2.3 Meshing procedures in COMSOL 4.2

In order to commence the FEM simulation, the computational domain must be meshed. COMSOL 4.2 software includes various meshing methods and many adjustable properties. A short description is given in the current section.

The COMSOL 4.2 mesh generation routines can be used in two different ways:

1. With a physics controlled mesh – only minimal control, a global mesh size variable.
2. With a user controlled mesh – complete control (refinements, element types, etc).

The triangular meshes are generated either using the Delaunay triangulation or an advancing front technique. The setting can be changed under *advanced* tab for free triangular operation.

The default settings in COMSOL 4.2 for a CFD mesh are a free triangular mesh with an increased resolution at curved surfaces and with a boundary layer mesh (rectangular prolonged elements near surfaces). An example mesh near a curved surface with the default settings is given in Fig. 2.2. One can also use a purely triangular mesh. An example mesh for the same region is given in Fig. 2.3.

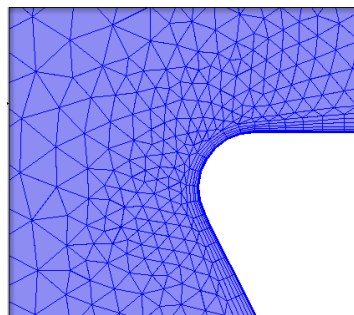


Figure 2.2: The default CFD mesh, generated by the COMSOL 4.2 near the curved surface.

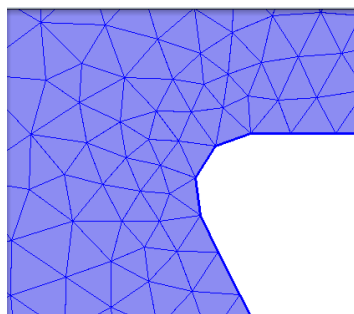


Figure 2.3: The pure triangular CFD mesh, generated by the COMSOL 4.2 near the curved surface.

Both types of meshes with various sizes are tested in the current work. For the mesh size, one can use predefined sizes or custom sizes. In COMSOL 4.2 there are 9 predefined size pre-sets, from *extremely fine* to *extremely coarse*. These pre-sets are available both in the physics controlled meshing (as the only controllable variable) and also in the user controlled meshing size option. The defined sets together with limits on the element sizes for the triangular mesh and the degrees of freedom (DOF) for the Model 1 geometry (see Section 3) with the  $P1 + P1$  and the  $P2 + P1$  discretization are given in Tab. 2.1.

In later chapters, the mesh level is denoted with the  $M_{\text{size}}$  parameter. The specific settings as a maximal element size  $h_{\max}$  and a minimal element size  $h_{\min}$  are shown in Tab. 2.1.

	$M_{\text{size}}$	$h_{\max}$	$h_{\min}$	DOF, $P1 + P1$	DOF, $P2 + P1$
Extremely fine	1	0.152 mm	0.004 mm	$\approx 3.0 \cdot 10^5$	$\approx 1.0 \cdot 10^6$
Extra fine	2	0.295 mm	0.034 mm	$\approx 8.2 \cdot 10^4$	$\approx 2.8 \cdot 10^5$
Finer	3	0.635 mm	0.091 mm	$\approx 2.7 \cdot 10^4$	$\approx 8.9 \cdot 10^4$
Fine	4	0.794 mm	0.227 mm	$\approx 1.5 \cdot 10^4$	$\approx 5.1 \cdot 10^4$
Normal	5	1.02 mm	0.454 mm	$\approx 8.6 \cdot 10^3$	$\approx 2.8 \cdot 10^4$
Coarse	6	1.52 mm	0.681 mm	$\approx 4.3 \cdot 10^3$	$\approx 1.4 \cdot 10^4$
Coarser	7	1.97 mm	0.908 mm	$\approx 2.8 \cdot 10^3$	$\approx 8.9 \cdot 10^3$
Extra coarse	8	2.95 mm	1.13 mm	$\approx 1.6 \cdot 10^3$	$\approx 5.0 \cdot 10^3$
Extremely coarse	9	4.99 mm	1.59 mm	$\approx 9.5 \cdot 10^2$	$\approx 2.9 \cdot 10^3$

Table 2.1: COMSOL 4.2 predefined mesh size sets and the degrees of freedom for the Model 1 geometry (see Section 3) and the  $P1 + P1$  and the  $P2 + P1$  discretization.

## 2.2.4 Solvers in COMSOL 4.2

The term *solver* in COMSOL 4.2 includes everything from the equation compilation to a sparse matrix solver. The stationary solver sequence for CFD with the  $k - \omega$  turbulence model contains two separate steps, one for the turbulence variables  $k$  and  $\omega$ , and a second one for the flow variables  $p, \vec{u}$ . The sequence is given in Fig. 2.4.

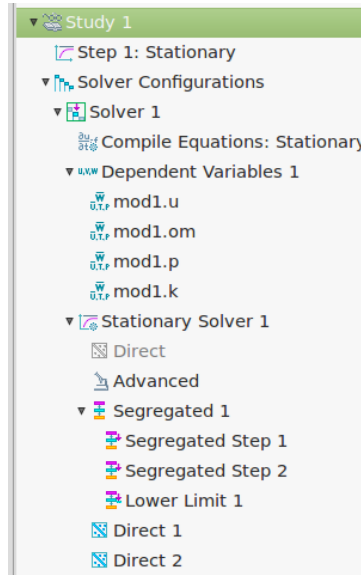


Figure 2.4: COMSOL 4.2 solver sequence for stationary CFD solutions with the  $k - \omega$  turbulence model.

In the current work, the default solver sequence for the *stationary solver* and a *time dependent solver* is used. Within the sequence, the direct solver for a sparse system of equations is used. It is selected because of its robustness and speed for 2D simulations.

For the *time dependent solver*, the default second-order backward difference scheme with an adaptive time step is used. The assumption can be made that the adaptive time step can resolve all time scales up to the selected mesh precision.

## 2.3 Selection of suitable boundary conditions

In order to complete the numerical simulation description, one must set appropriate boundary conditions. The boundary conditions are explained in the current section. The actual boundary shapes are developed in Section 3.

After discussions with our collaborators in Uppsala, it was determined that a suitable condition would be a fixed pressure drop over the considered larynx region. This condition would roughly resemble a constant lung suction. However, in the FEM implementation of the Navier-Stokes equations, setting such condition is not possible. Therefore a workaround is developed. At the inlet boundary, a fixed velocity profile is set, at the outlet boundary a zero normal stress is set, and the amplitude of the input velocity profile is adjusted until the required pressure drop is obtained.

In the current work the non-slip boundary condition is assumed to be a good enough approximation for the larynx walls. In order to reduce the complexity of computations, a symmetry boundary is also used.

The summary of selected boundary conditions (see Fig. 2.5):

1. **Inlet**  $\partial I$  – fixed normal velocity profile.
2. **Walls**  $\partial W$  – no slip condition.
3. **Outlet**  $\partial O$  – zero normal stress.
4. **Center**  $\partial C$  – symmetry condition.



Figure 2.5: A generic sketch of the computational domain.

The expression and the meaning of mentioned boundary conditions are different between the case with and the case without turbulence modelling. The main difference is the turbulence variable conditions at the boundaries. Especially complicated is the no-slip or wall condition in the turbulence case. The complications arise from high gradients in the flow. One of possible solutions is to use the so-called wall functions, which is used in the current work.

The summary of the selected boundary conditions in component form for the case with no turbulence modelling is given below:

$$\text{Inlet: } u_i = -U_0(x, y) \cdot n_i, \quad (2.14)$$

$$\text{Wall: } u_i = 0, \quad (2.15)$$

$$\text{Outlet: } [-p\delta_{ij} + \mu(u_{i,j} + u_{j,i})]n_j = 0, \quad (2.16)$$

$$\text{Center: } u_i n_i = 0; \quad K_i - (K_j n_j) n_i = 0; \quad (2.17)$$

$$K_i = \mu(u_{i,j} + u_{j,i})n_j,$$

where  $\vec{n}$  is the normal of each boundary and  $\vec{K}$  is an auxiliary vector. The most non-intuitive boundary conditions can be easily explained. Assuming the 2D case and  $n_x = 0, n_y = 1$ , relation (2.16) becomes:

$$\mu \left( \frac{\partial u_x}{\partial y} + \frac{\partial u_y}{\partial x} \right) = 0 \text{ and } -p + 2\mu \frac{\partial u_y}{\partial y} = 0, \quad (2.18)$$

which is the common expression for zero normal stress in this specific boundary orientation case. Assuming  $n_x = 1, n_y = 0$ , relation (2.17) becomes:

$$u_x = 0 \text{ and } \mu \frac{\partial u_y}{\partial x} = 0, \quad (2.19)$$

which is the common expression for the symmetry condition in this specific boundary orientation case. The boundary conditions in case with turbulence modelling are as follows:

$$\text{Inlet: } u_i = -U_0(x, y)n_i; \quad k = \frac{3}{2}(U_0 I_T)^2; \quad \omega = \frac{k^{1/2}}{(\beta_0^*)^{1/4} L_T}, \quad (2.20)$$

$$\begin{aligned} \text{Wall: } u_i n_i &= 0; \quad \left[ (\mu + \mu_T)(u_{i,j} + u_{j,i}) - \frac{2}{3}\rho k \delta_{ij} \right] n_j = -\rho \frac{u_\tau}{\delta_w^+} u_i; \\ k_{,i} n_i &= 0; \quad \omega = -\rho \frac{k}{\kappa_v \delta_w^+ \mu}, \end{aligned} \quad (2.21)$$

$$\begin{aligned} \text{Outlet: } &\left[ -p \delta_{ij} + (\mu + \mu_T)(u_{i,j} + u_{j,i}) - \frac{2}{3}\rho k \delta_{ij} \right] n_j = 0; \\ k_{,i} n_i &= 0; \quad \omega_{,i} n_i = 0, \end{aligned} \quad (2.22)$$

$$\text{Center: } u_i n_i = 0; \quad k_{,i} n_i = 0; \quad \omega_{,i} n_i = 0; \quad K_i - (K_j n_j) n_i = 0; \quad (2.23)$$

$$K_i = \left[ (\mu + \mu_T)(u_{i,j} + u_{j,i}) - \frac{2}{3}\rho k \delta_{ij} \right] n_j.$$

The inlet expression (2.20) contains the turbulence intensity  $I_T$  and the turbulence length scale  $L_T$ . Values of those parameters are taken from the work of Mylavarapu et. al [11] as  $I_T = 10\%$  and  $L_T = 1$  mm.

The wall expression (2.21) contains the friction velocity  $u_\tau = C_\mu^{1/4} \sqrt{k}$  and the wall distance in viscous units  $\delta_w^+ = \rho u_\tau \delta_w / \mu$ . The wall distance  $\delta_w$  is computed automatically so that  $\delta_w^+ = 11.06$  holds, which roughly corresponds to the place where the logarithmic layer meets the viscous sub-layer. Such correspondence is a reasonable approximation for attached flows. For detached flows the division in a logarithmic layer and viscous sub-layer is not an accurate description and corrections in wall treatment must be made [10]. In current work such corrections are not investigated. A schematic representation of the wall distance is given in Fig. 2.6.

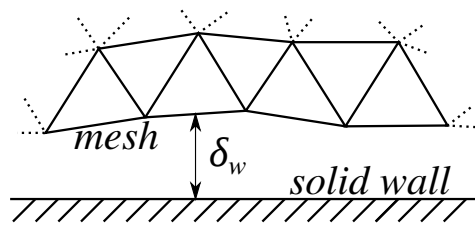


Figure 2.6: An illustration of the wall function boundary condition for the turbulence modelling.

The computed wall distance can be used as an additional criteria to determine if the obtained result is with reasonable accuracy. The wall distance should be much smaller than the typical dimensions. The wall distance results were investigated for selected cases, and the distance were mostly reasonable. As expected from the attached flow wall function formulation, the flow separation region seemed most problematic.

A detailed explanation for the other boundary conditions is not given due to their complexity.



### 3 Developed test models and conditions

During a visit at the department of Otolaryngology, Uppsala University Hospital, possible test models were discussed. We agreed to start with a very simple qualitative 2D model, that could be used to obtain a preliminary understanding of the fluid flow. The initial model is later on advanced it to an improved 2D model. Finally the improved model 2D model is complemented with an elastic description determining the quasi-stationary epiglottic fold dynamics. In the current chapter the development of model geometry approximations and an elasticity model for the epiglottic fold is described in more details.

#### 3.1 Development of model geometries

##### 3.1.1 Preliminary 2D geometry, Model 0

As previously discussed, for the supra-glottic EILO there are essentially two objects that block the air path — the vocal cords themselves and the supra-glottic obstacle (the epiglottic fold). Hence it could be of interest to investigate the air flow trough a simple structure with two obstacles.

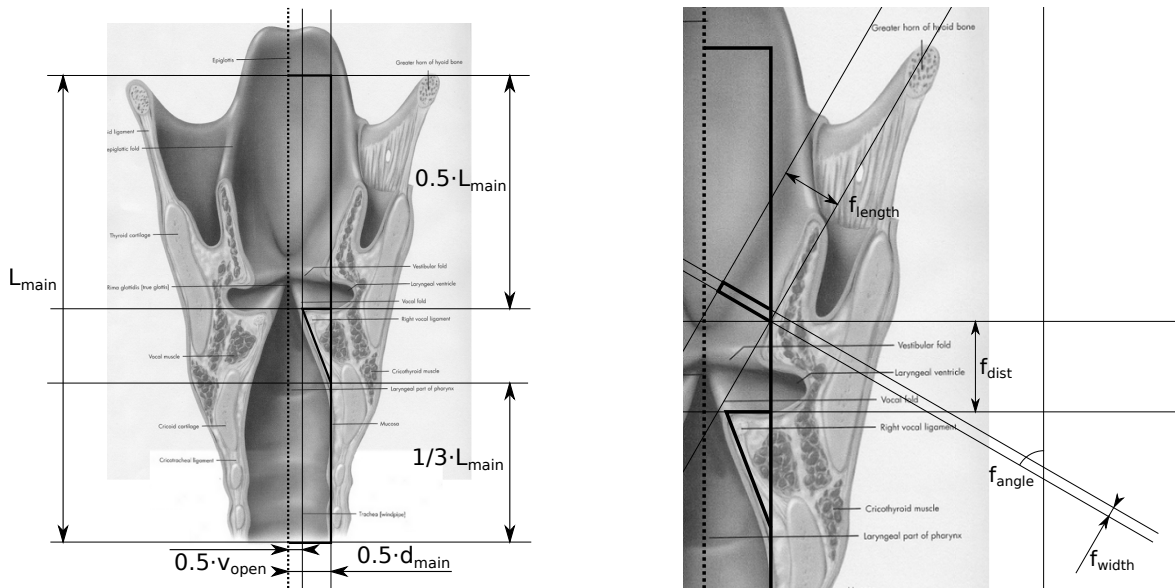


Figure 3.1: Model 0 geometry approximation over the larynx cross section image [14], a global geometry with the vocal chords (left) and an epiglottic fold design (right).

In order to simplify the numerical task, it is assumed that one can use a planar-symmetric representation of the problem. A sketch of the Model 0 geometry approximation is given in Fig. 3.1. For a better representation of the actual simulation domain, a full 3D representation sketch is given in Fig. 3.2.

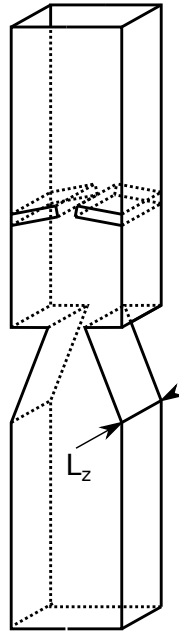


Figure 3.2: 3D representation sketch of the larynx Model 0 geometry approximation with  $L_z$  as the length in the  $\hat{z}$  dimension.

The corners of the inner geometry (apart from the inlet and the outlet) are rounded (filleted) before the actual simulations in order to avoid numerical problems in the corners.

The main parameters are taken as an average of data concerning man, presented by Eckel et al. [2]. The values taken are the main length of the larynx  $L_{\text{main}} = 71.3$  mm, the main diameter of the trachea (lowest part of the larynx)  $d_{\text{main}} = 18.15$  mm and the vocal cord opening size  $v_{\text{open}} = 6.3$  mm. The depth  $L_z = 14.25$  mm is selected to match the cross section in the rectangular case with the cross section of the circular. The epiglottic fold width is roughly estimated to be  $f_{\text{width}} = 1.5$  mm. The value of the epiglottic fold distance is roughly estimated to be  $f_{\text{dist}} = 8.0$  mm and the epiglottic fold length  $f_{\text{length}} = 7.0$  mm. The epiglottic fold angle  $f_{\text{angle}}$  is assumed to be within an interval  $f_{\text{angle}} \in [90^\circ, 20^\circ]$ , where  $f_{\text{angle}} = 90^\circ$  means a completely bent down epiglottic fold, and  $f_{\text{angle}} = 20^\circ$  means a completely opened epiglottic fold (the value is selected to be  $20^\circ$  in order to avoid problems with the geometry generation).

### 3.1.2 The improved 2D geometry, Model 1

In order to better describe the larynx geometry and obtain more reasonable results, an improved geometry approximation Model 1 is developed. A sketch of the Model 1 geometry

approximation over the larynx cross section image is shown in Fig. 3.3.

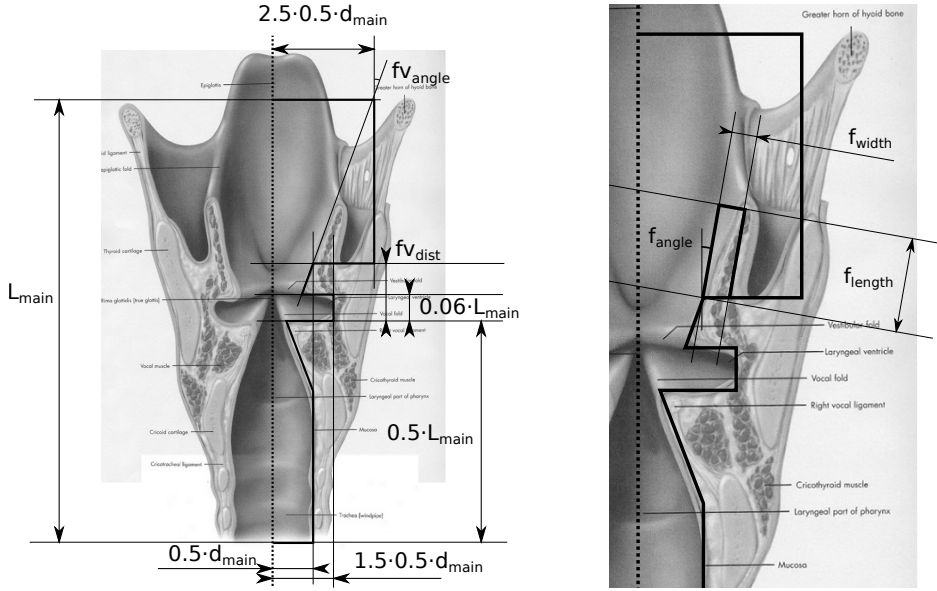


Figure 3.3: The larynx Model 1 geometry approximation over the larynx cross section image [14], a global geometry with vocal chord (left) and the epiglottic fold design (right).

Similar as for Model 0, the corners of the inner geometry before actual simulations are filleted. If compared to the Model 0, the false vocal cord angle parameter has been added. The false vocal cord angle with respect to vertical is determined from the cross section representation to be  $fv_{\text{angle}} = -20^\circ$ . The distance of the epiglottic fold is now determined by the false vocal cord thickness  $fv_{\text{dist}}$  (Fig. 3.3, left). For all other parameters the same values as before are used. Due to the used filleting, the epiglottic fold angle interval is taken  $f_{\text{angle}} \in [90^\circ, -16^\circ]$ .

One must note that the geometry approximations of the specific models are based mostly on the proportions read from the cross sectional representation of the larynx. Only a few main parameters, that can be clearly identified, are taken from real measurements.

## 3.2 Simulation methodology

To investigate results for different epiglottic fold configurations, a reference simulation for the flow rate  $Q = 100 \text{ l/min}$  is done, and a reference pressure drop  $\Delta P_{\text{ref}}$  is obtained. For Model 0, the reference simulation is done without the epiglottic fold; for Model 1, the reference simulation is done with the epiglottic fold in an upright position. Then, the epiglottic fold is added or bent down, and a solution is found iteratively by guessing the flow rate  $Q$  to obtain the same  $\Delta P = \Delta P_{\text{ref}}$  (up to the precision  $\varepsilon$ ). A sketch of process is given in Fig. 3.4.

After the pressure drop is matched, one can investigate results, such as the velocity field,

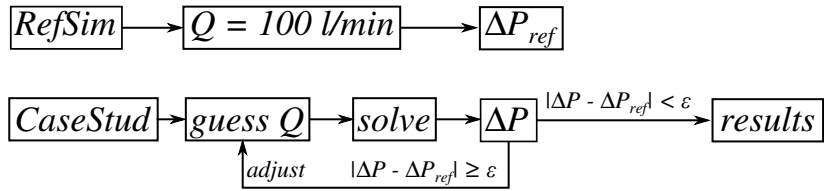


Figure 3.4: A block scheme representation of the Model 0 and the Model 1 simulation methodology.

the resulting flow, the generated pressure. The flow rate  $Q$  is modified using the empirical relation

$$Q^{(i+1)} = \left(1 - \frac{1}{2} \frac{\Delta P_{\text{err}}}{\Delta P_{\text{ref}}}\right) Q^{(i)}, \quad (3.1)$$

where  $Q^{(i)}$  is the guessed flow rate at an iteration  $i$  and the  $\Delta P_{\text{err}}$  is error of the obtained pressure drop. In the numerical simulations, initial flow  $Q$  guess is taken as 100 l/min or as the result from the previous simulation. The process typically converge in 2 – 4 iterations.

### 3.3 Description of the epiglottic fold elasticity

#### 3.3.1 Simple 1D continuous elastic description

In this work only stationary elasticity is considered, a motivation of this choice can be found in Section 1.3.3. Only dependence on one direction is assumed, hence arriving with a 1D elasticity model. For convenience, the derivation of beam stretching equation is given in appendix A. The main relation needed for derivations in this section is the relation between force and deformation

$$F(x) = E \cdot S(x) \cdot \frac{dx'}{dx} = E \cdot S(x)\varepsilon, \quad (3.2)$$

where  $x$  is original position,  $x'$  is deformed position,  $\varepsilon = dx'/dx$  is deformation, and  $F(x)$  is an elasticity force at a position  $x$  in a stretched beam with a cross section area  $S(x)$  and Young modulus  $E$ .

In the bending case, the situation is viewed a bit differently compared to the stretching case. In the bending case one usually work with a bending angle  $\varphi$  in respect to the horizon ( $x$  axis), while in the stretching case one usually work with the deformed coordinate  $x'$ . In the stretching case a non-deformed situation reduces to  $x' = x$ , while in the bending case the non-deformed situation reduces to  $\varphi(s) = \varphi_0(s)$  (in the current work only a special case  $\varphi(s) = \varphi_0 = \text{const}$  is considered), where the  $\varphi_0(s)$  describes an initial curvature. The angle distribution  $\varphi(s)$  together with a thickness distribution  $D(s)$  describes the beam shape.

It is assumed that the central line of the beam (from now on called the *centroid*) remains undeformed. Since the length is constant, it makes sense to put an axis along the centroid. A sketch of the described setup is given in Fig. 3.5.

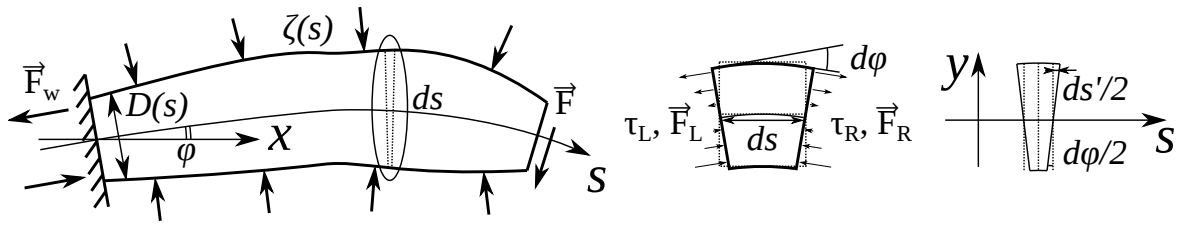


Figure 3.5: Sketch of a simple beam bending, one end fixed, a force on the other end and a load on boundaries applied (left), a small bent beam element (middle) and the relation to the linear stretching (right).

One can select an infinitesimal beam element, that is sufficiently small to assume that the  $s$  axis is straight in that region, and also the width of the beam is constant  $D(s) \approx const.$

In order to relate the torque at the infinitesimal beam element (middle part of Fig. 3.5), one can relate the bending with the simple linear stretching. According to the analytical geometry relations, from right part of Fig. 3.5 we get:

$$\frac{ds'}{2} = \frac{d\varphi}{2} \cdot y. \quad (3.3)$$

The relation implicitly contains the assumption that the deformation on the centroid is zero, hence  $ds'|_{y=0} = 0$ . Deformation in this case can be written as  $\varepsilon = ds'/ds$ . Consequently, the force amplitude on the right side of the infinitesimal beam element is

$$dF_R(y) = E \cdot dS \cdot \varepsilon = E \cdot dS \cdot \frac{ds'}{ds} = E \cdot dS \cdot \frac{d\varphi}{ds} \cdot y = E \cdot L_z \cdot dy \cdot \frac{y}{R(s)}, \quad (3.4)$$

where  $R(s)$  is a curvature radius of the beam centroid. One can also deduce a maximal linear deformation at the sides of the beam caused by the bending

$$\varepsilon_{max} = \varepsilon|_{y=\pm D(s)} = \pm \frac{d\varphi}{ds} \frac{D(s)}{2} = \pm \frac{D(x)}{2R(s)}. \quad (3.5)$$

In order to obtain the torque around a point on the centroid, one can integrate the momentum  $y \cdot dF_R(y)$  over the cross section and obtain

$$\tau_R(s) = \int_{-D(s)/2}^{D(s)/2} y \cdot dF_R(y) = \frac{E \cdot L_z}{R(s)} \int_{-D(s)/2}^{D(s)/2} y^2 dy = \frac{E \cdot L_z}{R(s)} \left[ \frac{y^3}{3} \right]_{-D(s)/2}^{D(s)/2} = \frac{E \cdot L_z}{R(s)} \frac{D^3(s)}{12}. \quad (3.6)$$

For a stationary state, the force and the torque is in equilibrium, hence  $\tau_R(s) = -\tau_L(s) = \tau(s)$  and thus the differential equation for the bending angle is

$$E \cdot \frac{L_z D^3(s)}{12} \frac{d\varphi}{ds} = \tau(s). \quad (3.7)$$

To obtain the load  $\zeta(s)$  (a linear force density) relation, one can differentiate expression (3.7) twice with respect to the centroid coordinate. The first differentiation yields a shear force distribution  $F_{sh}(s)$ , and the second differentiation yields the linear force density or the load  $\zeta(s)$ . The final differential equation for the bending description is

$$\frac{d^2}{ds^2} \left( E \cdot \frac{L_z D^3(s)}{12} \frac{d\varphi}{ds} \right) = \zeta(s). \quad (3.8)$$

For the case when the bending angle  $\varphi$  is small, the curved coordinate  $s$  can be approximated up to a good precision with a straight coordinate  $s \approx x$  and the bending angle as a deflection  $w$  (the centroid distance from  $x$  axis) derivative  $\varphi \approx dw/dx$ . In such case equation (3.8) is essentially the Euler–Bernoulli beam equation with an explicitly derived second momentum of inertia

$$\frac{d^2}{dx^2} \left( EI \frac{d^2w}{dx^2} \right) = \zeta(x); \quad I = \frac{L_z D^3(x)}{12}. \quad (3.9)$$

A final note is that, in the 2D case, the pressure  $P$  can be used instead of the load  $\zeta$ . The equation (3.8) can be rewritten as

$$\frac{d^2}{ds^2} \left( E \cdot \frac{D^3(s)}{12} \frac{d\varphi}{ds} \right) = \frac{\zeta(s)}{L_z} = P(s). \quad (3.10)$$

### 3.3.2 Methodology for the CFD simulation with an incorporated 1D elasticity

In order to carry out a complete simulation of the fluid and the elastic epiglottic fold, one must tie both descriptions together. In present section a solution for the task is explained.

The geometry approximation is essentially the same as described in the Section 3.1.2, with only a small change. The epiglottic fold is not approximated as a solid rectangle, instead it is approximated using piecewise linear approximations (see Fig. 3.6). The shape is determined by angle distribution  $\varphi(s)$  in respect to vertical and the width distribution  $D(s)$ . An example of generated curved epiglottic fold shape with a rough discretization and a fine discretization is shown in Fig. 3.7.

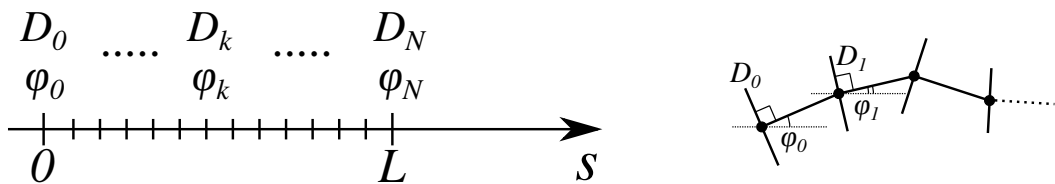


Figure 3.6: A sketch of the epiglottic fold shape data representation (left) and the shape skeleton construction (right).

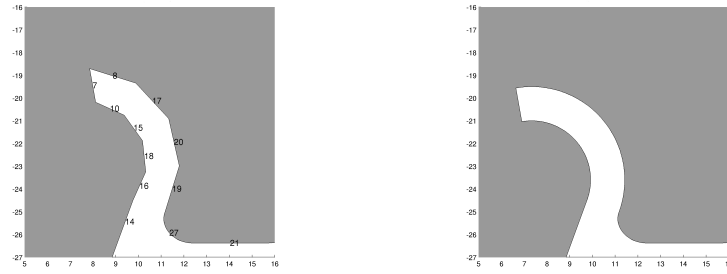


Figure 3.7: Epiglottic fold shapes generated with a rough resolution (left) and a fine resolution (right).

After the geometry has been generated, the CFD simulation can be carried out as described in Section 2. The simulation yields (amongst other information) the pressure on the boundary of the generated epiglottic fold. The boundary and the parametric pressure plot in respect to  $x$  coordinate is given in Fig. 3.8.

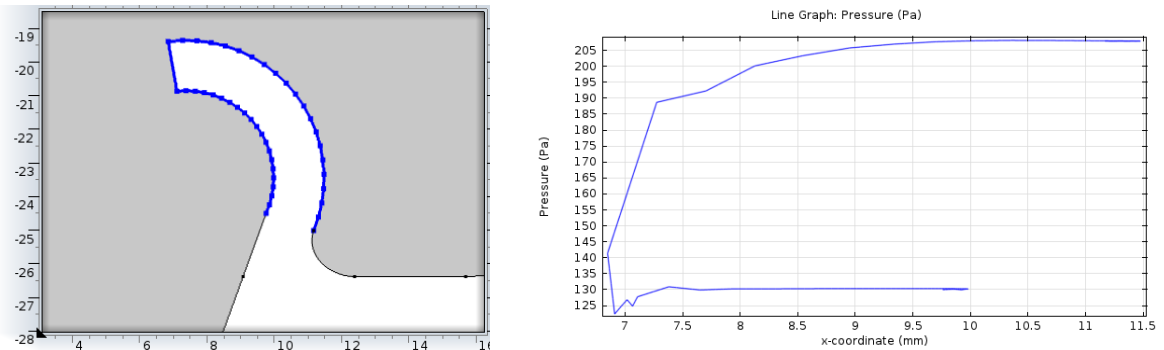


Figure 3.8: A selection of the epiglottic fold boundary (left) and the parametric pressure plot over the surface in respect to the  $x$  coordinate (right).

When the pressure (or any other force density) distribution over the epiglottic fold surface is obtained, one can map the force density data to the 1D elasticity problem load. In the current work the force density is evaluated at the epiglottic fold side points and the load is calculated as a difference between the side force densities. A schematic representation of the mapping is given in Fig. 3.9.

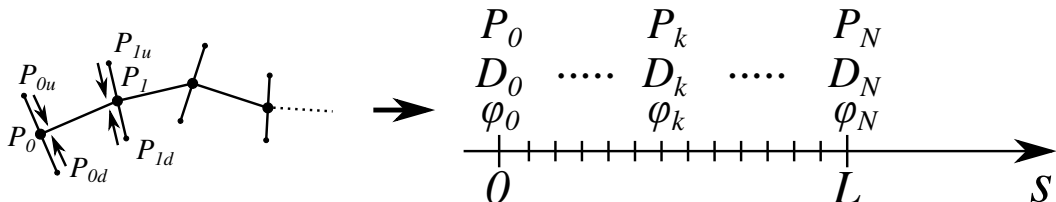


Figure 3.9: A construction of the 1D load from the epiglottic fold boundary force densities (left) and the representation on 1D mesh (right).

To get the actual load, one must select a force density to measure. The load mapping is tested for the pressure and for the total stress normal component (the pressure and the viscous force). The test shapes and the obtained load graphs are shown in Fig. 3.10 and Fig. 3.11.

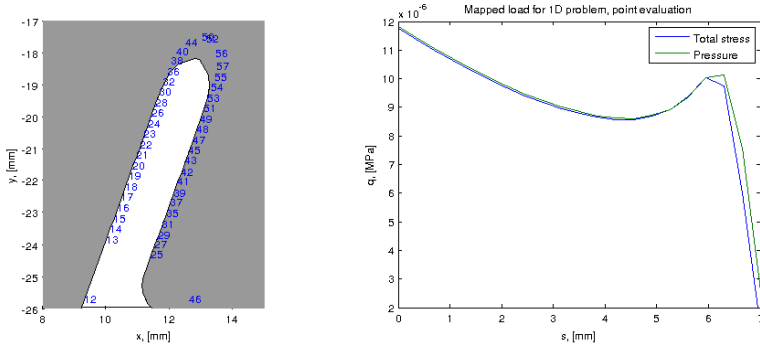


Figure 3.10: The shape of the first epiglottic fold (left) and the mapped load from the pressure and the total stress (right).

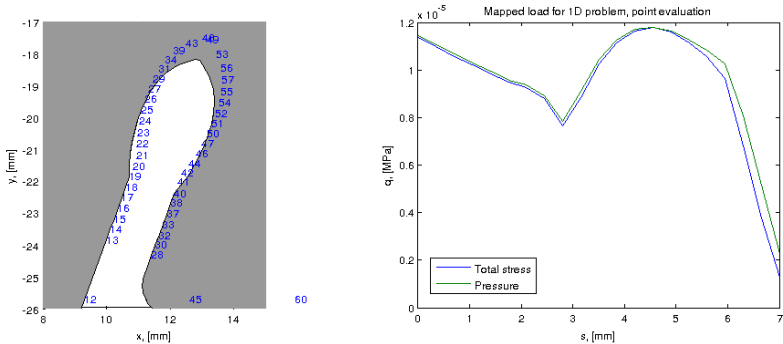


Figure 3.11: The shape of second test epiglottic fold (left) and the mapped load from the pressure and the total stress (right).

Thus, Figs. 3.10 and 3.11 suggest that the usage of the pressure alone is sufficient. Therefore in all future simulations only the pressure mapping is considered. To solve the epiglottic fold shape problem, boundary conditions must be included. In this work the end of the epiglottic fold is considered free (no shear force, no torque) and the beginning of epiglottic fold is set at a fixed angle.

After the mapping for the 1D elasticity problem is created and the three boundary conditions have been identified, one can choose a numerical method to solve the derived Euler–Bernoulli beam type equation (3.10). In the current work, a finite difference method (FDM) is used. The solution of equation (3.10) gives new angle distribution  $\varphi(s)$ , that can be used to construct a new epiglottic fold shape. All the steps described in the current section are repeated until a balance of fluid and elasticity forces is reached.

## 4 Results and analysis

The quantities to observe for Model 0 and 1 were determined after discussions with our collaborators in Uppsala. A schematic representation of the chosen quantities is given in Fig. 4.1.

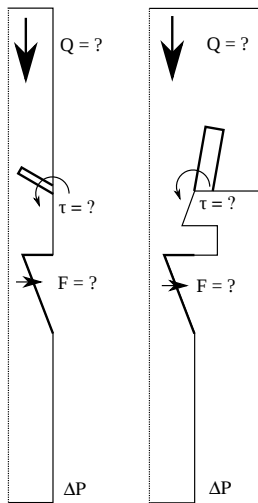


Figure 4.1: A schematic representation of selected quantities to be measured, Model 0 (left) and Model 1 (right).

The meaning of the selected measurements is essentially as follows. For the given reference pressure difference  $\Delta P_{\text{ref}}$  (representing a lung suction power), the following measurements are taken (for an approximate location see Fig. 4.1):

1.  $Q$  — the obtained air flow through the larynx, which corresponds to the breathing capability. The flow is integrated over the inlet surface. A very small flow essentially means choking;
2.  $\tau$  — the torque that is exerted on the epiglottic fold by air, can be related to a risk to acquire a supra-glottic EILO. The torque is calculated using an approximated expression. The lever arm is taken as the distance from the rotation point to the point on surface.
3.  $F$  — the horizontal force that is exerted on the vocal cords by air, which corresponds to a risk to acquire a glottic EILO. The force is integrated over the vocal chord surface.

For Model 1 with elasticity, the quasi-stationary iteration dynamics are investigated for various Young modulus values. Converged epiglottic fold shapes are also investigated.

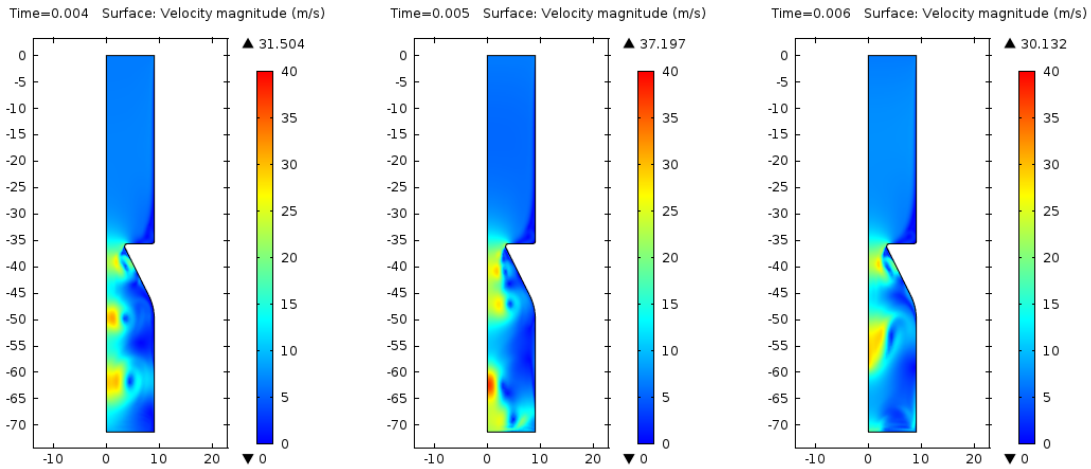


Figure 4.2: The velocity magnitude at times  $t = 4$  ms (left),  $t = 5$  ms (middle) and  $t = 6$  ms (right). The unsteady simulation with laminar outflow boundary condition, compressible Navier-Stokes equations.

## 4.1 Turbulence time scale study

During the initial calculation series, an unsteady DNS was carried out using Model 0 geometry. Compressible Navier-Stokes equations were used. Due to complexity of the task, the simulation is probably under-resolved. Also, the described boundary conditions (see Section 2.3) were not sufficient to obtain any reasonable results. The “laminar outflow” condition (see COMSOL 4.2 CFD users guide pages 137–139) for the outlet was selected. A uniform velocity initial condition for the domain and the inlet were set. The results for the velocity magnitudes at selected time moments are shown in Fig. 4.2. A surface point is selected just below the vocal cords. Fig. 4.3 presents the pressure at the selected point as function of time. The largest oscillations have a time scale

$$t_{\text{turb}} \approx 1.0 - 2.0 \text{ ms.} \quad (4.1)$$

In Section 1.3.2 the turbulence time scale was estimated to  $t_{\text{turb}} \approx 0.5$  ms by simple dimensional reasoning. An agreement within order of magnitude is obtained. In both estimations the time scale is very small. Therefore an averaging of turbulence effects and the RANS turbulence modelling with the  $k - \omega$  model seems to be a reasonable choice.

All following simulations use incompressible Navier–Stokes equations with the zero normal stress boundary condition at the outlet. No convergence problems with such selection have been noticed in steady simulations with the turbulence modelling.

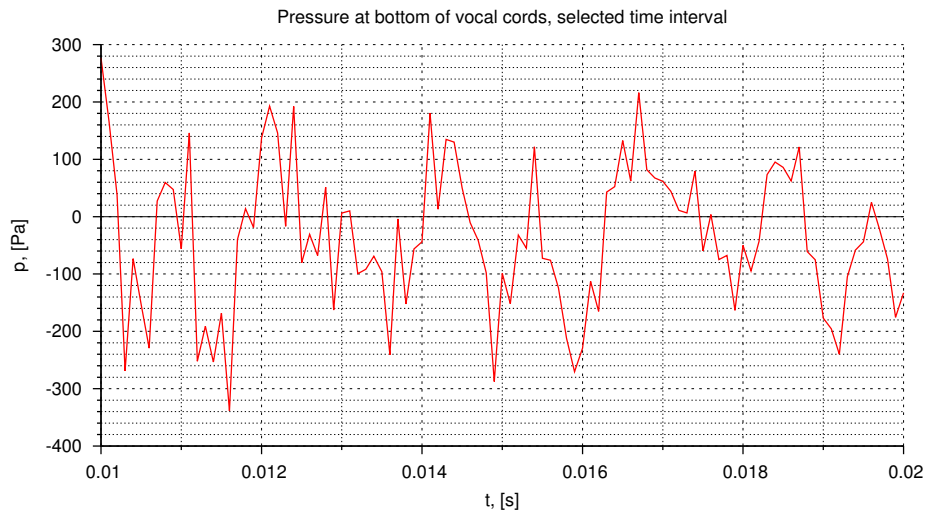


Figure 4.3: The pressure for the surface point just below the vocal cords, the selected time interval.

## 4.2 Solution convergence study

### 4.2.1 Domain size study

In order to determine appropriate simulation settings, convergence of the simulations with respect to various settings is checked. First, a domain size investigation is carried out with the default mesh settings. The reason of such investigation is to find out how much the outlet boundary condition influences the results.

The original size of the domain (denoted with  $L_0$ ) is taken as a reference. In addition, five in the downstream direction extended simulation domains were used (with lengths  $1.2 \cdot L_0$ ,  $1.4 \cdot L_0$ ,  $1.6 \cdot L_0$ ,  $1.8 \cdot L_0$  and  $2.0 \cdot L_0$ ). The pressure is investigated over all the non-slip surface with respect to the position on the surface, where position zero represents the inlet. The pressure is chosen to be monitored, since it is assumed to be the most interesting quantity to observe. The results for all cases are shown in Fig. 4.4. The zero normal stress boundary condition essentially fixes the pressure at the outlet. Since the pressure drop is the meaningful quantity, it is decided to shift the pressure results to get the zero pressure at the inlet. Shifted results are shown in Fig. 4.5.

The shifted pressure curves essentially coincide in the upper part of the simulation domain. At the end of each domain, there are small anomalies. Nevertheless it can be concluded that the effect of the outlet boundary condition on the obtained pressure distribution is small. Henceforth the original length of the simulation domain is used for all simulations.

As a second test, the averaged pressure over horizontal cross-sections of the domain was also checked. No qualitative differences in comparison to the surface pressure curve were obtained.

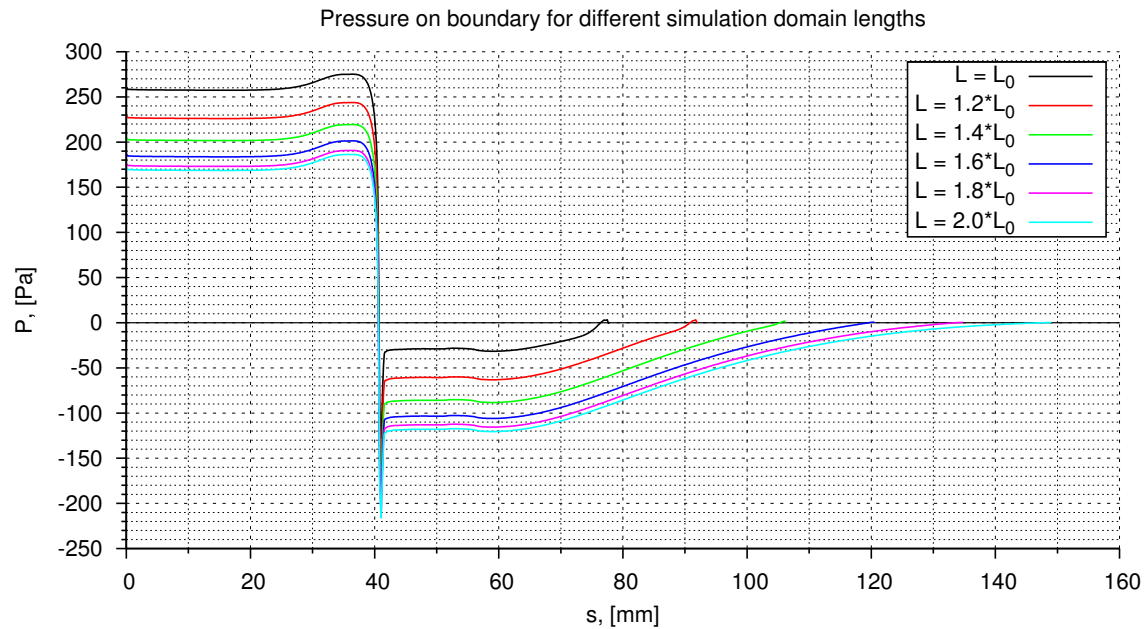


Figure 4.4: The pressure at the non-slip surface for various simulation domain lengths.

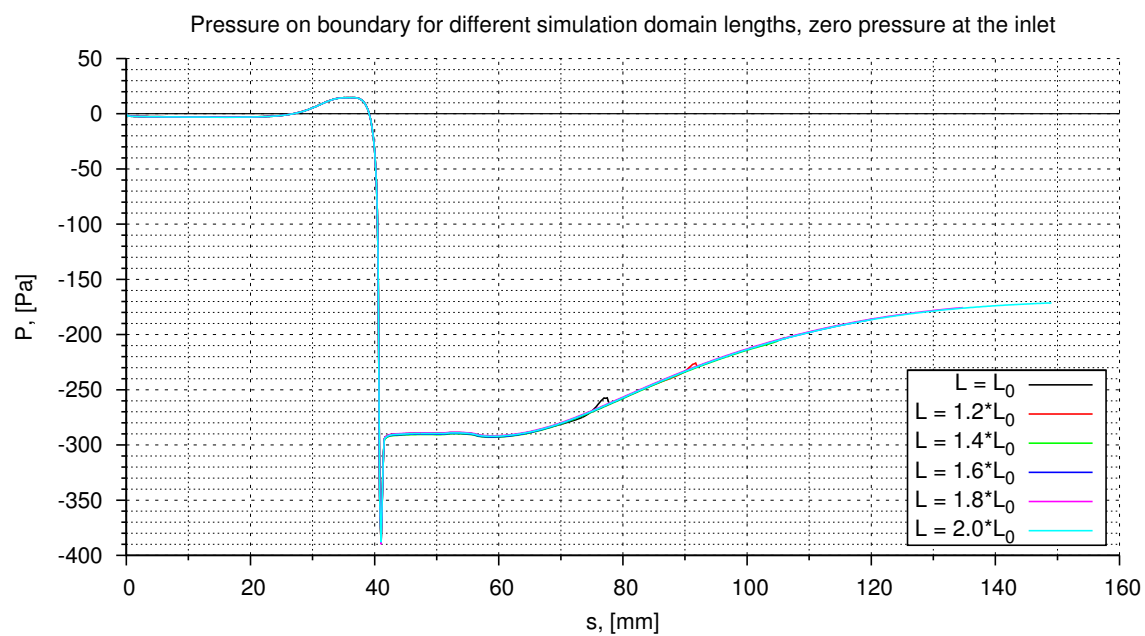


Figure 4.5: The pressure at the non-slip surface for various simulation domain lengths with the zero pressure at the inlet.

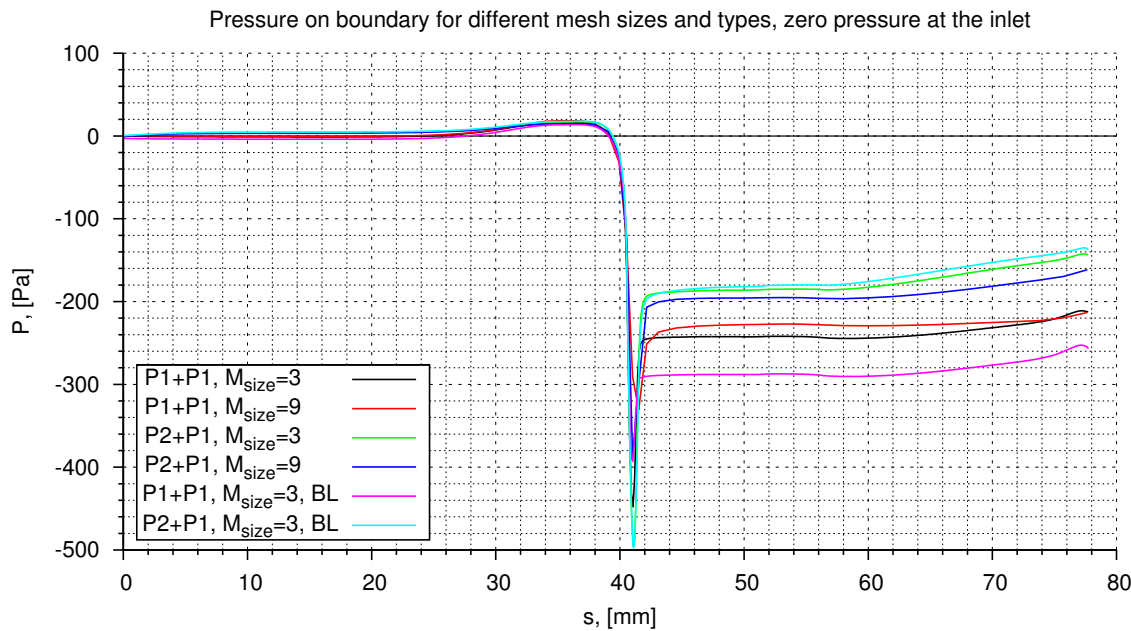


Figure 4.6: The pressure at the non-slip surface for various mesh types and sizes, two different discretizations.

#### 4.2.2 Mesh type and size study

To test the mesh settings, various studies with different mesh types and different mesh levels are carried out. To evaluate the results, the pressure on the wall is monitored. It is found that the results are quite sensitive to the choice of mesh type and size, and also to the choice of discretization scheme. In order to summarize the observed behaviour, shifted pressure results (to have the zero pressure at the inlet) for the finest and the coarsest meshes and both discretizations and mesh types are given in Fig. 4.6. The  $M_{\text{size}}$  parameter (Fig. 4.6) indicates the mesh level (see Tab. 2.1), while the tag *BL* indicates the mesh with the boundary layer elements. The results within the same discretization and mesh type seem to differ only little, while between different discretizations and different mesh types the jump is rather notable.

In order to further understand the differences, the mesh sizes where the biggest difference occurs are selected. The *BL* case meshes are shown in Fig. 4.7. The velocity streamlines for the *BL* meshes are investigated in the same region (Fig. 4.8). The results of the  $P1 + P1$  case with the finest mesh are very similar to the results of the  $P2 + P1$  case with the crudest mesh. Such an agreement can also be observed in the pressure plots (not shown in order to limit the amount of figures).

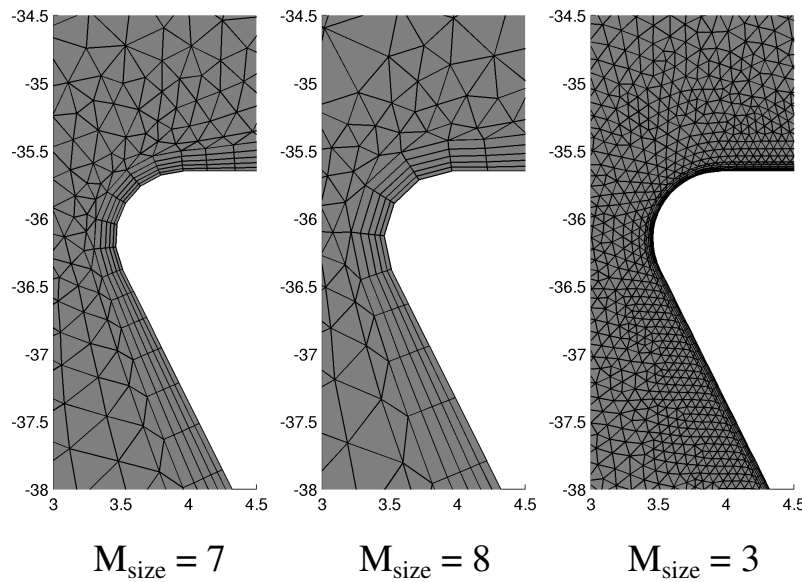


Figure 4.7: The boundary layer mesh around the vocal cords, different mesh sizes.

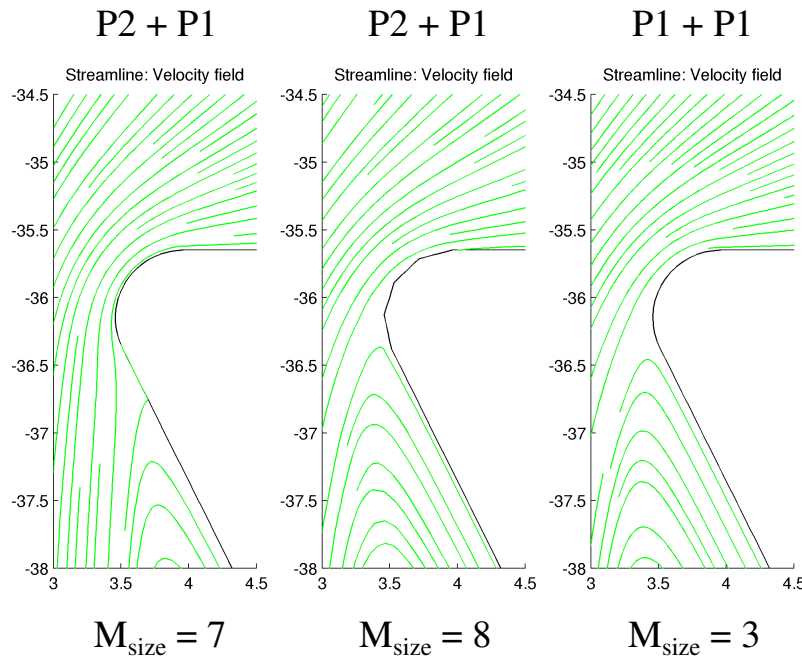


Figure 4.8: The velocity streamlines around the vocal cords for different mesh sizes and discretizations, when using the boundary layer mesh.

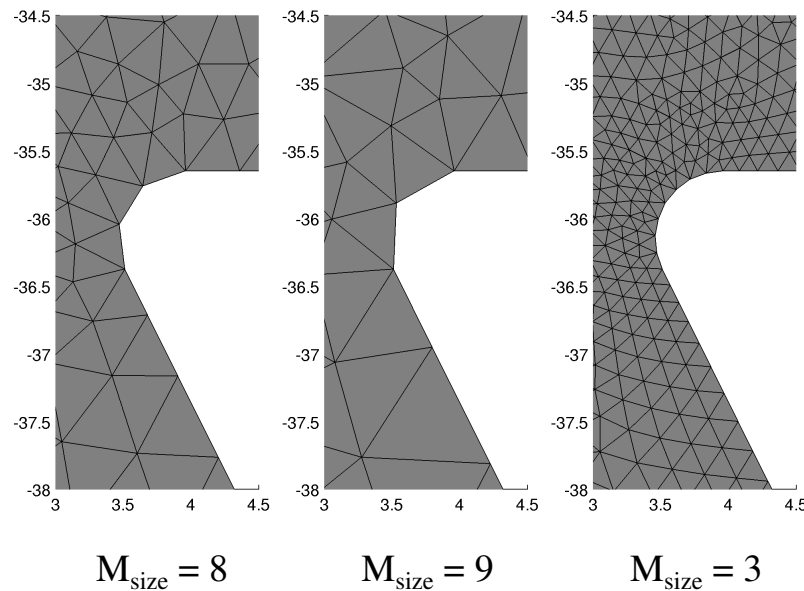


Figure 4.9: The triangular mesh around the vocal cords for different mesh sizes.

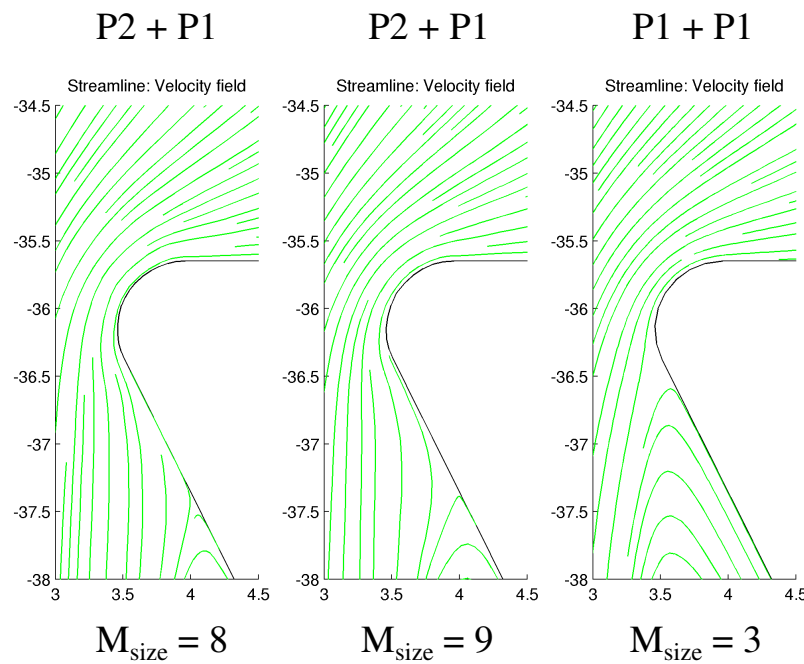


Figure 4.10: The velocity streamlines around the vocal cords for different mesh sizes and discretizations, when using the purely triangular mesh.

Mesh and streamline plots for the same region are given for the purely triangular mesh in Fig. 4.9 and Fig. 4.10, respectively. By comparing the streamline plots closely (see Fig. 4.8 and Fig. 4.10), one can see that the flow separation point has different positions. It seems that the flow separation point is further downstream for the more accurate discretizations and also for the finer meshes. The change of the flow separation point is determined to be the reason for the difference in pressure drops on the surface. Henceforth the purely triangular mesh of the mesh size  $M_{\text{size}} = 5$  with the  $P2 + P1$  discretization is used for all simulations.

## 4.3 Model 0 results

### 4.3.1 Reference simulation

In order to commence case studies, a reference simulation without the epiglottic fold is carried out. The pressure drop for the flow  $Q = 100 \text{ l/min}$  is determined to be

$$\Delta P_{\text{ref}}^{\text{M}0} = 145.34 \text{ Pa} \quad (4.2)$$

for this case.

### 4.3.2 Epiglottic fold distance study

As a first case study, a varying epiglottic fold distance  $f_{\text{dist}}$  is selected. The epiglottic fold is set at a closed position ( $f_{\text{angle}} = 90^\circ$ ), and the length is selected to be the estimated epiglottic length ( $f_{\text{length}} = 7.0 \text{ mm}$ ). The fold distance interval  $f_{\text{dist}} \in [3; 13] \text{ mm}$  is selected symmetrically around the initial distance 8 mm. The velocity magnitudes for the three distances  $f_{\text{dist}} = 3, 8, 13 \text{ mm}$  are given in Fig. 4.11. The resulting flow through the larynx model for the pressure drop  $\Delta P_{\text{ref}}^{\text{M}0}$  is given in Fig. 4.12, the obtained torque on the epiglottic fold is given in Fig. 4.13, and the horizontal force on the vocal cords is given in Fig. 4.14. The variation in the horizontal force on the vocal cords (see Fig. 4.14) is negligible. It seems to indicate no correlation between the fluid forces and the glottic EILO.

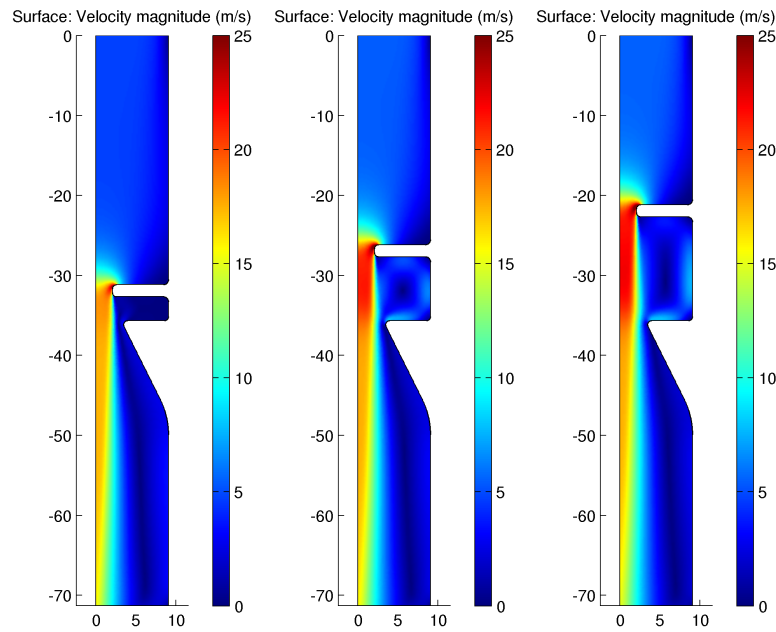


Figure 4.11: The velocity magnitudes for the epiglottic fold distances  $f_{\text{dist}} = 3, 8, 13$  mm, Model 0.

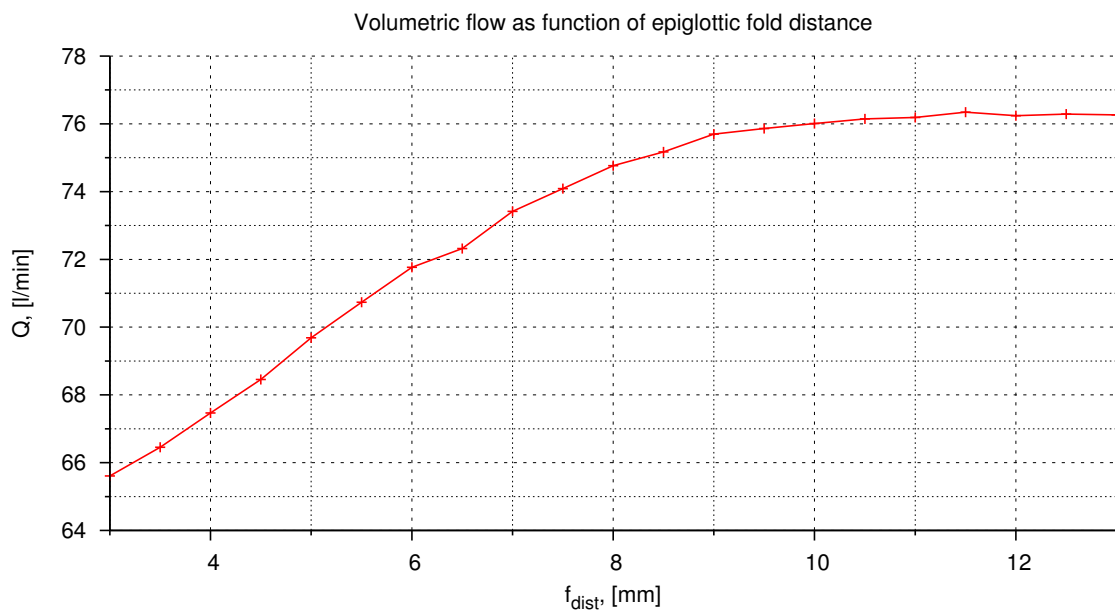


Figure 4.12: The epiglottic fold distance case study, the flow results, Model 0.

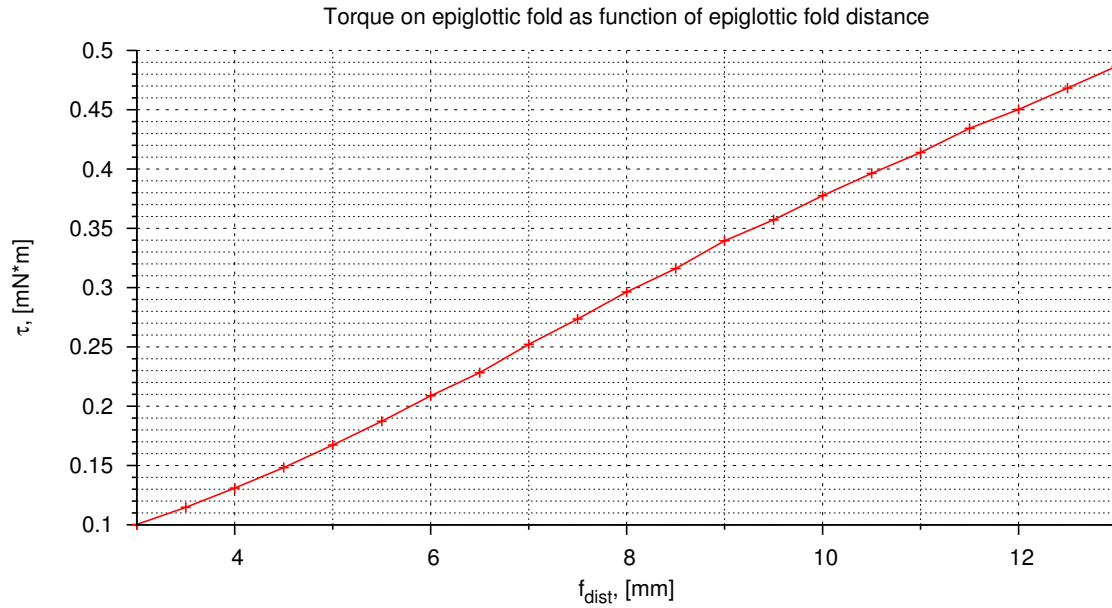


Figure 4.13: The epiglottic fold distance case study, the torque on the epiglottic fold, Model 0.

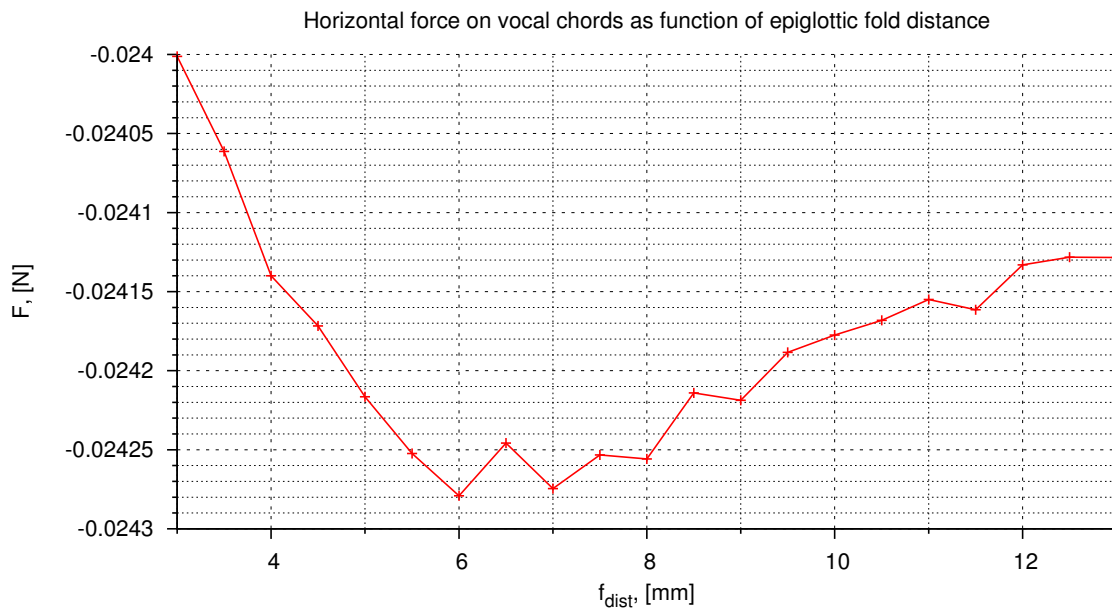


Figure 4.14: The epiglottic fold distance case study, the horizontal force on the vocal cords, Model 0.

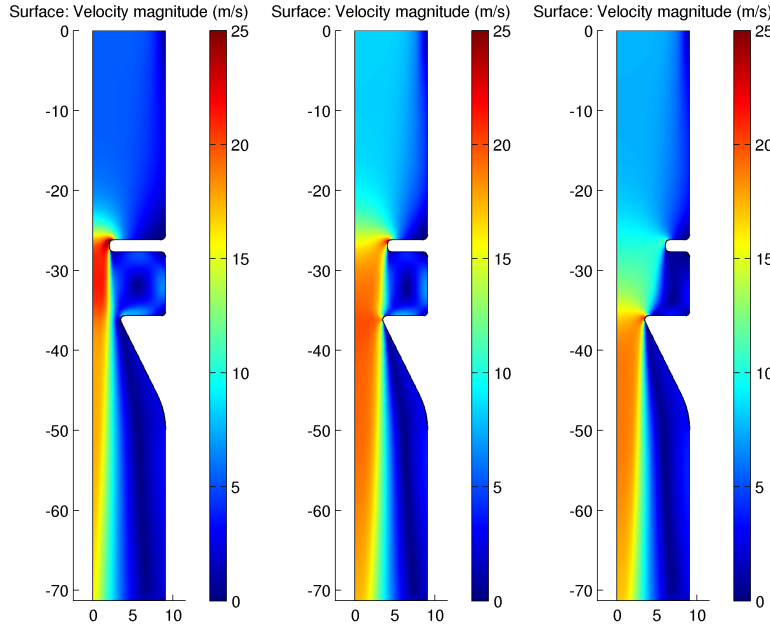


Figure 4.15: The velocity magnitudes for the epiglottic fold lengths  $f_{\text{length}} = 3, 5, 7$  mm, Model 0.

### 4.3.3 Epiglottic fold length study

For the next case study, a varying epiglottic fold length  $f_{\text{length}}$  is selected. The epiglottic fold is selected to be at a closed position ( $f_{\text{angle}} = 90^\circ$ ) at the distance  $f_{\text{dist}} = 8.0$  mm. The length interval  $f_{\text{length}} \in [3; 7]$  mm is selected to represent both a wider and a narrower gap than the vocal cord gap. The velocity magnitudes for the three lengths  $f_{\text{length}} = 3, 5, 7$  mm are given in Fig. 4.15. The resulting flow through the larynx for the pressure drop  $\Delta P_{\text{ref}}^{\text{M}0}$  is given in Fig. 4.16, the obtained torque on the epiglottic fold is given in Fig. 4.17, and the horizontal force on the vocal cords is given in Fig. 4.18. There is a counter intuitive increase in the resulting flow for epiglottic fold lengths  $3.0 \leq f_{\text{length}} \leq 6.0$  mm. The torque results for the smallest epiglottic fold lengths should be viewed with suspicion, due to the approximate nature of the torque calculation. The variation in the horizontal force on the vocal cords (see Fig. 4.18) is very small also in this case.

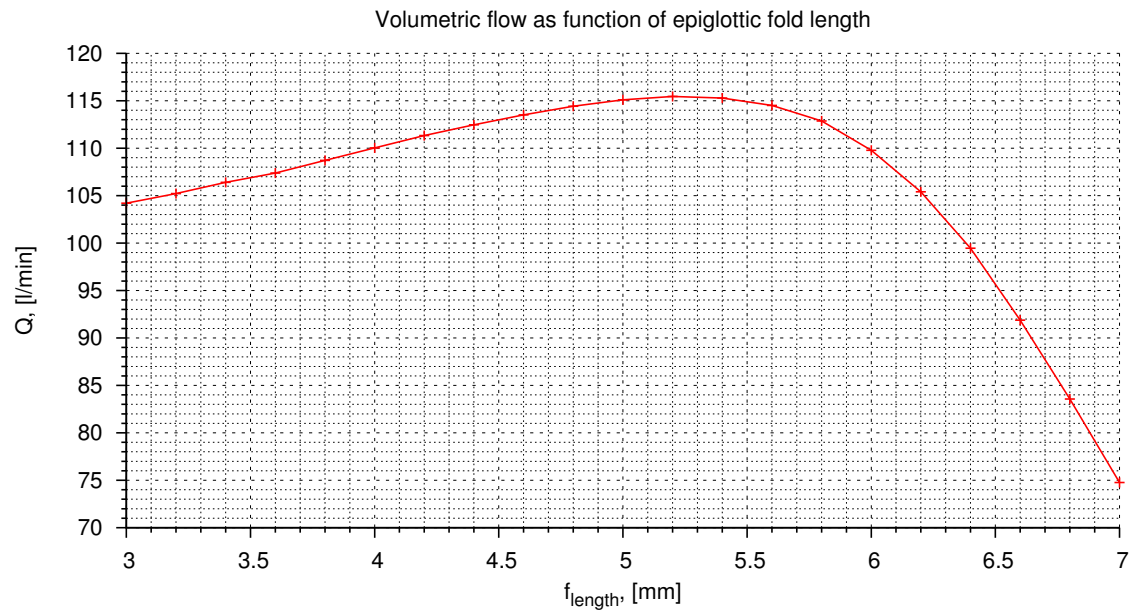


Figure 4.16: The epiglottic fold length case study, the flow results, Model 0.

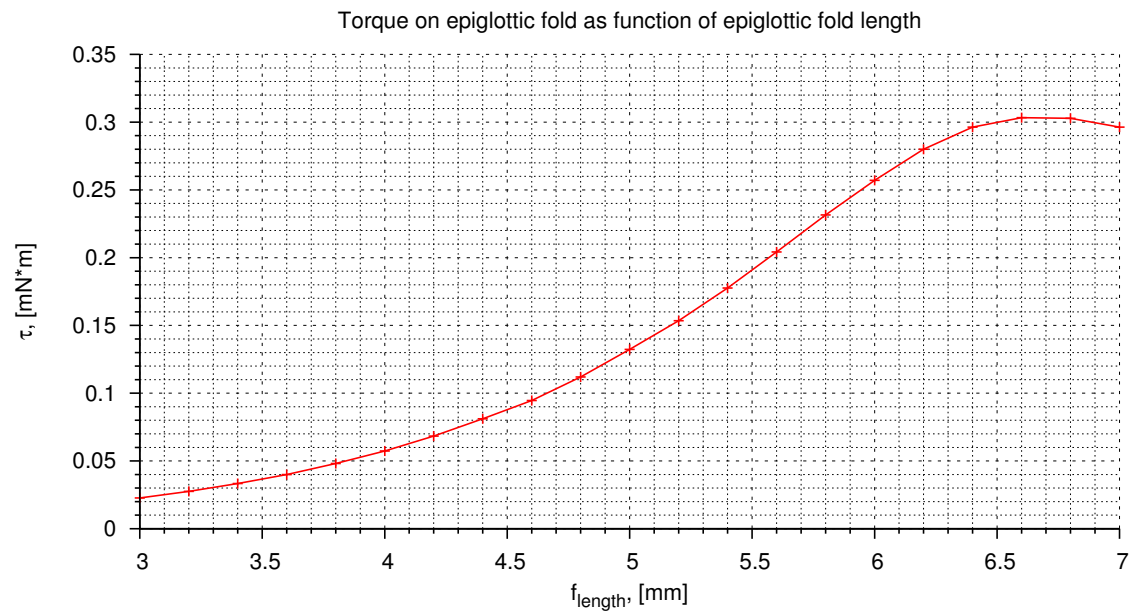


Figure 4.17: The epiglottic fold length case study, the torque on epiglottic fold, Model 0.

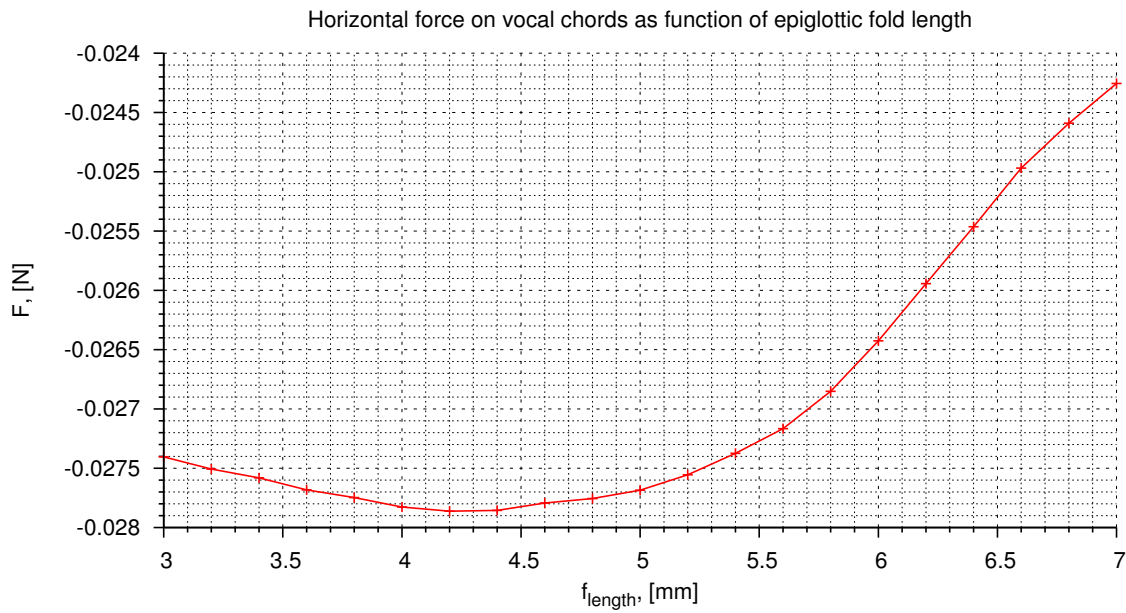


Figure 4.18: The epiglottic fold length case study, the horizontal force on the vocal cords, Model 0.

#### 4.3.4 Epiglottic fold angle study

As the last case study, a varying epiglottic fold angle  $f_{\text{angle}}$  is selected. The epiglottic fold length is selected to have the estimated value ( $f_{\text{length}} = 7.0$  mm) and set at distance  $f_{\text{dist}} = 8.0$  mm, and the angle interval  $f_{\text{angle}} \in [20^\circ; 90^\circ]$  is selected to avoid problems with the geometry generation. The velocity magnitudes for the three angles  $f_{\text{angle}} = 20^\circ, 55^\circ, 90^\circ$  are given in Fig. 4.19. The resulting flow trough the larynx for the pressure drop  $\Delta P_{\text{ref}}^{\text{M}0}$  is given in Fig. 4.20, the obtained torque on the epiglottic fold is given in Fig. 4.21, and the horizontal force on the vocal cords is given in Fig. 4.22. Also in this study there is a counter intuitive increase in the resulting flow for epiglottic fold angles  $30^\circ \leq f_{\text{angle}} \leq 60^\circ$ . The torque data for the smallest epiglottic fold angles should be viewed with suspicion also in this case. The variation in horizontal force on the vocal cords (see Fig. 4.22) is negligible again.

Due to no apparent importance, in all following simulations both the vertical force on the vocal cords and the torque on the epiglottic fold is not monitored.

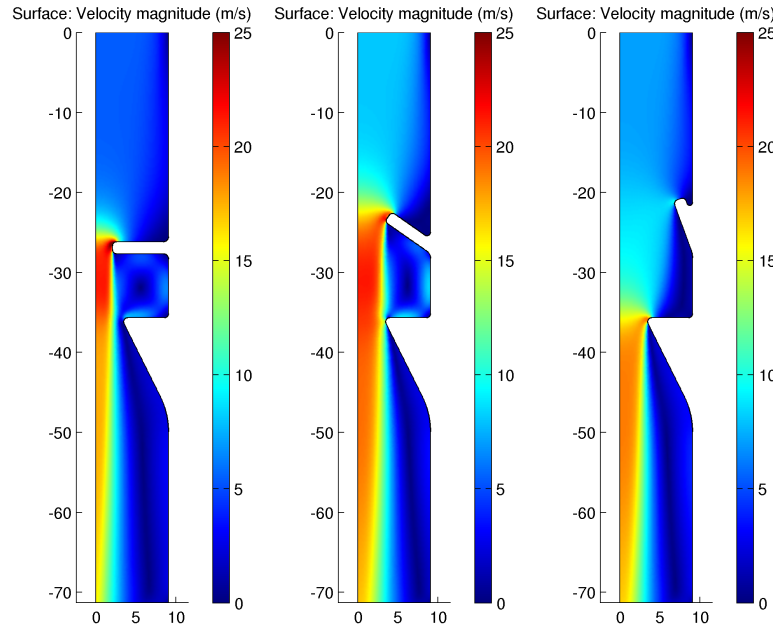


Figure 4.19: The velocity magnitudes for the epiglottic fold angles  $f_{\text{angle}} = 20^\circ, 55^\circ, 90^\circ$ , Model 0.

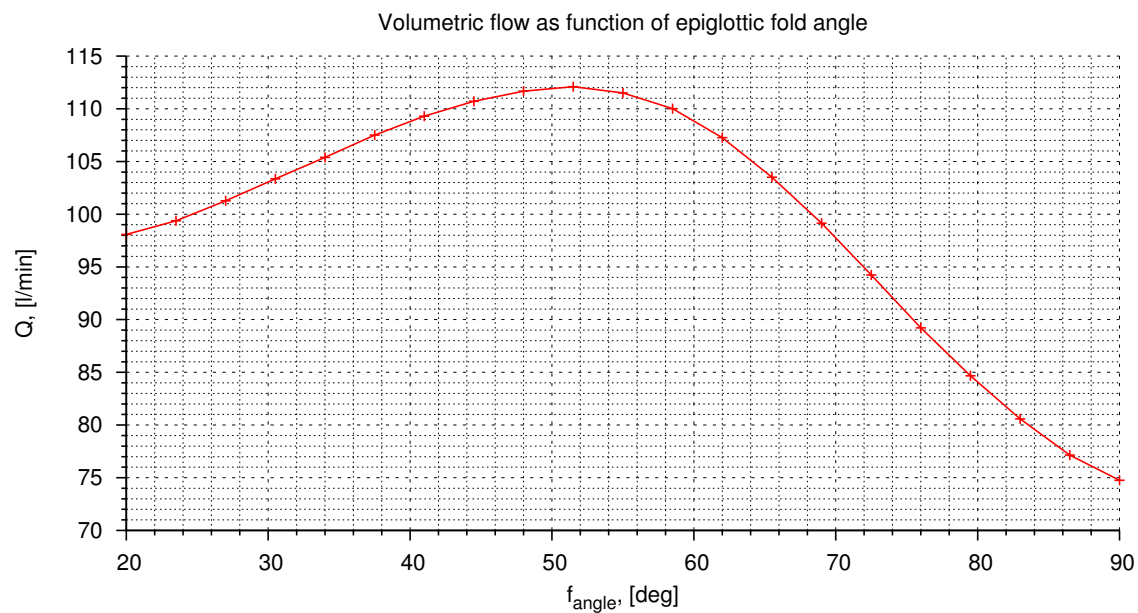


Figure 4.20: The epiglottic fold angle case study, the flow results, Model 0.

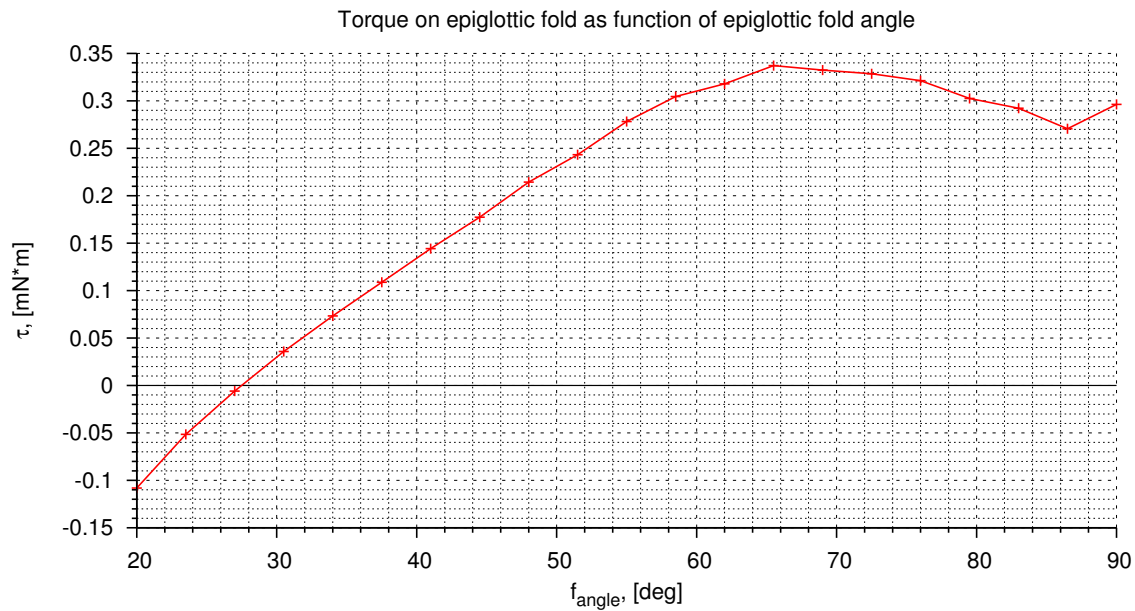


Figure 4.21: The epiglottic fold angle case study, the torque on the epiglottic fold, Model 0.

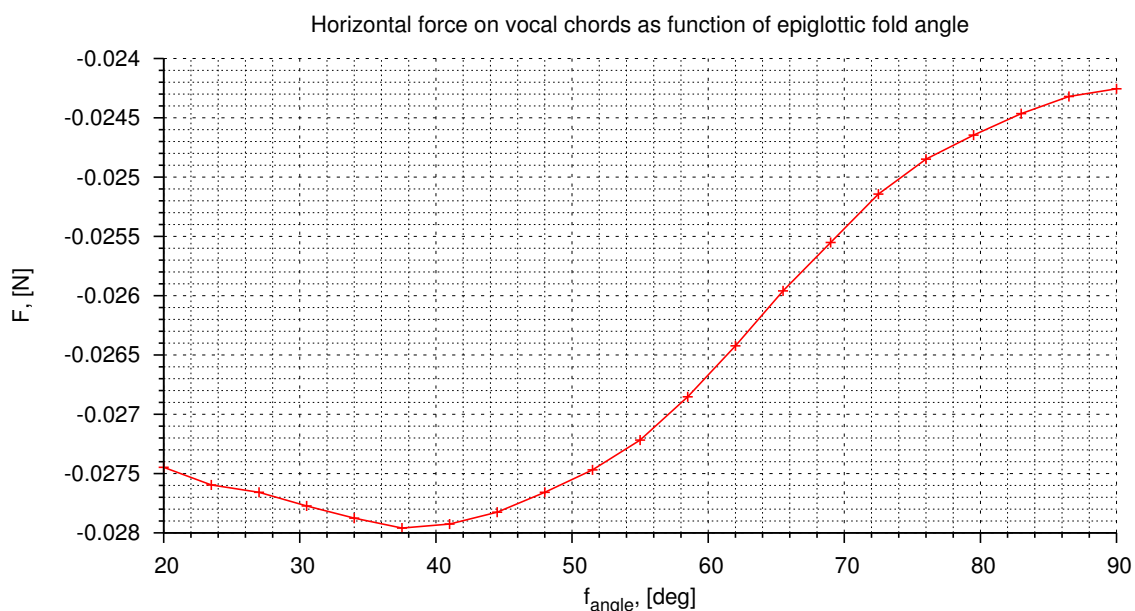


Figure 4.22: The epiglottic fold angle case study, the horizontal force on the vocal cords, Model 0.

## 4.4 Model 1 results

### 4.4.1 Reference simulation

In order to commence the next case studies, a reference simulation with the epiglottic fold in an upright position is carried out. For this case the pressure drop for the flow  $Q = 100$  l/min is determined to be

$$\Delta P_{\text{ref}}^{\text{M1}} = 148.73 \text{ Pa.} \quad (4.3)$$

In this case, the reference pressure drop is the same for the epiglottic fold angle and length studies, as well as for the vocal cord opening study. However, for the false vocal cord distance study, the reference pressure drop is recalculated for each case. The motivation is that the false vocal cord distance should be the same for an individual, but may vary across individuals. The epiglottic fold angle and the vocal cord opening can change for the individual itself.

### 4.4.2 Laryngeal ventricle existence study

In the evolution from Model 0 to Model 1, quite some characteristics of the simulation domain were changed. In the current section, Model 1 with and without the laryngeal ventricle (see Fig. 1.1) is considered. The representation of the obtained velocity magnitude is given in Fig. 4.23. The resulting flow as a function of the epiglottic fold angle is investigated (Fig. 4.24). When the laryngeal ventricle is added, there is a noticeable but very small change in resulting flow rate. The change is well below the margins of the turbulence modelling accuracy, hence it is unclear whether any conclusions can be drawn. Henceforth no more small changes in the domain are investigated.

### 4.4.3 Pressure–flow characteristics study

In order to investigate the general properties of the simulation domain, a few pressure–flow characteristics curves are measured. For the measurements, the case with the epiglottic fold in the opened state ( $f_{\text{angle}} = -16^\circ$ ) and the case with the epiglottic fold in the closed state ( $f_{\text{angle}} = 89^\circ$ ) are selected. The velocity magnitudes for the flow rate  $Q = 40$  l/min are given in Fig. 4.25. The corresponding pressure–flow curves are given in Fig. 4.26. The pressure relation to flow rate seems to be approximately quadratic, a relation that also holds for turbulent flow in a pipe [15]. If relation follows the exponent function, in a log-log graph it can be fitted with a linear function. The obtained linear fits for the epiglottic fold in the opened and the closed states are given in Fig. 4.27 and Fig. 4.28, respectively.

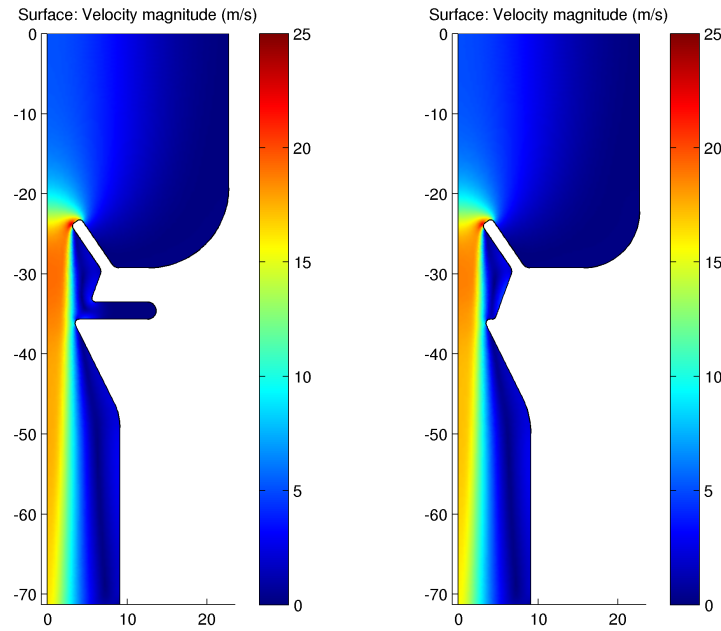


Figure 4.23: Model 1 with (left) and without (right) the laryngeal ventricle, the velocity magnitude.

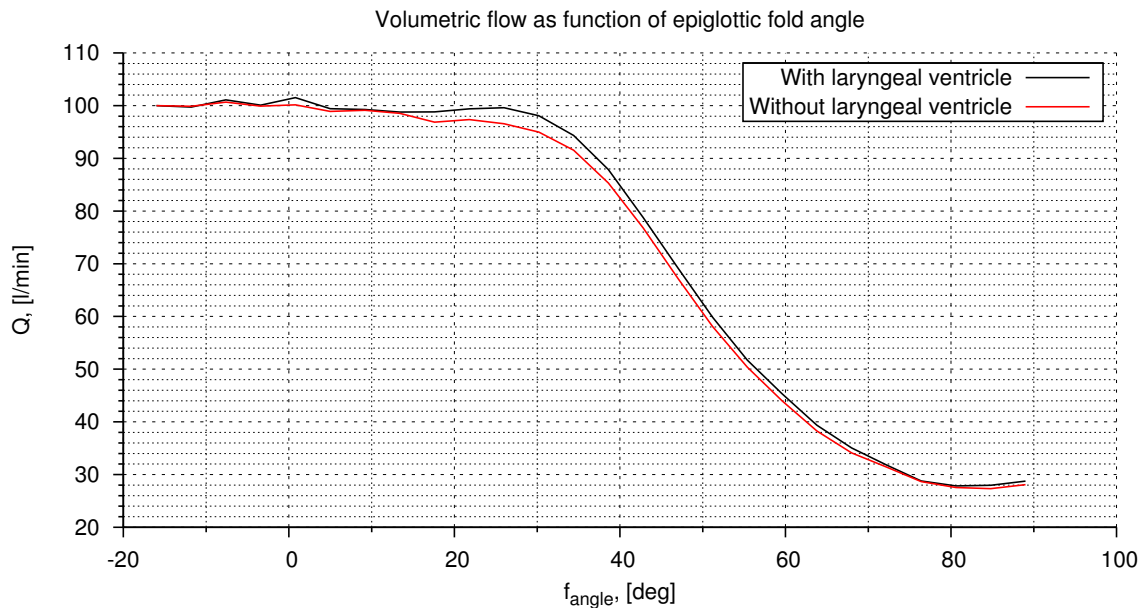


Figure 4.24: The resulting flow as a function of the epiglottic fold angle with and without the laryngeal ventricle, Model 1.

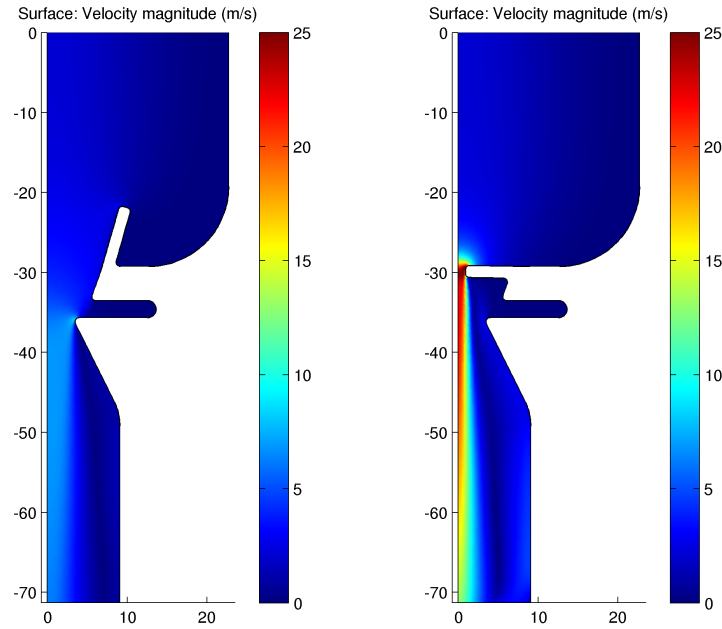


Figure 4.25: An example of the velocity field for the flow  $Q = 40 \text{ l/min}$  with the epiglottic fold in the opened (left) and the closed (right) state, Model 1.

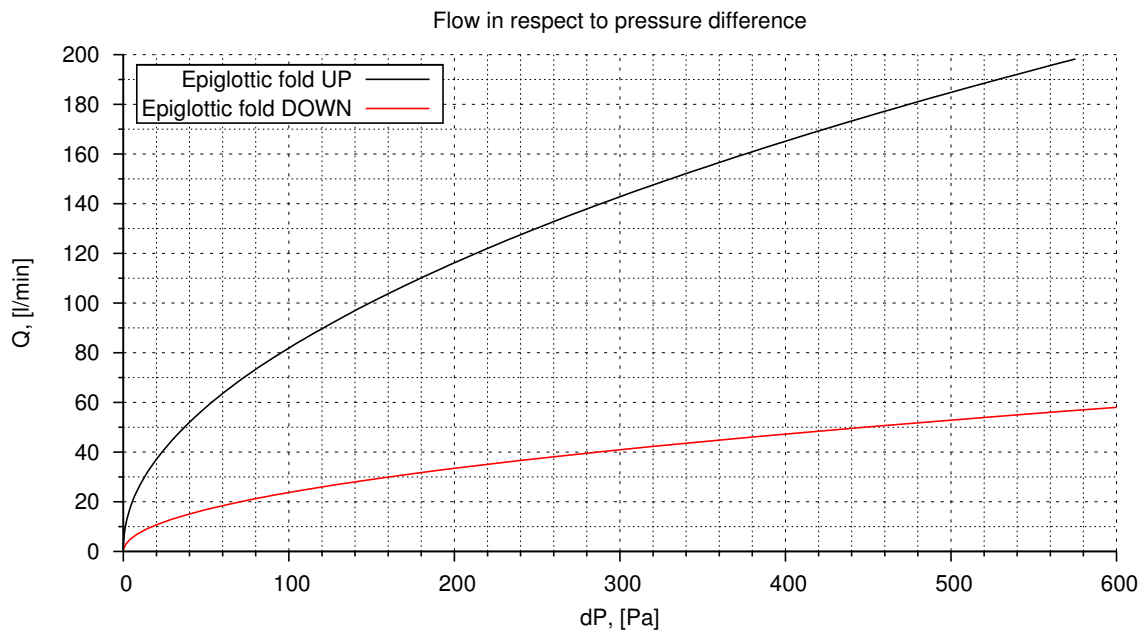


Figure 4.26: The obtained pressure–flow curves with the epiglottic fold in the opened and the closed state, Model 1.

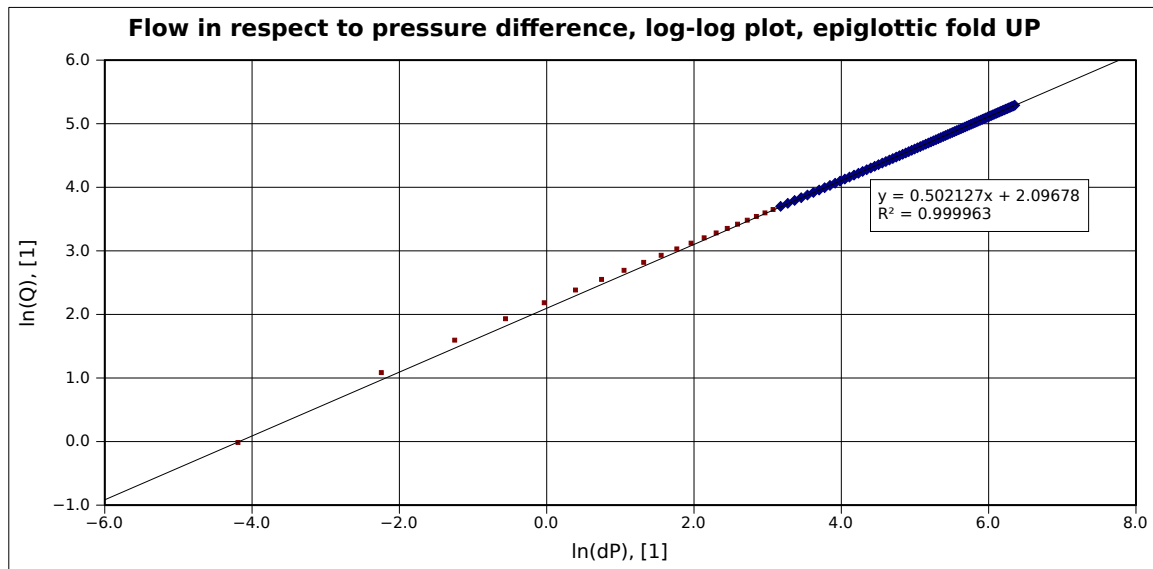


Figure 4.27: The obtained pressure–flow log-log curve with the epiglottic fold in the opened state, a linear fit in a selected interval, Model 1.

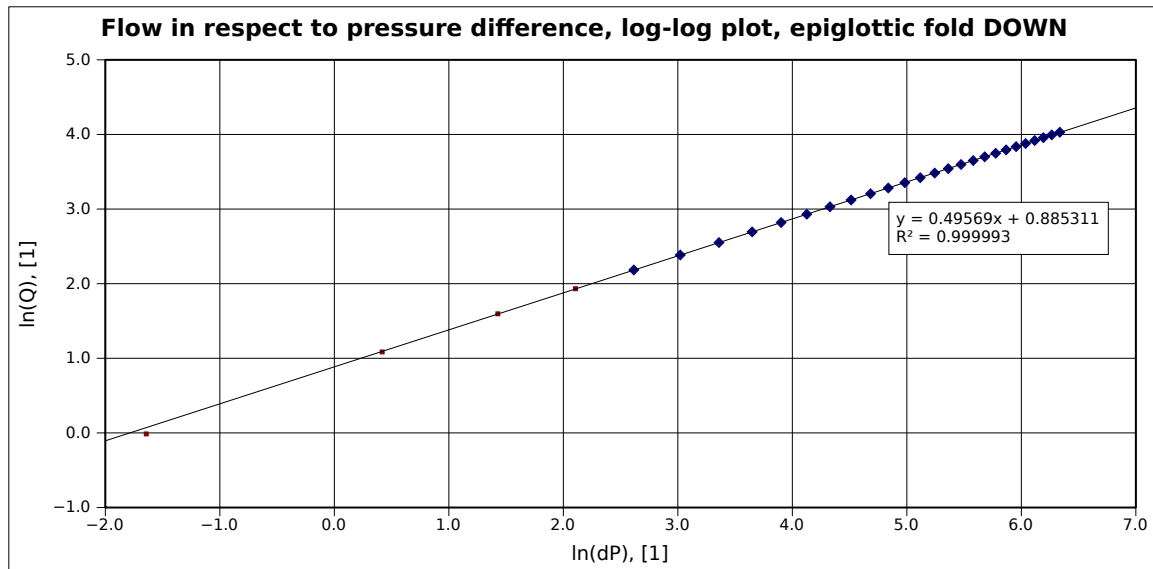


Figure 4.28: The obtained pressure–flow log-log curve with the epiglottic fold in the closed state, a linear fit in a selected interval, Model 1.

In both cases, data points denoted with blue dots has been fitted, but data points denoted with red dots has been omitted. Both the opened and the closed case show slight derivations from the linear relation for the lowest flow rates. In the fitting regions, the linear correspondence is good. The determined exponent is close to  $a \approx 0.5$ . Hence it can be concluded that the flow and the pressure characteristics in these cases obey the proportionality

$$Q \propto \Delta P^{1/2} \quad \text{or} \quad \Delta P \propto Q^2. \quad (4.4)$$

Using simple approximations for a laminar flow, the quadratic pressure correspondence to the flow rate for the high flow rate regime can be obtained analytically (see appendix B). Such result suggests the dominance of inertial forces over viscous forces, which also is in line with Reynolds number estimate (1.3).

#### 4.4.4 Epiglottic fold angle and length study

For Model 1, the epiglottic fold angle and length case studies are united in a single two-parameter study. The study is carried out with respect to both the epiglottic fold angle interval  $f_{\text{angle}} \in [-16^\circ; 89^\circ]$  and the epiglottic fold length interval  $f_{\text{length}} \in [3.5; 7.5]$  mm. The velocity magnitudes for angle values  $f_{\text{angle}} = -16^\circ, 37^\circ, 89^\circ$  and length values  $f_{\text{length}} = 7.5, 5.5, 3.5$  mm are given in Fig. 4.29, Fig. 4.30, and Fig. 4.31, respectively. The resulting flow can be conveniently represented as a contour line plot (see Fig. 4.32). There is a large region, where the breathing is unaffected (the resulting flow close to the reference flow  $Q_0 = 100$  l/min). There is also a relatively small region with a slight improvement (up to 6%) and with a large decline (up to 50%).

#### 4.4.5 Vocal cord opening study

As next case study of the Model 1, various vocal cord openings  $v_{\text{open}}$  are investigated. The velocity magnitudes for angle values  $f_{\text{angle}} = -16^\circ, 37^\circ, 89^\circ$  and vocal cord opening values  $v_{\text{open}} = 6.3, 2.3$  mm are given in Fig. 4.33 and Fig. 4.34, respectively. The resulting flow through the larynx for the pressure drop  $\Delta P_{\text{ref}}^{\text{M1}}$  with all vocal cord openings is given in Fig. 4.35.

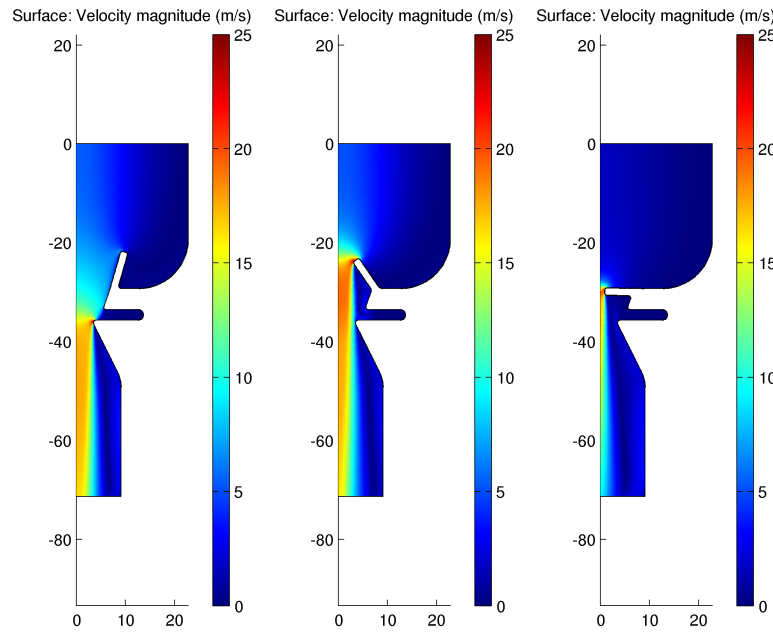


Figure 4.29: The velocity magnitudes for epiglottic fold angles  $f_{\text{angle}} = -16^\circ, 37^\circ, 89^\circ$  and epiglottic fold length  $f_{\text{length}} = 7.5 \text{ mm}$ , Model 1.

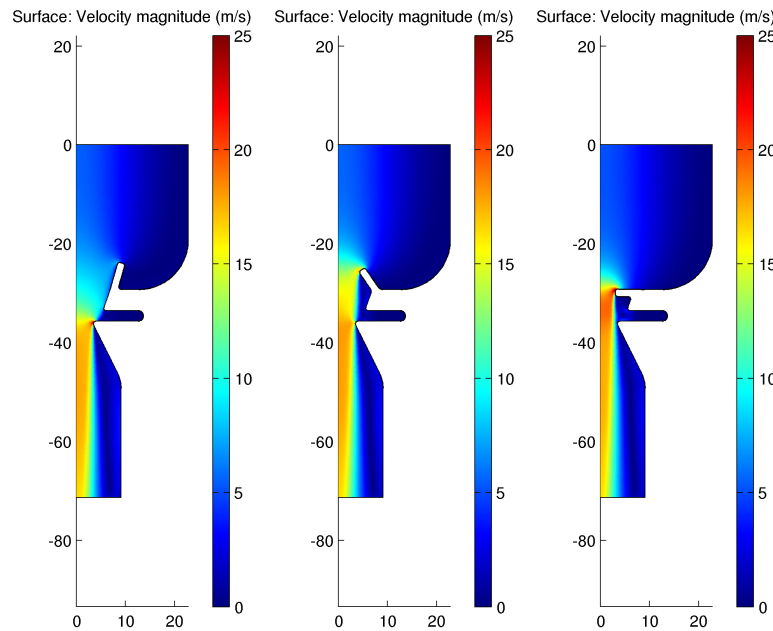


Figure 4.30: The velocity magnitudes for epiglottic fold angles  $f_{\text{angle}} = -16^\circ, 37^\circ, 89^\circ$  and epiglottic fold length  $f_{\text{length}} = 5.5 \text{ mm}$ , Model 1.

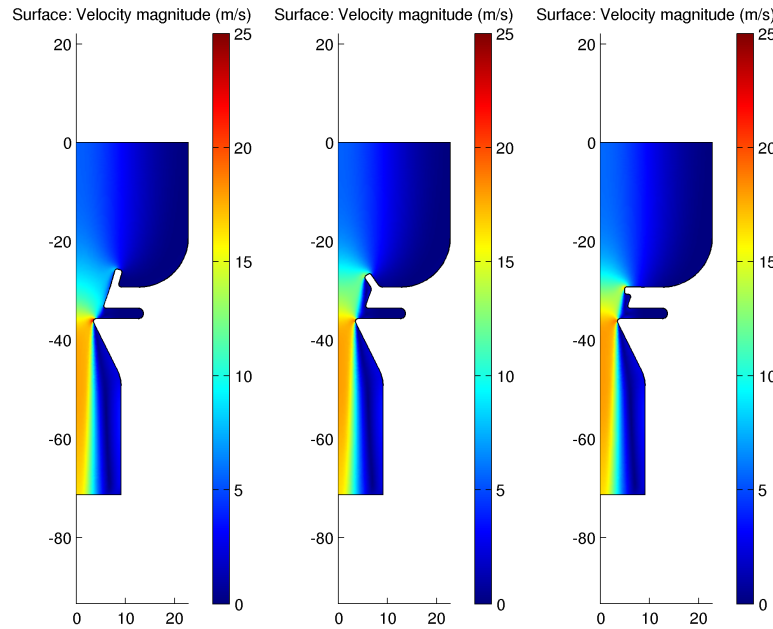


Figure 4.31: The velocity magnitudes for epiglottic fold angle values  $f_{\text{angle}} = -16^\circ, 37^\circ, 89^\circ$  and epiglottic fold length  $f_{\text{length}} = 3.5 \text{ mm}$ , Model 1.

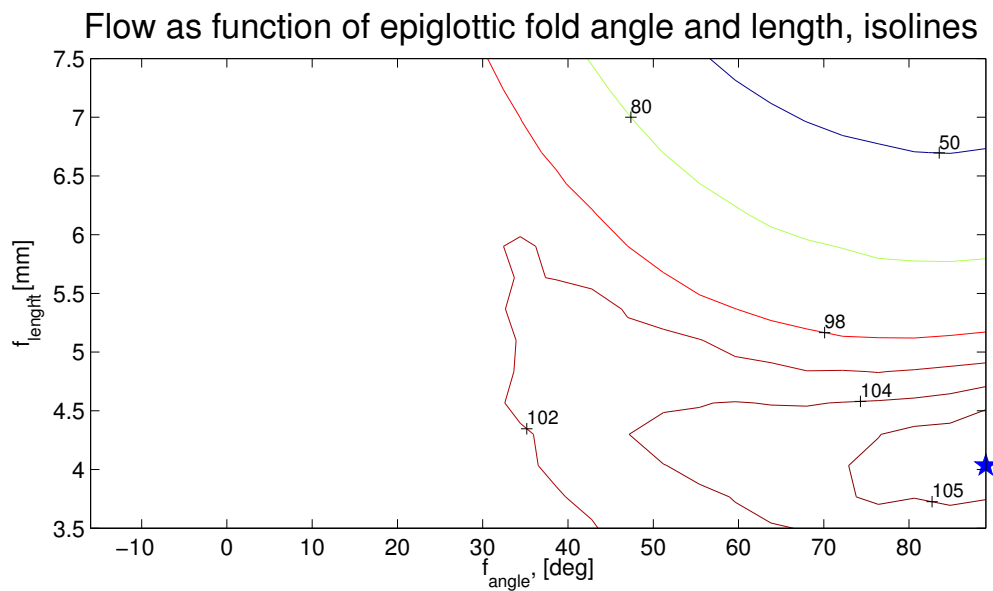


Figure 4.32: The epiglottic fold angle and length case study. The resulting flow contour lines. The maximal flow marked by a blue star, Model 1.

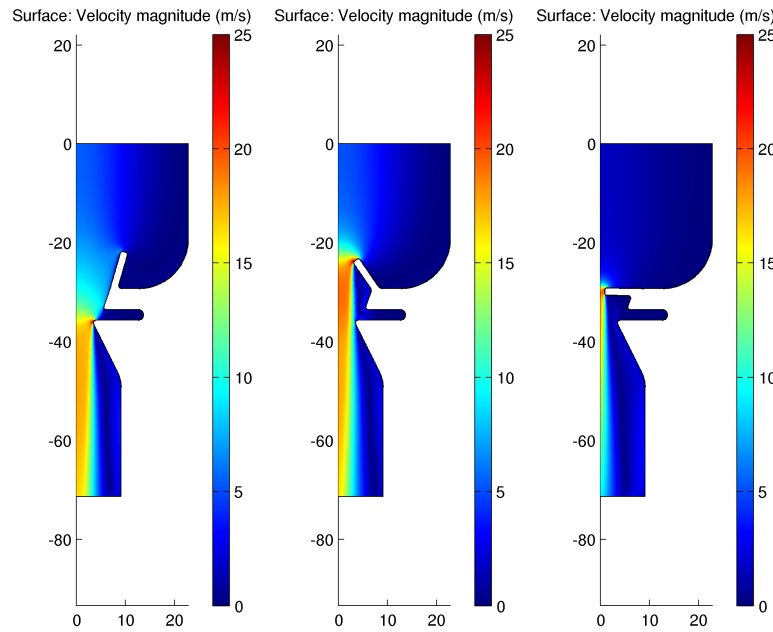


Figure 4.33: The velocity magnitudes for the epiglottic fold angle values  $f_{\text{angle}} = -16^\circ, 37^\circ, 89^\circ$  and vocal cord opening  $v_{\text{open}} = 6.3 \text{ mm}$ , Model 1.

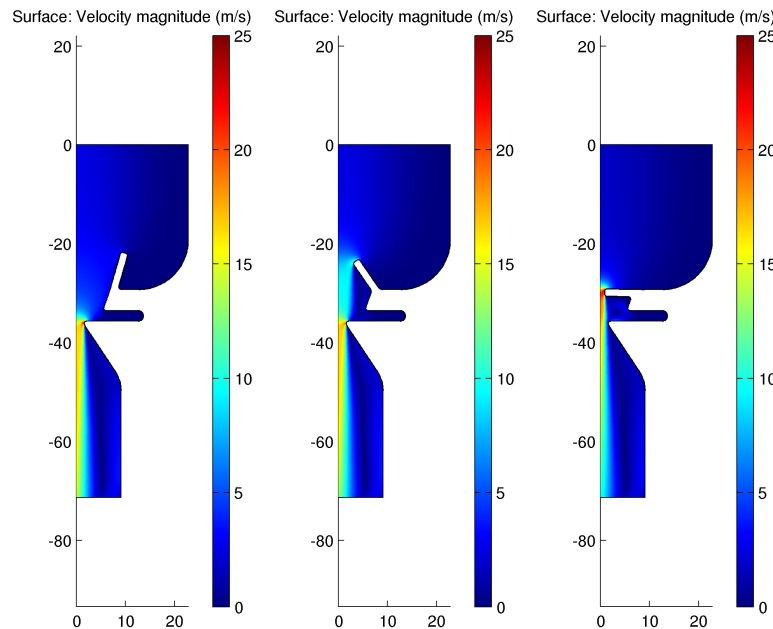


Figure 4.34: The velocity magnitudes for the epiglottic fold angle values  $f_{\text{angle}} = -16^\circ, 37^\circ, 89^\circ$  and vocal cord opening  $v_{\text{open}} = 2.3 \text{ mm}$ , Model 1.

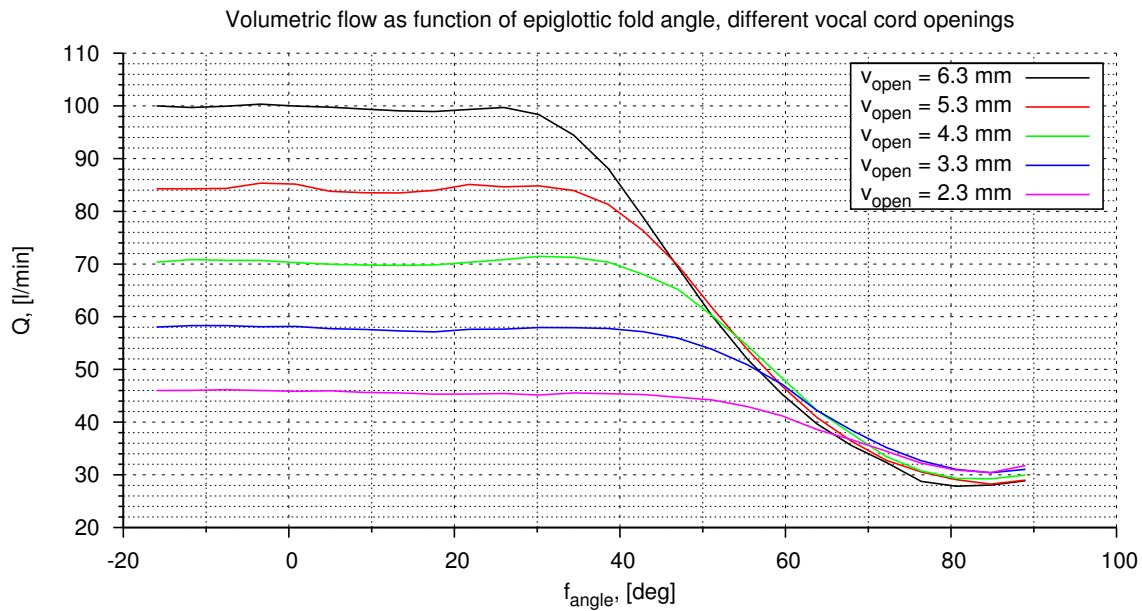


Figure 4.35: The epiglottic fold angle case study with different vocal cord openings, the resulting flow, Model 1.

#### 4.4.6 False vocal cord distance study

In the last case study for Model 1, various false vocal cord heights (effectively the epiglottic fold distance)  $fv_{\text{dist}}$  are selected. The velocity magnitudes for angle values  $f_{\text{angle}} = -16^\circ, 37^\circ, 89^\circ$  and false vocal chord height values  $fv_{\text{dist}} = 5.0, 7.8 \text{ mm}$  are given in Fig. 4.36 and Fig. 4.37, respectively. The resulting flow through the larynx for a recalculated reference pressure drop (with the epiglottic fold in the upright position) for all false vocal cord heights is given in Fig. 4.38.

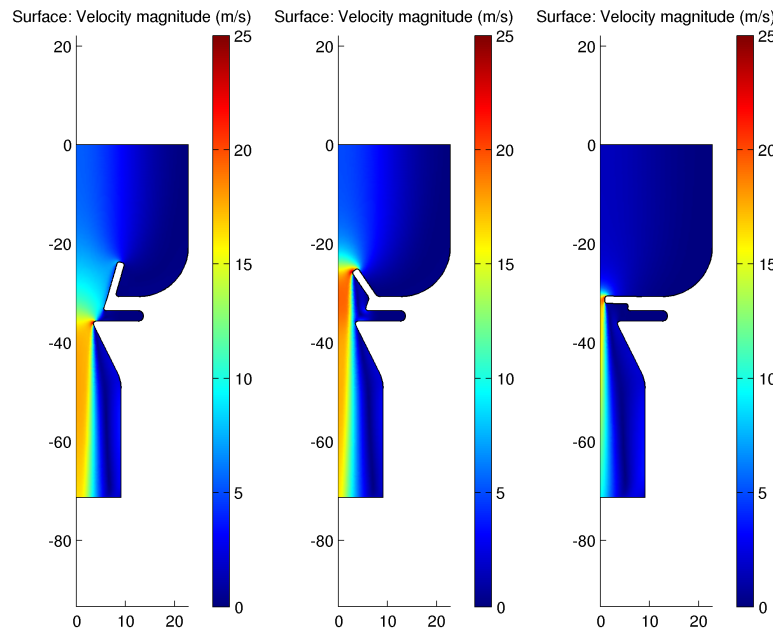


Figure 4.36: The velocity magnitudes for the epiglottic fold angle values  $f_{\text{angle}} = -16^\circ, 37^\circ, 89^\circ$  and false vocal cord height  $fv_{\text{dist}} = 5.0 \text{ mm}$ , Model 1.

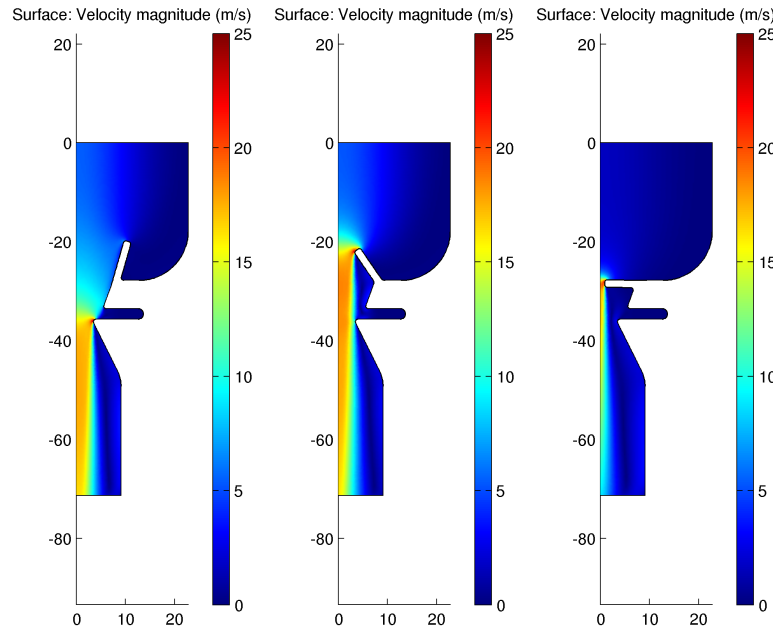


Figure 4.37: The velocity magnitudes for the epiglottic fold angle values  $f_{\text{angle}} = -16^\circ, 37^\circ, 89^\circ$  and false vocal cord height  $fv_{\text{dist}} = 7.8 \text{ mm}$ , Model 1.

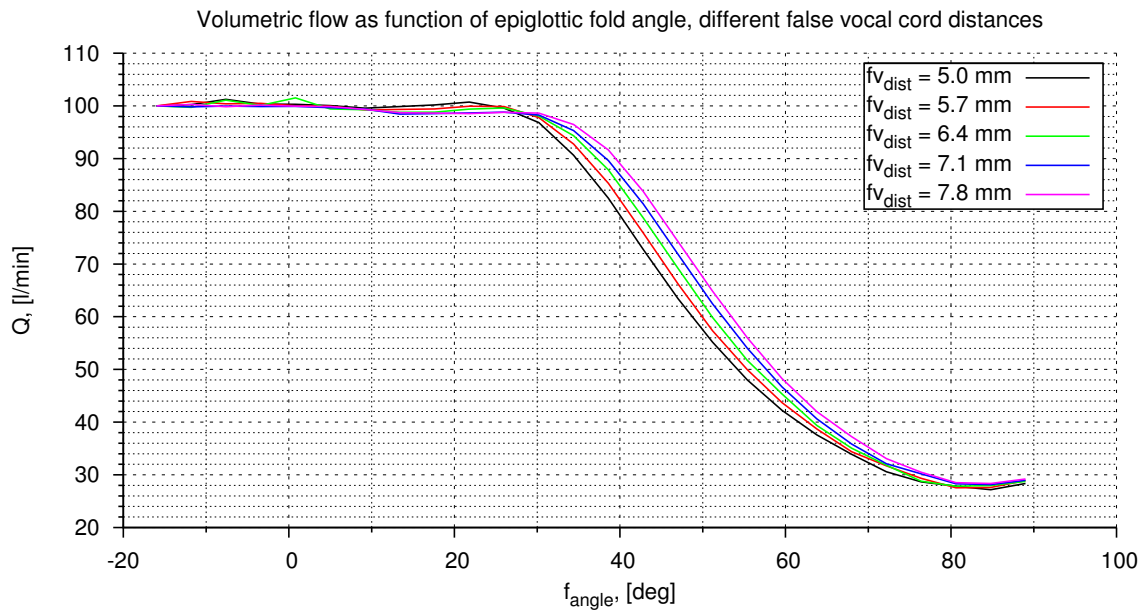


Figure 4.38: The epiglottic fold angle case study with different false vocal cord heights, the resulting flow, Model 1.

## 4.5 Model 1 with elasticity results

### 4.5.1 Simulation methodology

The aim for the coupled CFD and elasticity simulation is to find a stationary epiglottic fold shape, for which the elasticity forces and the stationary fluid forces (the pressure) are balanced.

1. In an ideal case, the pressure and the elasticity forces are perfectly balanced at the final state. However, in the reality one must use a stopping criterion — such as an maximal allowed change of the shape between iterations.
2. The *RMS* change of the centroid coordinates  $\delta_{RMS}$  is selected for the epiglottic fold shape change measure.
3. Often one can not use the new shape solution directly, because the change can be too large to converge to a stationary solution. In current work a damping factor  $\alpha$  is introduced. Damping factor  $\alpha$  determines, how large step in a direction of new solution one takes.

Such method can be identified as a generalized fixed point iteration method [1].

The simulations are carried out with and without any stopping criterion. Simulations without the stopping criterion are done in order to observe iteration dynamics. For other simulations,

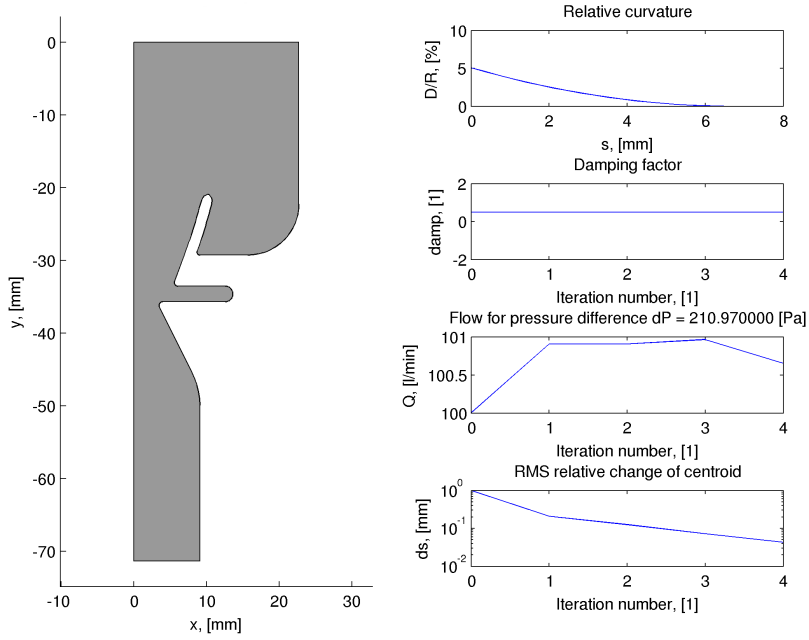


Figure 4.39: The geometry and the iteration statistics, the converged simulation,  $E = 50$  kPa, damping coefficient  $\alpha = 0.5$ , iteration 4, the Model 1 with elasticity.

the following stopping criterion is used:

$$\delta_{RMS} \leq 0.05 \text{ mm.} \quad (4.5)$$

The value is selected to be much smaller than the typical width of the epiglottic fold (1.5 mm). A smaller value is not reasonable, since the convergence is very oscillatory for  $\delta_{RMS}$  values smaller than the selected stopping criterion.

The reference simulation resulted in higher reference pressure drop  $\Delta P_{\text{ref}}^{\text{M1E}} = 210.97 \text{ Pa}$  compared to the Model 1 simulation  $\Delta P_{\text{ref}}^{\text{M1}}$ .

### 4.5.2 Stiff epiglottic fold study

Various Young modulus  $E$  values are considered for the epiglottic fold elasticity. For large  $E$  values, the epiglottic fold shape changes only slightly. A converged shape with  $E = 50$  kPa is obtained already after 4 iterations. The result is given in Fig. 4.39. The final shape is very close to the initial shape. An obvious conclusion is that for very large Young modulus there are no problems with the epiglottic fold bending and blocking the air passage.

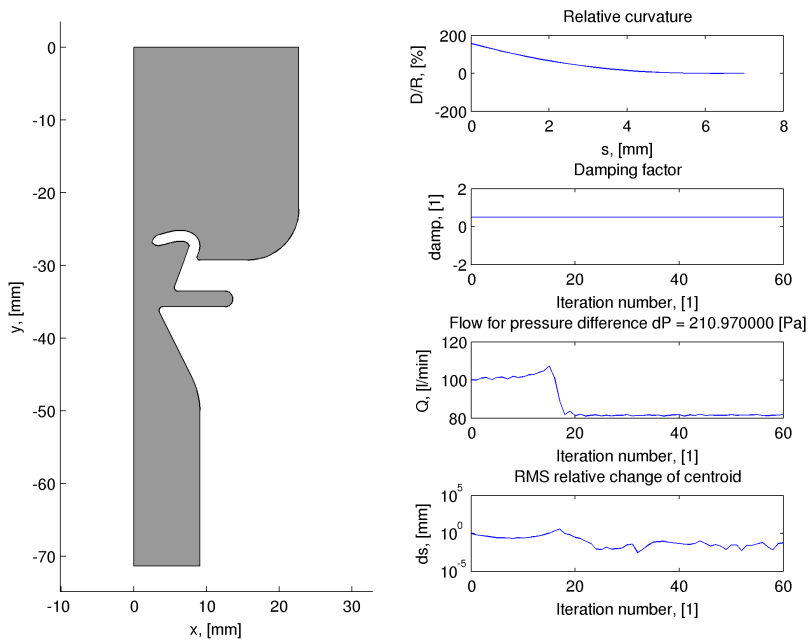


Figure 4.40: The geometry and the iteration statistics, no convergence,  $E = 16 \text{ kPa}$ , damping coefficient  $\alpha = 0.5$ , iteration 60, the Model 1 with elasticity.

### 4.5.3 Soft epiglottic fold study

For the Young modulus value of  $E = 16 \text{ kPa}$ , more interesting results are obtained. A simulation using the damping coefficient  $\alpha = 0.5$  without stopping criterion is carried out. The geometry and iteration statistics are given in Fig. 4.40. The simulation seems to indicate that there could be two equilibrium points, one stable and one unstable. An unstable equilibrium point is suggested by the first local minimum (around iteration number 10), whereas a stable equilibrium point is suggested by the oscillations around same shape (after iteration number 25).

The next simulation is carried out using the damping coefficient  $\alpha = 0.1$ . The stopping criterion is satisfied after 98 iterations. The simulation does not converge at the proposed unstable equilibrium point. The final geometry and iteration statistics are given in Fig. 4.41. The stationary shape can be roughly related to the laryngoscopic view of the supra-glottic EILO (in right part of Fig. 1.3). The picture with the supra-glottic EILO with cross section identified is given in Fig. 4.42. The similarities between the obtained shape (Fig. 4.41) and the laryngoscopic view of the supra-glottic EILO (Fig. 4.42) suggest that even a crude elasticity modelling might be of some use for investigations, how different epiglottic fold shapes behave in fluid flow. Nevertheless, the real life situation is rather complicated and the 2D approximation of the geometry is very rough.

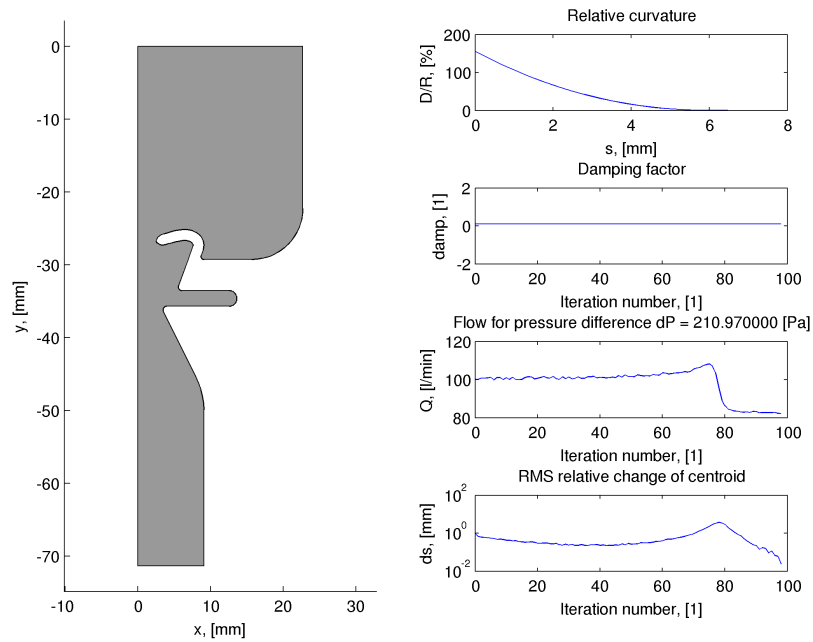


Figure 4.41: The geometry plot and the iteration statistics, converged simulation,  $E = 16$  kPa, damping  $\alpha = 0.1$ , iteration 98, Model 1 with elasticity.

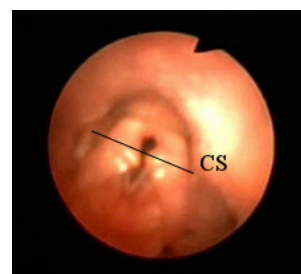


Figure 4.42: The laryngoscopic view of the supra-glotic obstruction condition closed state, the cross section identified (black line  $CS$ ).



## 5 Investigation for future 3D simulations

In the current work no 3D simulations are carried out, however a short analysis for a future work is presented. In order to pursue 3D simulations, one must come up with a reasonable geometry approximation. There exists few possible approaches to such task:

1. **A conceptional model.** One can use few main parameters and construct the 3D geometry in a similar way as the 2D models are constructed (see Section 3).
2. **A geometry constructed from measurements.** One can use various scanning techniques (for example, Magnetic Resonance Imaging) to obtain a set of cross-section scans and reconstruct the geometry from them.
3. **A hybrid model.** One can use the real measurement reconstructed geometry for the main parts (the airway walls, for example) and construct specific parts (the epiglottic fold, for example) using conceptual modelling.

Creating a good 3D geometry is very complicated and much harder than in 2D. The reconstruction from scans usually require rather complicated algorithms. The mixed design incorporate the upsides and the complexities of both cases.

### 5.1 Conceptual model

An initial attempt to design a reasonable 3D model is shown in Fig. 5.1. The generation of this geometry is quite complicated due to the specifics of vocal chord shape and opening and closing processes. Moreover, for useful geometry approximation many important details (such as epiglottic fold, false vocal chords) are still to be designed and added. The advantage with this approach is that it provides a large freedom to control the obtained geometry. The model can be designed in a way that allows an easy modification of the main parameters. However, the design of the specific parts will require substantial thinking and tweaking.

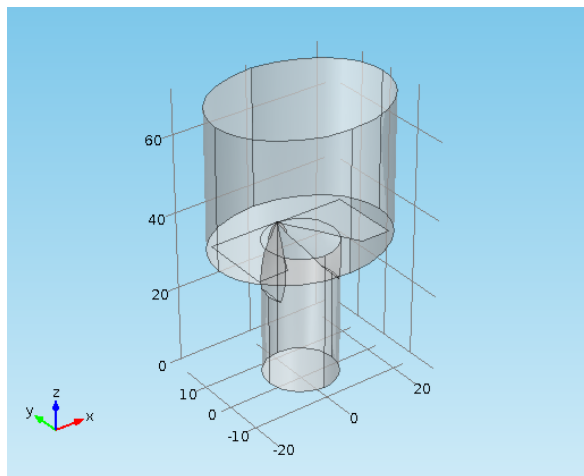


Figure 5.1: The initial attempt to design a 3D larynx model, the base geometry with the vocal chords.

## 5.2 Constructed geometries from MRI scans

An alternative to manually designing the geometry approximation is to construct it from measurements. During the investigation of this approach, a contact with researchers in Helsinki University of Technology, Finland [6] was taken. Their work concerns the geometry of the human upper airway during phonation of various vowels.

The aim for their work is to design a work flow for a computer assisted treatment of the phonation problems. They have done quite a few MRI scans of the upper human airways during the phonation of specific sounds. An example cross section scan is given in the left part of Fig. 5.2. With many such cross section scans, it is possible to reconstruct the 3D geometry (right part of Fig. 5.2) using picture analysis tools. The reconstruction procedures are developed and various geometries has been created at the Helsinki University of Technology [6].

The main interest of the current work lies in the region close to the vocal cords. The generated geometry in more details is investigated there (see Fig. 5.3). For a better comparison with the laryngoscopic view (Fig. 1.3), one can generate a similar view of the given mesh (see Fig. 5.4). Unfortunately, the main parts of interest (the epiglottic fold, the vocal cords) can not be clearly identified. The reason is resolution (The resolution is about 2 mm for the investigated scans, while the epiglottic fold is approximately 1.5 mm wide.) and the vibration of the vocal chords, that essentially smears them out.

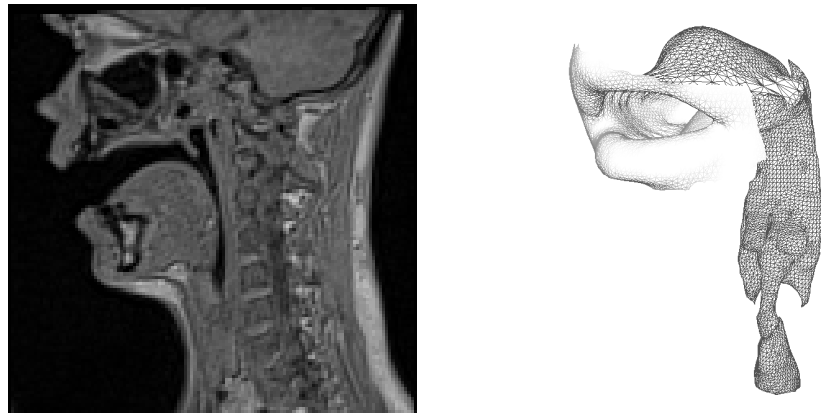


Figure 5.2: An example of the human MRI cross section scan in the upper airway region (left) and the reconstructed geometry (right) [6].

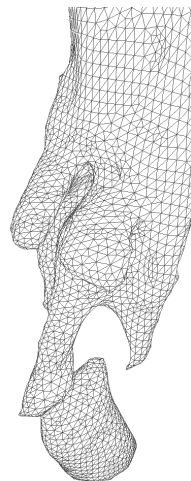


Figure 5.3: An example of the reconstructed geometry of the human upper airways from the MRI scans [6], the region of interest zoomed.

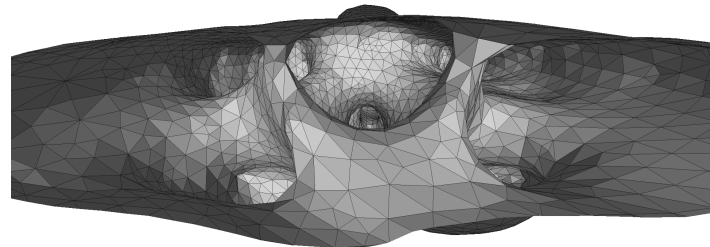


Figure 5.4: A laryngoscopic view of a reconstructed geometry of the human upper airways based on MRI scans [6].



## 6 Conclusions

In the current work, computational fluid dynamics was used to investigate flow properties for various epiglottic fold shapes of relevance to supra-glottic and glottic exercise induced laryngeal obstructions (EILO). Two larynx geometry approximations were used in the numerical simulations. Relations between the resulting flow (breathing rate) for constant lung suction pressure and various epiglottic fold configurations were found. Shapes of elastic epiglottic fold were found that balance the fluid forces and the elastic forces.

A significant reduction (up to 50%) of resulting breathing rate was observed in most cases with the epiglottic fold in a closed position (see the largest length region in Fig. 4.16 and the largest angle region in Fig. 4.20, as well as in Fig. 4.32). Surprisingly, at some intermediate locations of the epiglottic fold, a notable increase up to 15% of resulting breathing rate was observed (see the flow rate peak in Fig. 4.16, Fig. 4.20 and Fig. 4.32). These results suggest a hypothesis that a partial larynx blockage may thus be beneficial, but risky. If the partial larynx blockage transitions to full blockage, reduction in the resulting flow is drastic. Further studies to support the hypothesis would be needed.

The larger volumetric flow results for larger epiglottic fold distances from the vocal chords (see Fig. 4.12 and Fig. 4.38) seem to support the conjecture, expressed by our collaborators in Uppsala, that the EILO condition is more severe if the the epiglottic fold is closer to the vocal chords. (The EILO condition is more common amongst girls, who on average have a smaller distance between the epiglottic fold and vocal cords than boys.) There was no notable change in horizontal force on vocal cords (see Fig. 4.14, Fig. 4.18, and Fig. 4.22). No indications that the supra-glottic EILO could trigger the glottic EILO because of the fluid forces were obtained.

There is similarity between stationary epiglottic fold shape solution and laryngoscopic view of the supra-glottic EILO (see Fig. 4.41 and Fig. 4.42). The result indicates that even a simple elasticity description may be useful for investigating how different epiglottic fold shapes behave in fluid flow.



## A Derivation of a beam stretching equation

In order to better understand the derivation of the bending elasticity that is given in the current work, a simpler case of continuous stretching of a beam with a length  $L$  is considered. To keep things intuitive, the beam is fixed at the coordinate origin and a force is applied at the other end. Also, there might be a surface tension all over the beam surface. The main non-deformed coordinate is  $x$ , while the deformed coordinate is  $x'$ . A sketch of the described problem is given in Fig. A.1.

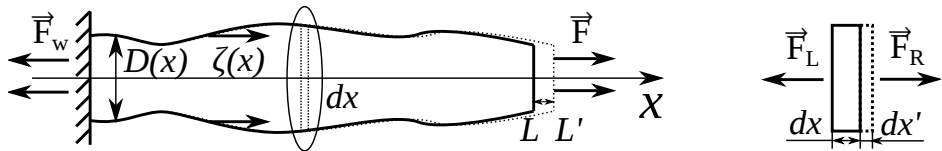


Figure A.1: The sketch of the simple beam stretching, the left side fixed, the force applied on the right side and the tension applied on boundaries (left), a infinitesimal beam element with the respective extension (right).

In the left part of Fig. A.1 the notation are as follows,  $\vec{F}_w$  is the force the wall exerts on the beam,  $\vec{F}$  is the force that is applied at the other end of the beam,  $D(x)$  is the width of the beam, and  $\zeta(x)$  is the horizontal tension on the beam boundary (positive if in  $\hat{x}$  direction).

In the right part of Fig. A.1 an infinitesimal small element of a non-deformed beam with a length  $dx$  is considered, such that forces from the left  $\vec{F}_L$  and the right  $\vec{F}_R = -\vec{F}_L$  are opposite and equal in the magnitude and the width  $D(x)$  is constant. The infinitesimal small element of the beam is deformed and the length is increased by an infinitesimal small change  $dx'$ . The relation can be specified using the material Young modulus  $E$  and the Hooks law as

$$F_L(x) = F_R(x) = F(x) = E \cdot S(x) \cdot \frac{dx'}{dx} = E \cdot D(x) \cdot L_z \cdot \frac{dx'}{dx}, \quad (\text{A.1})$$

where  $L_z$  is beam size in the  $\hat{z}$  direction.

One can think a bit about how the force forms on each of the mentioned slices and how the Newtons first law is fulfilled. As first, one can explicitly write the force that wall exerts on the beam (opposite to the force that the beam exerts on the wall, a sum of force at the end boundary and tension on the side boundaries) as

$$F_w = - \left( F + L_z \int_0^L \zeta(x) dx \right). \quad (\text{A.2})$$

At position  $x$  in the beam, the force from the right can be found as a respective integral from the position in question to the end of beam, with addition of force at the end of the beam:

$$F_R(x) = L_z \int_x^L \zeta(\tilde{x}) d\tilde{x} + F, \quad (\text{A.3})$$

whereas the force from the left can be found as a respective integral from the beginning of the beam to the position in question, with addition of the force at the wall as

$$\begin{aligned} F_L(x) &= F_w + L_z \int_0^x \zeta(\tilde{x}) d\tilde{x} = -F - L_z \int_0^L \zeta(x) dx + L_z \int_0^x \zeta(\tilde{x}) d\tilde{x} = \\ &= -F - L_z \int_x^L \zeta(\tilde{x}) d\tilde{x} = -F_R(x). \end{aligned} \quad (\text{A.4})$$

In stationary case, it is easy to prove the Newtons first law for the every beam point, it reads  $F_R(x) = -F_L(x) = F(x)$ . Using the obtained force results, one can write a differential equation for the displacement  $x'$  using the equation (A.1) and (A.4), the result is

$$E \cdot D(x) \cdot L_z \cdot \frac{dx'}{dx} = F(x) = L_z \int_x^L \zeta(\tilde{x}) d\tilde{x} + F. \quad (\text{A.5})$$

In order to get the final result (get rid from the integral in the explicit expression), one can differentiate both sides and use integral with a variable limit theorem and obtain

$$\frac{d}{dx} \left( E \cdot D(x) \cdot \frac{dx'}{dx} \right) = \zeta(x). \quad (\text{A.6})$$

In order to give a little remainder of the rigorous mathematical treatment in this case, one can illustrate the last step as follows. First, the equation is written explicitly in two infinitely close points as

$$\begin{aligned} E \cdot D(x + dx) \cdot \frac{dx'}{dx} \Big|_{x+dx} &= \int_{x+dx}^L \zeta(\tilde{x}) d\tilde{x} + F/L_z, \\ E \cdot D(x) \cdot \frac{dx'}{dx} \Big|_x &= \int_x^L \zeta(\tilde{x}) d\tilde{x} + F/L_z = \int_x^{x+dx} \zeta(\tilde{x}) d\tilde{x} + \int_{x+dx}^L \zeta(\tilde{x}) d\tilde{x} + F/L_z. \end{aligned} \quad (\text{A.7})$$

The second expression can be subtracted from the first. The assumption that both points are very close, gives horizontal stress  $\zeta(x) \approx \zeta(x + dx) = \text{const}$ , that can be derived to be

$$E \cdot \left( D(x + dx) \cdot \frac{dx'}{dx} \Big|_{x+dx} - D(x) \cdot \frac{dx'}{dx} \Big|_x \right) = \int_x^{x+dx} \zeta(\tilde{x}) d\tilde{x} \approx \zeta(x + dx/2) dx. \quad (\text{A.8})$$

Dividing both sides of the equation (A.8) with the  $dx$  and taking the limit  $dx \rightarrow 0$  gives definition of a derivative on the left hand side, whereas the right hand side remains as the  $\zeta(x)$ . Hence we have arrived with the equation (A.6).

While the force derivative  $dF/dx$  essentially gives the linear force density and the division by the 2D domain  $\hat{z}$  length  $L_z$  yields the stress, going through such derivations are useful for keeping a good understanding of the used equations.

## B Full analytical description of smooth flow guide

Schematics of an example case (2D, given inflow  $Q_0$ , half channel widths  $h_0$  and  $h_1$  and transition length  $L$ ) are given in Fig. B.1.

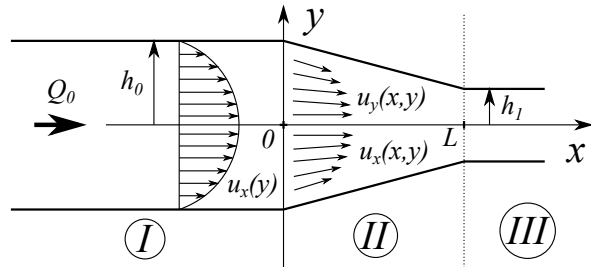


Figure B.1: The schematic representation of the case to be investigated, 2D.

The stationary incompressible fluid description (The Navier–Stokes and the continuity equations) in the vector form is given below:

$$\begin{aligned} \rho (\vec{u} \cdot \nabla) \vec{u} &= -\nabla P + \mu \nabla^2 \vec{u}, \\ \nabla \cdot \vec{u} &= 0. \end{aligned} \quad (\text{B.1})$$

Same equations in the full component form:

$$\begin{aligned} \rho \left( u_x \frac{\partial u_x}{\partial x} + u_y \frac{\partial u_x}{\partial y} \right) &= -\frac{\partial P}{\partial x} + \mu \left( \frac{\partial^2 u_x}{\partial x^2} + \frac{\partial^2 u_x}{\partial y^2} \right), \\ \rho \left( u_x \frac{\partial u_y}{\partial x} + u_y \frac{\partial u_y}{\partial y} \right) &= -\frac{\partial P}{\partial y} + \mu \left( \frac{\partial^2 u_y}{\partial x^2} + \frac{\partial^2 u_y}{\partial y^2} \right), \\ \frac{\partial u_x}{\partial x} + \frac{\partial u_y}{\partial y} &= 0. \end{aligned} \quad (\text{B.2})$$

In the region  $I$  it is assumed that the flow obeys the Poiseuilles law. The assumption is that  $\vec{u} \rightarrow u_x(y)$  (the continuity equation is satisfied automatically), consequently from the  $\hat{y}$  component of the Navier-Stokes equations there is no pressure change in the  $\hat{y}$  direction, that means  $P = P(x)$ . Using the  $\hat{x}$  component one can derive:

$$\begin{aligned} 0 &= -\frac{\partial P}{\partial x} + \mu \frac{\partial^2 u_x}{\partial y^2}, \\ \frac{\partial^2 u_x}{\partial y^2} &= \frac{1}{\mu} \frac{\partial P}{\partial x} = 2A. \end{aligned} \quad (\text{B.3})$$

Since the left and the right part is dependent from different independent coordinates (the velocity from the  $y$  coordinate and the pressure from the  $x$  coordinate), one must set both expressions to constants:

$$\begin{aligned} P(x) &= 2\mu Ax + P_{ref}, \\ u_x(y) &= Ay^2 + By + C. \end{aligned} \quad (\text{B.4})$$

To obtain the final relations (the expressions for  $A$ ,  $B$  and  $C$ ), one must apply boundary conditions (the no slip condition at the walls) and the initial condition (the given inflow). The quadratic function is rewritten in form, that would be zero at  $y = \pm h_0$  and it is continued with the flow integration:

$$\begin{aligned} u_x(y) &= Ay^2 + By + C = Ah_0^2 \left( \frac{y^2}{h_0^2} - 1 \right), \\ Q_0 &= \int_{-h_0}^{h_0} u_x dy = \int_{-h_0}^{h_0} (Ay^2 - Ah_0^2) dy = -2Ah_0^3 + A \left[ \frac{y^3}{3} \right]_{-h_0}^{h_0} = -\frac{4}{3}Ah_0^3, \\ A &= -\frac{3}{4} \frac{Q_0}{h_0^3}. \end{aligned} \quad (\text{B.5})$$

The final relations for the Poiseuilles flow is:

$$\begin{aligned} P(x) &= -\mu \frac{3}{2} \frac{Q_0}{h_0^3} x + P_{ref}, \\ u_x(y) &= \frac{3}{4} \frac{Q_0}{h_0} \left( 1 - \frac{y^2}{h_0^2} \right). \end{aligned} \quad (\text{B.6})$$

To proceed with the derivation in the region  $II$ , one can make assumption that the Poiseuilles law holds true for the velocity  $\hat{x}$  component with a coordinate dependent width  $h = h(x)$ . For a linear transition (see Fig.B.1) the width can be expressed as:

$$h = h_0 - d \cdot x; \quad d = \frac{h_0 - h_1}{L}. \quad (\text{B.7})$$

Under such assumption, the velocity  $\hat{y}$  component is uniquely defined from the continuity equation. Later on both velocity expressions can be used to obtain the pressure gradient and the pressure from the Navier-Stokes equation.

The derivation is initiated with determining the  $u_y(x, y)$  component (from now on the  $h$  is assumed to be the coordinate dependent  $h = h(x)$  with a derivative  $h' = -d$ , see the

equation B.7), derivation is:

$$\begin{aligned}
 u_x(x, y) &= \frac{3}{4} \frac{Q_0}{h} \left( 1 - \frac{y^2}{h^2} \right), \\
 \frac{\partial u_x}{\partial x} &= \frac{3}{4} \frac{Q_0 d}{h^2} - \frac{9}{4} \frac{Q_0 d}{h^4} y^2 = \frac{3}{4} \frac{Q_0 d}{h^2} \left( 1 - 3 \frac{y^2}{h^2} \right) = [\text{eq. B.2}] = -\frac{\partial u_y}{\partial y}, \\
 u_y(x, y) &= \frac{3}{4} \frac{Q_0 d}{h^2} \int_{-h}^y \left( 3 \frac{y'^2}{h^2} - 1 \right) dy' = \frac{3}{4} \frac{Q_0 d}{h^2} \left[ \frac{y'^3}{h^2} - y' \right]_{-h}^y = \frac{3}{4} \frac{Q_0 d}{h^2} y \left( \frac{y^2}{h^2} - 1 \right).
 \end{aligned} \tag{B.8}$$

From now on the velocity functions (B.9) and (B.10) is taken as assumed relations:

$$u_x(x, y) = \frac{3}{4} \frac{Q_0}{h} \left( 1 - \frac{y^2}{h^2} \right), \tag{B.9}$$

$$u_y(x, y) = \frac{3}{4} \frac{Q_0 d}{h^2} y \left( \frac{y^2}{h^2} - 1 \right). \tag{B.10}$$

Since  $d$  is a constant parameter, the velocity component  $u_y(0, y)$  at the coordinate start point or the interface between the flow channel and the transition region can not be zero. Therefore it is not possible to match the given regions. This behaviour arise from the fact that the boundary is discontinuous.

In order to continue the derivation, one must obtain the velocity derivatives for the inertial part of the Navier-Stokes equation:

$$\begin{aligned}
 \frac{\partial u_x}{\partial x} &= -\frac{\partial u_y}{\partial y} = \frac{3}{4} \frac{Q_0 d}{h^2} \left( 1 - 3 \frac{y^2}{h^2} \right), \\
 \frac{\partial u_x}{\partial y} &= -\frac{3}{2} \frac{Q_0}{h^3} y; \quad \frac{\partial u_y}{\partial x} = 3 \frac{Q_0 d^2}{h^5} y^3 - \frac{3}{2} \frac{Q_0 d^2}{h^3} y = \frac{3}{2} \frac{Q_0 d^2}{h^3} y \left( 2 \frac{y^2}{h^2} - 1 \right).
 \end{aligned} \tag{B.11}$$

The Navier-Stokes  $\hat{x}$  component inertial term derivation:

$$\begin{aligned}
 u_x \frac{\partial u_x}{\partial x} &= \frac{3}{4} \frac{Q_0}{h} \left( 1 - \frac{y^2}{h^2} \right) \cdot \frac{3}{4} \frac{Q_0 d}{h^2} \left( 1 - 3 \frac{y^2}{h^2} \right) = \frac{9}{16} \frac{Q_0^2 d}{h^3} \left( 1 - \frac{y^2}{h^2} \right)^2 - \frac{9}{8} \frac{Q_0^2 d}{h^5} \left( 1 - \frac{y^2}{h^2} \right) y^2, \\
 u_y \frac{\partial u_x}{\partial y} &= \frac{3}{4} \frac{Q_0 d}{h^2} y \left( \frac{y^2}{h^2} - 1 \right) \cdot \left( -\frac{3}{2} \frac{Q_0}{h^3} y \right) = \frac{9}{8} \frac{Q_0^2 d}{h^5} \left( 1 - \frac{y^2}{h^2} \right) y^2, \\
 u_x \frac{\partial u_x}{\partial x} + u_y \frac{\partial u_x}{\partial y} &= \frac{9}{16} \frac{Q_0^2 d}{h^3} \left( 1 - \frac{y^2}{h^2} \right)^2.
 \end{aligned} \tag{B.12}$$

The Navier-Stokes viscous term  $\hat{x}$  component derivation:

$$\begin{aligned}\frac{\partial^2 u_x}{\partial x^2} &= \frac{\partial}{\partial x} \left( \frac{\partial u_x}{\partial x} \right) = \frac{3}{2} \frac{Q_0 d^2}{h^3} - 9 \frac{Q_0 d^2}{h^5} y^2 = \frac{3}{2} \frac{Q_0 d^2}{h^3} \left( 1 - 6 \frac{y^2}{h^2} \right), \\ \frac{\partial^2 u_x}{\partial y^2} &= \frac{\partial}{\partial y} \left( \frac{\partial u_x}{\partial y} \right) = -\frac{3}{2} \frac{Q_0}{h^3}, \\ \frac{\partial^2 u_x}{\partial x^2} + \frac{\partial^2 u_x}{\partial y^2} &= \frac{3}{2} \frac{Q_0 d^2}{h^3} \left( 1 - 6 \frac{y^2}{h^2} \right) - \frac{3}{2} \frac{Q_0}{h^3} = \frac{3}{2} \frac{Q_0}{h^3} (d^2 - 1) - 9 \frac{Q_0 d^2}{h^5} y^2.\end{aligned}\quad (\text{B.13})$$

Using the obtained results, one can write the pressure gradient in the  $\hat{x}$  direction as:

$$\begin{aligned}\frac{\partial P}{\partial x} &= -\rho \left( u_x \frac{\partial u_x}{\partial x} + u_y \frac{\partial u_x}{\partial y} \right) + \mu \left( \frac{\partial^2 u_x}{\partial x^2} + \frac{\partial^2 u_x}{\partial y^2} \right), \\ \frac{\partial P}{\partial x} &= -\rho \frac{9}{16} \frac{Q_0^2 d}{h^3} \left( 1 - \frac{y^2}{h^2} \right)^2 + \mu \left[ \frac{3}{2} \frac{Q_0}{h^3} (d^2 - 1) - 9 \frac{Q_0 d^2}{h^5} y^2 \right].\end{aligned}\quad (\text{B.14})$$

However, to stitch the Poiseuilles flow in the regions *I* and *III* with the undetermined flow in the region *II* (see Fig. B.1), one must demand relations  $h(0) = h_0$ ,  $h'(0) = h''(0) = h^{(3)}(0) = 0$ ,  $h(L) = h_1$  and  $h'(L) = h''(L) = h^{(3)}(L) = 0$  to hold, that would lead to:

$$u_y \Big|_{x=0;L} = \frac{\partial u_y}{\partial y} \Big|_{x=0;L} = \frac{\partial^2 u_y}{\partial y^2} \Big|_{x=0;L} = \frac{\partial u_y}{\partial x} \Big|_{x=0;L} = \frac{\partial^2 u_y}{\partial x^2} \Big|_{x=0;L} = 0 \rightarrow \frac{\partial P}{\partial y} \Big|_{x=0;L} = 0. \quad (\text{B.15})$$

That would mean taking the function  $h$  as a polynomial of order 7, that is  $h = a_1 x^7 + a_2 x^6 + a_3 x^5 + a_4 x^4 + a_5 x^3 + a_6 x^2 + a_7 x + a_8$ . Note, to satisfy the velocity continuum, a polynomial of an order 3 is sufficient. Applying the conditions described above, one can get the coefficients  $a_i$ . Under such assumption, the section *II* boundary in comparison to previous case (see Fig. B.1) would now look as shown in Fig. B.2. The precise shapes of usable transition sections on a unit interval with the entrance and exit widths  $h_0 = 2$  and  $h_1 = 1$  are given in Fig. B.3.

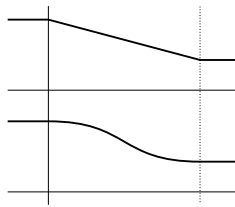


Figure B.2: A schematic representation of the region *II* boundary, the comparison between the linear case and the polynomial case.

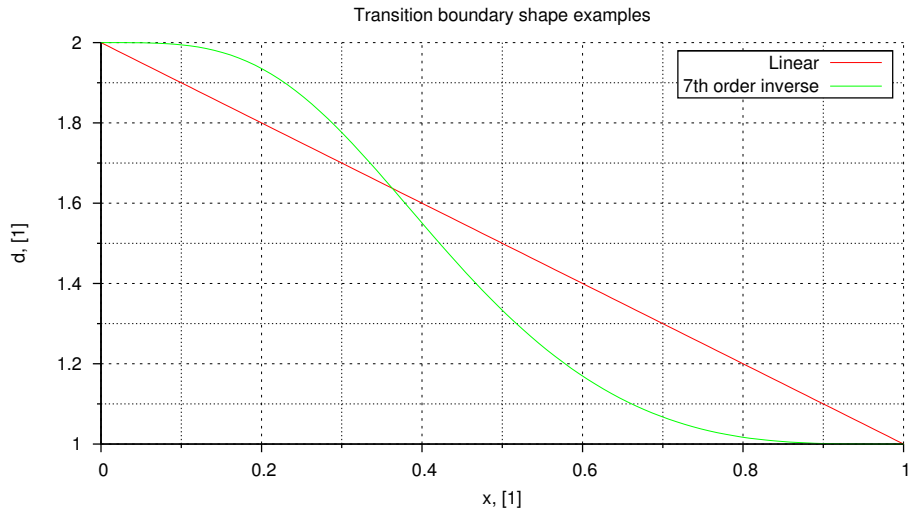


Figure B.3: The precise representation of the transition regions with the linear boundary and the 7th order inverse polynomial boundary.

In such case, the velocity relations

$$u_x(x, y) = \frac{3}{4} \frac{Q_0}{h} \left( 1 - \frac{y^2}{h^2} \right), \quad (\text{B.16})$$

$$u_y(x, y) = -\frac{3}{4} \frac{Q_0 h'}{h^2} y \left( \frac{y^2}{h^2} - 1 \right) \quad (\text{B.17})$$

are still valid. Various derivatives are

$$\begin{aligned} \frac{\partial u_x}{\partial y} &= -\frac{3}{2} \frac{Q_0}{h^3} y; \quad \frac{\partial^2 u_x}{\partial y^2} = -\frac{3}{2} \frac{Q_0}{h^3}; \quad \frac{\partial u_x}{\partial x} = -\frac{3}{4} \frac{Q_0 h'}{h^2} \left( 1 - 3 \frac{y^2}{h^2} \right), \\ \frac{\partial^2 u_x}{\partial x^2} &= -\frac{3}{4} \frac{Q_0 h''}{h^2} + \frac{3}{2} \frac{Q_0 h'^2}{h^3} + \frac{9}{4} \frac{Q_0 h''}{h^4} y^2 - 9 \frac{Q_0 h'^2}{h^5} y^2 = \\ &= -\frac{3}{4} \frac{Q_0 h''}{h^2} \left( 1 - 3 \frac{y^2}{h^2} \right) + \frac{3}{2} \frac{Q_0 h'^2}{h^3} \left( 1 - 6 \frac{y^2}{h^2} \right). \end{aligned} \quad (\text{B.18})$$

The Navier-Stokes inertial term  $\hat{x}$  component derivation is

$$\begin{aligned} u_x \frac{\partial u_x}{\partial x} &= -\frac{3}{4} \frac{Q_0}{h} \left( 1 - \frac{y^2}{h^2} \right) \cdot \frac{3}{4} \frac{Q_0 h'}{h^2} \left( 1 - 3 \frac{y^2}{h^2} \right) = -\frac{9}{16} \frac{Q_0^2 h'}{h^3} \left( 1 - \frac{y^2}{h^2} \right)^2 + \frac{9}{8} \frac{Q_0^2 h'}{h^5} \left( 1 - \frac{y^2}{h^2} \right) y^2, \\ u_y \frac{\partial u_x}{\partial y} &= -\frac{3}{4} \frac{Q_0 h'}{h^2} y \left( \frac{y^2}{h^2} - 1 \right) \cdot \left( -\frac{3}{2} \frac{Q_0}{h^3} y \right) = -\frac{9}{8} \frac{Q_0^2 h'}{h^5} \left( 1 - \frac{y^2}{h^2} \right) y^2, \\ u_x \frac{\partial u_x}{\partial x} + u_y \frac{\partial u_x}{\partial y} &= -\frac{9}{16} \frac{Q_0^2 h'}{h^3} \left( 1 - \frac{y^2}{h^2} \right)^2. \end{aligned} \quad (\text{B.19})$$

The Navier-Stokes viscous term  $\hat{x}$  component is

$$\begin{aligned} \frac{\partial^2 u_x}{\partial x^2} + \frac{\partial^2 u_x}{\partial y^2} &= -\frac{3}{4} \frac{Q_0 h''}{h^2} \left(1 - 3 \frac{y^2}{h^2}\right) + \frac{3}{2} \frac{Q_0 h'^2}{h^3} \left(1 - 6 \frac{y^2}{h^2}\right) - \frac{3}{2} \frac{Q_0}{h^3} = \\ &= \frac{3}{4} \frac{Q_0}{h^3} (2h'^2 - h \cdot h'' - 2) + \frac{9}{4} \frac{Q_0 y^2}{h^5} (h \cdot h'' - 4h'). \end{aligned} \quad (\text{B.20})$$

That all leads to the pressure gradient  $\hat{x}$  component expression

$$\begin{aligned} \frac{\partial P}{\partial x} &= -\rho \left( u_x \frac{\partial u_x}{\partial x} + u_y \frac{\partial u_x}{\partial y} \right) + \mu \left( \frac{\partial^2 u_x}{\partial x^2} + \frac{\partial^2 u_x}{\partial y^2} \right) = \\ &= \rho \frac{9}{16} \frac{Q_0^2 h'}{h^3} \left(1 - \frac{y^2}{h^2}\right)^2 + \mu \frac{3}{4} \frac{Q_0}{h^3} (2h'^2 - h \cdot h'' - 2) + \mu \frac{9}{4} \frac{Q_0 y^2}{h^5} (h \cdot h'' - 4h'). \end{aligned} \quad (\text{B.21})$$

At the center of the channel the expression simplifies to

$$\frac{\partial P}{\partial x} = \rho \frac{9}{16} \frac{Q_0^2 h'}{h^3} + \mu \frac{3}{4} \frac{Q_0}{h^3} (2h'^2 - h \cdot h'') - \mu \frac{3}{2} \frac{Q_0}{h^3}. \quad (\text{B.22})$$

One can note, that at  $x = 0$  and  $x = L$  the pressure gradient reduces to the derived expression for the Poiseuilles flow. The first term can be integrated easily, remembering, that  $dh = h' dx$ , it yields

$$\Delta P_1 = \int_0^L \frac{\partial P}{\partial x} \Big|_1 dx = \int_{h_0}^{h_1} \frac{\partial P}{\partial x} \Big|_1 \frac{dh}{h'} = \rho \frac{9}{32} Q_0^2 \left( \frac{1}{h_0^2} - \frac{1}{h_1^2} \right) = \rho \frac{9}{32} Q_0^2 \frac{(h_1 - h_0)(h_1 + h_0)}{h_0^2 h_1^2}. \quad (\text{B.23})$$

The second term integrated essentially is the velocity  $\hat{x}$  component derivative in respect to the  $\hat{x}$  coordinate. That results in

$$\Delta P_2 = \int_0^L \frac{\partial P}{\partial x} \Big|_2 dx = \mu \int_0^L \frac{\partial^2 u_x}{\partial x^2} dx = \mu \left[ \frac{\partial u_x}{\partial x} \right]_0^L = 0. \quad (\text{B.24})$$

And the last term must be integrated directly as

$$\Delta P_3 = \int_0^L \frac{\partial P}{\partial x} \Big|_3 dx = -\mu \frac{3}{2} Q_0 \int_0^L \frac{dx}{h^3}. \quad (\text{B.25})$$

The function  $h$  selection and the integral itself has been carried out in the appendix C, the result is

$$\Delta P_3 = -\mu \frac{3}{2} Q_0 \cdot C_8(h_0, h_1) \cdot L, \quad (\text{B.26})$$

where  $C_8$  is a constant depending only from the entrance and the exit heights  $h_0$  and  $h_1$ :

$$C_8(h_0, h_1) = \frac{613h_1^3 + 245h_0h_1^2 + 245h_0^2h_1 + 613h_0^3}{1716h_0^3h_1^3}. \quad (\text{B.27})$$

It can be concluded that for a static geometry the coefficients in front of the flow rate in the expressions (B.23) and (B.25) is of a similar order, that is  $1/h^2$  and  $L/h^3$  respectively. Therefore an explicit dominance of  $\Delta P_1$  or  $\Delta P_3$  is not found.

One possible thought might be that for the larger flow rates  $Q_0$ , the pressure drop over domain could be proportional to the quadratic flow rate  $Q_0^2$  (the  $\Delta P_1$  dominates), the investigated numerical results seem to support such conclusion (see Section 4.4.3).

A possible test would be finding the entrance and the exit heights  $h_0$  and  $h_1$  that would match the obtained coefficient from the Section 4.4.3 and compare the results with the actual dimensions of the simulation domain.

The coefficient in expression (B.23) to be matched is  $C = 9/32\rho(1/h_0^2 - 1/h_1^2)$ . In the numerical simulations, the pressure drop is taken with a positive sign, therefore the coefficient must be adjusted to  $C = 9/32\rho(1/h_1^2 - 1/h_0^2)$ . The coefficient logarithm  $\ln(C)$  can be read off the linear fitting (see Section 4.4.3), for the opened epiglottic fold case it is  $\ln(C) = 2.09678 + \ln([l/\text{min}]/[m^3/\text{s}]) = -8.90532$  (changed to match the SI system).

Both heights  $h_0$  and  $h_1$  are not uniquely defined at this point. Therefore the exit height  $h_1$  is set to match the half-diameter of the trachea (see the Section 3) as

$$h_1 = 9.07500 \text{ mm}. \quad (\text{B.28})$$

Under such assumption, the entrance height  $h_0$  is uniquely defined, and the final result is

$$h_1 = 9.07502 \text{ mm}. \quad (\text{B.29})$$

As one can see, the change in the theoretically proposed channel width is infinitesimal. The reason for such behaviour is the coefficient scale  $1/h^2$  (the derivative is very large around small  $h$  values, as in this case). Therefore the coefficient value is very sensitive on the change of channel height.

Hence one must conclude that the specific derivation and the coefficient values are not very reliable, despite that the quadratic relation between the flow rate and the pressure were obtained both in the theory and the numerical simulations.

## C Tied transition section boundary shape and integration

The boundary shape function  $h$  must satisfy conditions  $h(0) = h_0$ ,  $h'(0) = h''(0) = h^{(3)}(0) = 0$ ,  $h(L) = h_1$  and  $h'(L) = h''(L) = h^{(3)}(L) = 0$  in order to provide the boundary region matching or tied solutions. The choice of an ordinary 7th order polynomial is not good, because in such case integral

$$\Delta P_3 \propto \int_0^L \frac{dx}{h^3} \quad (\text{C.1})$$

is very hard to integrate analytically.

In order to simplify the task, one can investigate an inverse function derivatives in a comparison to the function derivatives:

$$\begin{aligned} \frac{\partial}{\partial x} \left( \frac{1}{f} \right) &= -\frac{f'}{f^2}, \\ \frac{\partial^2}{\partial x^2} \left( \frac{1}{f} \right) &= -\frac{f''}{f^2} + 2\frac{(f')^2}{f^3}, \\ \frac{\partial^3}{\partial x^3} \left( \frac{1}{f} \right) &= -\frac{f^{(3)}}{f^2} + 3\frac{f''f'}{f^4} + 4\frac{f'f''}{f^3} - 6\frac{(f')^3}{f^4}. \end{aligned} \quad (\text{C.2})$$

If the respective function  $f$  derivative at the point  $x_0$  is 0, also the inverted function  $1/f$  derivative at the point  $x_0$  is zero. Furthermore, if two consequent derivatives  $f'$  and  $f''$  of function  $f$  are 0 at the point  $x_0$ , the second derivative of function  $1/f$  at the point  $x_0$  is also zero. Same holds for the 3rd derivative. The conclusions stand, if the function  $f$  is strictly positive in the whole interval of interest. Luckily, such is this case.

Therefore one can set transition region width  $h = 1/\hat{h}$  and take  $\hat{h} = \sum_{i=0}^7 a_i x^i$ . The determination of the coefficients can be divided in two stages, first stage would treat the condition at  $x = 0$  and would give the following values in matrix form for the first four coefficients:

$$\begin{pmatrix} a_3 \\ a_2 \\ a_1 \\ a_0 \end{pmatrix} = \begin{pmatrix} 0 \\ 0 \\ 0 \\ 1/h_0 \end{pmatrix}. \quad (\text{C.3})$$

The second bunch of coefficients can be determined by the set of linear algebraic equations,

the system in matrix form is given below:

$$\begin{pmatrix} L^7 & L^6 & L^5 & L^4 \\ 7L^6 & 6L^5 & 5L^4 & 4L^3 \\ 42L^5 & 30L^4 & 20L^3 & 12L^2 \\ 210L^4 & 120L^3 & 60L^2 & 24L \end{pmatrix} \cdot \begin{pmatrix} a_7 \\ a_6 \\ a_5 \\ a_4 \end{pmatrix} = \begin{pmatrix} 1/h_1 - 1/h_0 \\ 0 \\ 0 \\ 0 \end{pmatrix}. \quad (\text{C.4})$$

Solving the system yields result:

$$\begin{pmatrix} a_7 \\ a_6 \\ a_5 \\ a_4 \end{pmatrix} = \frac{1/h_1 - 1/h_0}{L^4} \begin{pmatrix} -20/L^3 \\ 70/L^2 \\ -84/L \\ 35 \end{pmatrix}. \quad (\text{C.5})$$

For the integration, zero elements are skipped and the function is:

$$\hat{h} = a_7x^7 + a_6x^6 + a_5x^5 + a_4x^4 + a_0/ \quad (\text{C.6})$$

And one has to integrate a cubed version of it:

$$\begin{aligned} \hat{h}^3 &= (a_7x^7 + a_6x^6 + a_5x^5 + a_4x^4 + a_0)^3 = a_7^3x^{21} + 3a_6a_7^2x^{20} + \\ &+ (3a_5a_7^2 + 3a_6^2a_7)x^{19} + (3a_4a_7^2 + 6a_5a_6a_7 + a_6^3)x^{18} + \\ &+ (6a_4a_6a_7 + 3a_5^2a_7 + 3a_5a_6^2)x^{17} + (6a_4a_5a_7 + 3a_4a_6^2 + 3a_5^2a_6)x^{16} + \\ &+ (3a_4^2a_7 + 6a_4a_5a_6 + a_5^3)x^{15} + (3a_0a_7^2 + 3a_4^2a_6 + 3a_4a_5^2)x^{14} + \\ &+ (6a_0a_6a_7 + 3a_4^2a_5)x^{13} + (6a_0a_5a_7 + 3a_0a_6^2 + a_4^3)x^{12} + \\ &+ (6a_0a_4a_7 + 6a_0a_5a_6)x^{11} + (6a_0a_4a_6 + 3a_0a_5^2)x^{10} + 6a_0a_4a_5x^9 + 3a_0a_4^2x^8 + \\ &+ 3a_0^2a_7x^7 + 3a_0^2a_6x^6 + 3a_0^2a_5x^5 + 3a_0^2a_4x^4 + a_0^3 \end{aligned} \quad (\text{C.7})$$

In order not to make any mistake and not to write too long derivations, the integration is done using an analytical mathematics package *Maxima*. The integral is evaluated as follows:

$$\Delta P_3 \propto \int_0^L \frac{dx}{h^3} = \int_0^L \hat{h}^3 dx = \frac{613h_1^3 + 245h_0h_1^2 + 245h_0^2h_1 + 613h_0^3}{1716h_0^3h_1^3} \cdot L = C_8 \cdot L. \quad (\text{C.8})$$

At this point it is decided to cease efforts in this direction, because the obtained result relation with the problem to be solved is not clear. Further investigations should be carried out.

## References

- [1] R. L. Burden. *Numerical analysis*. Prindle, Weber & Schmidt, 1985.
- [2] H.E. Eckel, C. Sittel, P. Zorowka, and A. Jerke. Dimensions of the laryngeal framework in adults. *Surgical and Radiologic Anatomy*, 16:31–36, 1994.
- [3] V.J. Ervin and E.W. Jenkins. The LBB condition for the Taylor–Hood  $P_2 - P_1$  and Scott–Vogelius  $P_2 - \text{disc}P_1$  element pairs in 2-D. Technical Report, Clemson University, 2011.
- [4] H. Gray. *Anatomy of the Human Body*. 1918.
- [5] A.R. Lambert, P. O Shaughnessy, M.H. Tawhai, E.A. Hoffman, and C.L. Lin. Regional deposition of particles in an image-based airway model: large-eddy simulation and left-right lung ventilation asymmetry. *Aerosol Science and Technology*, 45(1):11–25, 2011.
- [6] J. Malinen. Personal communication. jmalinen@cc.hut.fi. Helsinki University of Technology.
- [7] A.A. Mancuso, H. Ojiri, and R.G. Quisling. *Head and Neck Radiology: A Teaching File*. Lippincott Williams & Wilkins, 2002.
- [8] C.M. Mermier, J.M. Samet, W.E. Lambert, and T.W. Chick. Evaluation of the relationship between heart rate and ventilation for epidemiologic studies. *Arch Environmental Health*, 48(4):263–269, 1993.
- [9] M. Mihaescu, S.M. Khosla, S. Murugappan, and E.J. Gutmark. Unsteady laryngeal airflow simulation of the intra-glottal vortical structures. *Journal of the Acoustical Society of America*, 127(1):435–444, 2010.
- [10] B. Mohammad and O. Pironneau. Unsteady separated turbulent flows computation with wall-laws and  $k - \varepsilon$  model. *Computer methods in applied mechanics and engineering*, 148:393–405, 1997.
- [11] G. Mylavaram, S. Murugappan, M. Mihaescu, M. Kalra, S. Khosla, and E. Gutmark. Validation of computational fluid dynamics methodology used for human upper airway flow simulations. *Journal of Biomechanics*, 42:1553–1559, 2009.
- [12] L. Nordang. Personal communication. Leif.Nordang@akademiska.se. Department of Otolaryngology, Uppsala University Hospital.

- [13] L. Nordang, S. Morén, H.M. Johansson, E. Wenngren, and L. Nordvall. Ansträngnings-astma kan vara laryngeal obstruktion. *Läkartidningen*, 106(38):2351–2353, 2009.
- [14] 3B Scientific. The Larynx Chart. <http://www.3bscientific.com/>.
- [15] Wikipedia. Darcy-Weisbach equation. [http://en.wikipedia.org/wiki/Darcy-Weisbach\\_equation](http://en.wikipedia.org/wiki/Darcy-Weisbach_equation).
- [16] D.C. Wilcox. *Turbulence modeling for CFD*. DCW Industries, Inc, 1994.
- [17] J. Xi, P.W. Longest, and T.B. Martonen. Effects of the laryngeal jet on nano- and microparticle transport and deposition in an approximate model of the upper tracheo-bronchial airways. *Journal of Applied Physiology*, 104:1761–1777, 2008.
- [18] M. Zuurbier, G. Hoek, P. Hazel, and B. Brunekreef. Minute ventilation of cyclists, car and bus passengers: an experimental study. *Environmental Health*, 8:48, 2009.